

**FACULTY  
OF MATHEMATICS  
AND PHYSICS**  
Charles University

**MASTER THESIS**

Tomáš Fodran

**Study of ultra-high energy cosmic ray  
propagation**

Institute of Particle and Nuclear Physics

Supervisor of the master thesis: doc. RNDr. Dalibor Nosek, Dr.

Study programme: Physics

Study branch: Nuclear and Subnuclear Physics

Prague 2019

I declare that I carried out this master thesis independently, and only with the cited sources, literature and other professional sources.

I understand that my work relates to the rights and obligations under the Act No. 121/2000 Sb., the Copyright Act, as amended, in particular the fact that the Charles University has the right to conclude a license agreement on the use of this work as a school work pursuant to Section 60 subsection 1 of the Copyright Act.

In ..... date .....

signature of the author

My biggest gratitude belongs to my family that supports me my whole life. Thank you to my brother Kuku that helped me numerous times and gave me helpful advice. Thank you to Lulu for her love and infinite patience with me during writing my thesis and my studies. Next, I would like to thank my supervisor Dr. Dalibor Nosek for his advice, valuable consultations, and comments regarding this master's thesis. One thanks also belongs to Dr. Vladimír Novotný for his consultations on Astroparticle topics and my thesis.

Title: Study of ultra-high energy cosmic ray propagation

Author: Tomáš Fodran

Institute: Institute of Particle and Nuclear Physics

Supervisor: doc. RNDr. Dalibor Nosek, Dr., Institute of Particle and Nuclear Physics

Abstract: The master's thesis is dedicated to studying the propagation of ultra-high energy proton cosmic rays under a hypothesis of Lorentz invariance violation. For this purpose, numerical methods were used. Our calculations indicated that the effective horizon of ultra-high energy cosmic protons is significantly extended when Lorentz invariance violation is assumed. Further, we investigated the effects of Lorentz invariance violation on the Cosmic ray spectrum. We learned that measured cosmic ray spectra are a suitable tool for constraining the coefficients describing Lorentz invariance violation and we estimated an interval where the upper bound on the pion Lorentz invariance violating coefficient lies. Moreover, a correlation between free parameters of the analytical model of cosmic ray spectrum and coefficients, that describes Lorentz invariance violation, was found.

Keywords: Lorentz invariance violation, Cosmic ray spectrum, Propagation of cosmic ray, Ultra-high energy cosmic ray.

# Contents

<b>Introduction</b>	<b>2</b>
<b>1 Cosmic rays</b>	<b>4</b>
1.1 Energy spectrum and composition of Cosmic rays . . . . .	5
1.2 Propagation of proton CR . . . . .	7
1.3 Energy evolution of proton CR . . . . .	13
<b>2 Effects of LIV on the propagation of proton CR</b>	<b>18</b>
2.1 LIV framework . . . . .	18
2.2 Modified kinematics . . . . .	20
2.3 Proton CR propagation modified by LIV . . . . .	23
<b>3 Proton CR spectrum modified by LIV effects</b>	<b>30</b>
3.1 Analytical calculation of the proton CR spectrum . . . . .	30
3.2 Proton CR spectra modified by LIV . . . . .	35
<b>Conclusion</b>	<b>41</b>
<b>Bibliography</b>	<b>42</b>
<b>List of Abbreviations</b>	<b>46</b>
<b>A Appendix</b>	<b>47</b>
<b>B Appendix</b>	<b>48</b>
<b>C Appendix</b>	<b>49</b>

# Introduction

Discovery of the Cosmic rays (CR) is imputed to Victor Hess. In 1912, he carried Wulf electrometers to an altitude of 5,300 meters in a free balloon flight. Contrary to his expectations the ionization rate was at this altitude twice the higher than at the sea level. He concluded that the radiation is coming from outer space. Later, in 1920, this statement was confirmed by Robert Millikan who performed a similar experiment by measuring the ionization rate from deep underwater to high altitudes. Also, he was the first one that named the extraterrestrial radiation as Cosmic rays. The mentioned experiments had put foundations for a new branch of particle physics - Astroparticle physics whose object of study are elementary particles of astronomical origin with their relation to astrophysics and cosmology.

From these pioneer times, until today, enormous progress has been made in the research of cosmic rays. Instead of observing only the simple power-law spectrum of CR, in the presence a complex structure of the spectrum with knee, second knee and steep cut-off at the highest energy is known, and instead of the all-particle energy spectrum, the individual mass groups are recognized. Moreover, the derived upper limits for the high energy neutrino and photon fluxes helped to exclude several top-down Ultra-high energy cosmic rays (UHECR) models such as topological defects, some dark matter models or the Z-bursts. However, the study of cosmic rays does not only restrict on answering astrophysical questions. It can also provide limited information on very high-energy phenomena or the existence of unknown elementary particles.<sup>1</sup> At Planck scale, i.e. at energies about  $10^{28}$  eV a new physics phenomena is expected to emerge. One of these theoretical concepts is Lorenz invariance violation (LIV) and since its effects are expected to increase with energy, CR can serve as excellent probes.

In this thesis, effects of the LIV on cosmic ray spectrum are investigated. Since the exact composition of CR is still unknown, a proton composition from energies  $10^{19}$  eV is assumed. Model of proton CR spectrum was calculated by using formalism developed by Berezhinsky and Grigorieva [1]. The main goal of this thesis was to find out whether the measured CR spectra can be used as a tool for constraining the LIV coefficients. Second goal was the investigation of the LIV effects. Particularly, how the LIV incorporation to physics will manifest in the model of cosmic ray spectrum, what will be its observable effects and whether the model with LIV is compatible with the observed data. We also investigated the relation between the LIV coefficients and free parameters of the spectrum model, particularly, parameter of the source evolution  $\zeta$ , parameter of the spectral index  $\Gamma$  and parameter of the maximal energy of the proton at source  $E_{max}^{source}$ . Moreover, the consequences of the LIV on the proton propagation were studied. An analytical approach for calculating the CR spectrum was chosen because currently no CR Monte Carlo program has incorporated LIV module.

In the first chapter a short review of cosmic rays is given. The energy losses are discussed herein details since they are essential for subsequent spectrum calculations. Next chapter describes the used LIV phenomenology and the effects of different orders of LIV coefficients on the inelasticity and the proton propagation

---

<sup>1</sup> Discovery of the positron, the first anti-particle, and  $\pi$  mesons.

are shown. In the last chapter, the analytical method of calculating the proton cosmic ray spectrum is described and main results are summarized. Best free parameters  $\zeta$ ,  $\Gamma$ , and  $E_{max}^{source}$  for the spectra model modified by LIV coefficients are found via  $\chi^2$  test using measured data of the two largest observatories - Pierre Auger Observatory and Telescope Array. Relation between the LIV coefficients and free parameters  $\zeta$ ,  $\Gamma$  and  $E_{max}^{source}$  is subsequently discussed and an upper bound on the LIV coefficient is given.

# 1. Cosmic rays

Cosmic rays (CR)<sup>1</sup> are mainly charged particles from outer space. Our knowledge about CR and methods of studying cosmic rays vary with their energy. At low energies ( $\sim$ MeV), the CR flux of particles is very high and sophisticated detectors with an active area of a few 100 cm<sup>2</sup> could measure many information about the incoming particles like energy, charge, mass and even the individual isotopes could be identified. However, in the GeV region only relative abundances of elements were identified [2]. The effective surface of the spectrometers is  $\sim$ m<sup>2</sup>. With increasing energy, as the CR flux is getting weaker, the bigger detectors are used and the amount of information about the cosmic ray is getting thinner (Fig.1.1).

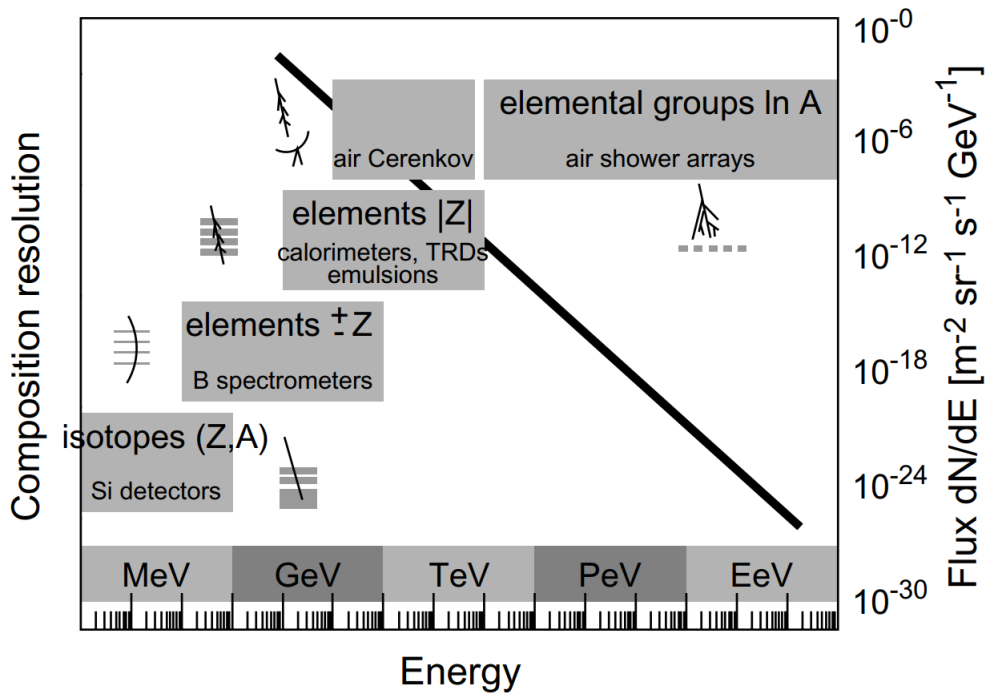


Figure 1.1: Composition resolution as a function of energy. With growing energy less information can be obtained from CR [3].

At highest energies (PeV, EeV) CR are studied indirectly. When a particle of such energies hits atoms in the atmosphere on its arrival a cascade of interactions occurs (also known as shower) as the atmosphere acts as a huge calorimeter. Properties of showers can be measured and information about the CR flux can be derived. To study such extensive air showers, observatories like Pierre Auger Observatory or Telescope Array were built. However, the chemical composition, energy spectrum and also the trajectory of particles are modified during the propagation. There are several reasons behind this. The most important are the interactions with ambient photon fields, effects of the galactic and extragalactic magnetic fields and a cosmological effect - cosmic expansion. In this chapter, general properties of the measured cosmic rays are given and the processes occurring during the proton propagation is explained more in detail.

<sup>1</sup> Photons coming from outerspace are known as X-rays or  $\gamma$ -rays.

## 1.1 Energy spectrum and composition of Cosmic rays

The energy spectrum of CR can be seen on Fig. 1.2. First ( $10^{15}$  eV) and second ( $10^{17}$  eV) breakpoint are known as the knees. Up to the first knee, the particle flux on earth is very high. For example, particles with energies  $\sim 10^{11}$  eV are hitting earth with flux of one particle per second per  $1 \text{ m}^2$ . The origin of the particles between the knees is within our galaxy [4]. The last breakpoint is the ankle. The

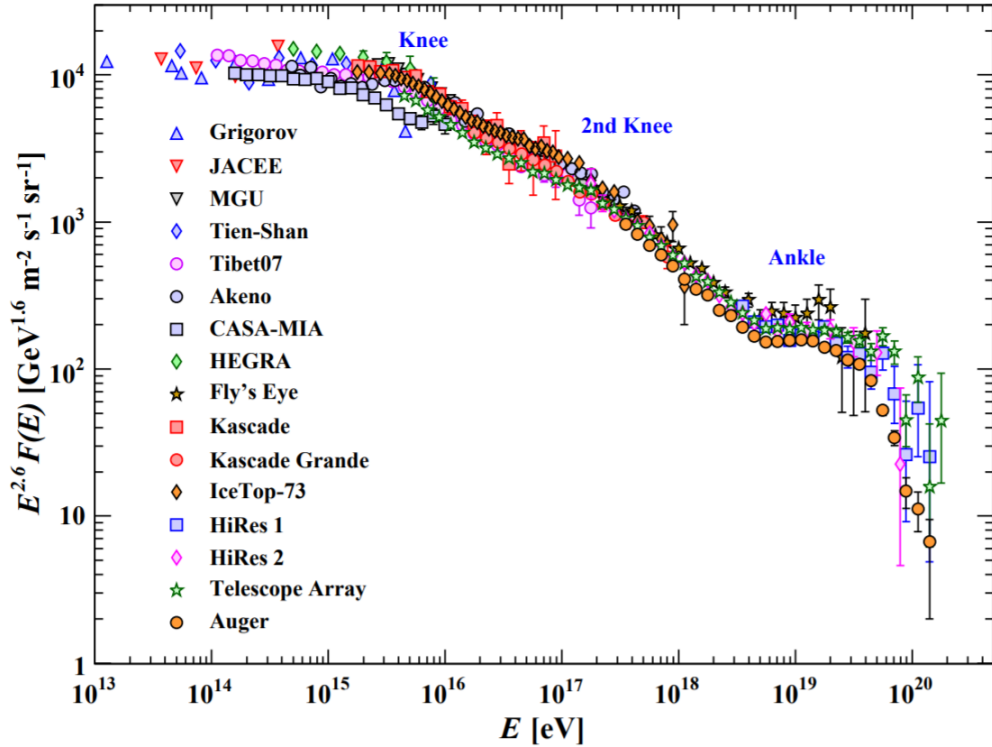


Figure 1.2: Cosmic ray spectrum measured by various observatories [5].

flux of the particles from the ankle is only approximately one particle per  $1 \text{ km}^2$  per year. In the second knee-ankle region it is expected that the origin of the CR is changing from galactic to extragalactic [6]. Above the ankle it is assumed that the origin of CR is purely extragalactic since the Larmor radius of the particles is now much larger than the size of our Galaxy [4, 7]. The corresponding origin of each part of the CR spectrum is shown in Fig.1.3. The last feature of the CR spectrum is a dramatic steepening around the energies about  $10^{19}$  eV caused by the famous Greizen-Zatsepin-Kuzmin (GZK) cutoff named after the authors that came with the idea that proton and Cosmic microwave background (CMB) photon interaction should cause a cutoff in the CR spectrum.

Besides the energy spectrum of the cosmic ray also the composition of the spectrum can be indirectly derived. This is based on the character of so-called showers which differs by its primary. Hadronic showers develop later and deeper in the atmosphere and are transversally wider longer and contain muons and neutrinos in comparison to shower induced by electron (positron) or photon. In order to determine the composition, observables that are sensitive to particle types are used, for instance the position of the depth where the number of particles in the air shower reaches its maximum ( $X_{max}$ ). Identifying the atomic number of

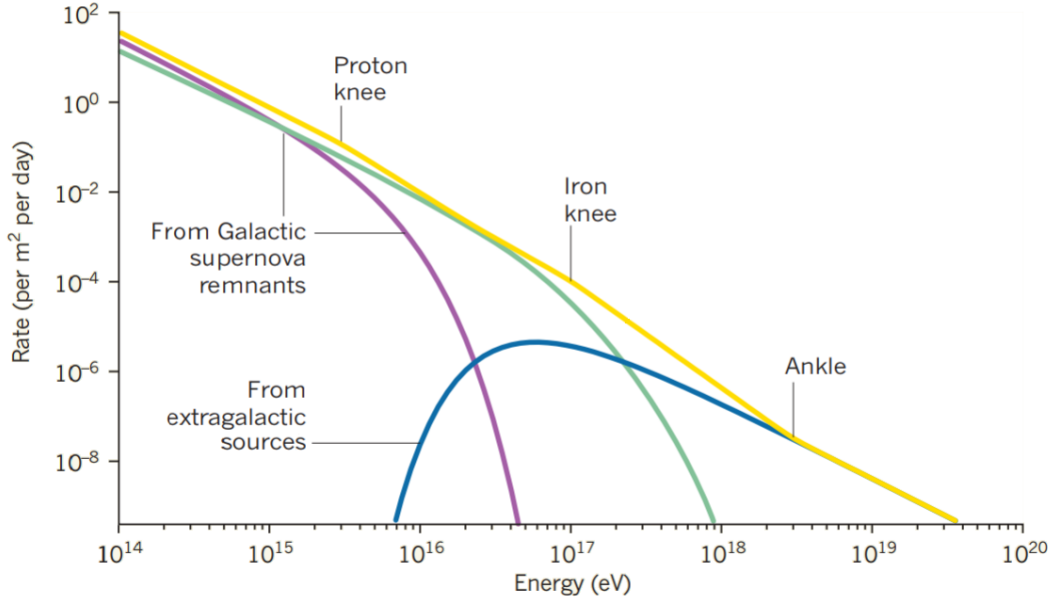


Figure 1.3: The energy spectrum of cosmic rays. Contributions from galactic sources are depicted by red and green line, contributions from extragalactic sources as blue line [8].

primary is complicated since nuclei can not be treated as a mere superposition of  $A$  nucleons since they are not independent. Predictions of the shower parameters (e.g. mean and width of  $X_{max}$  distribution) are obtained by running simulations using transport code (Corsika, Aires, Cosmos) with hadronic interaction models (EPOS, QGSJet, Sibyll) which are extrapolated from lower energy physics. On Fig.1.4 the average depth of maximum shower development ( $\langle X_{max} \rangle$ ) measured by several observatories in comparison with the predictions from simulations is shown. According to the predictions from the simulations (red and blue lines in Fig.1.4), the composition between the knees (between energy  $10^{15}$  eV and  $10^{17}$  eV) is changing from light to heavy. From energy  $10^{17}$  eV, the composition starts to get again lighter and at energy  $10^{18}$  eV it has the lightest composition. By going to higher energies, the composition is getting heavier again.

Since LIV effects are expected to take place at very high energies, we further investigate only the CR spectrum from energy  $10^{19}$  eV. Moreover, we assume a pure proton composition from these energies. This assumption greatly simplifies all our investigation. It is important to stress out that the assumption of the composition based on Fig.1.4 can, in the end, differ from the real one. The discrepancy can be caused, for instance, by unknown (but possible) QCD effects in higher energies.

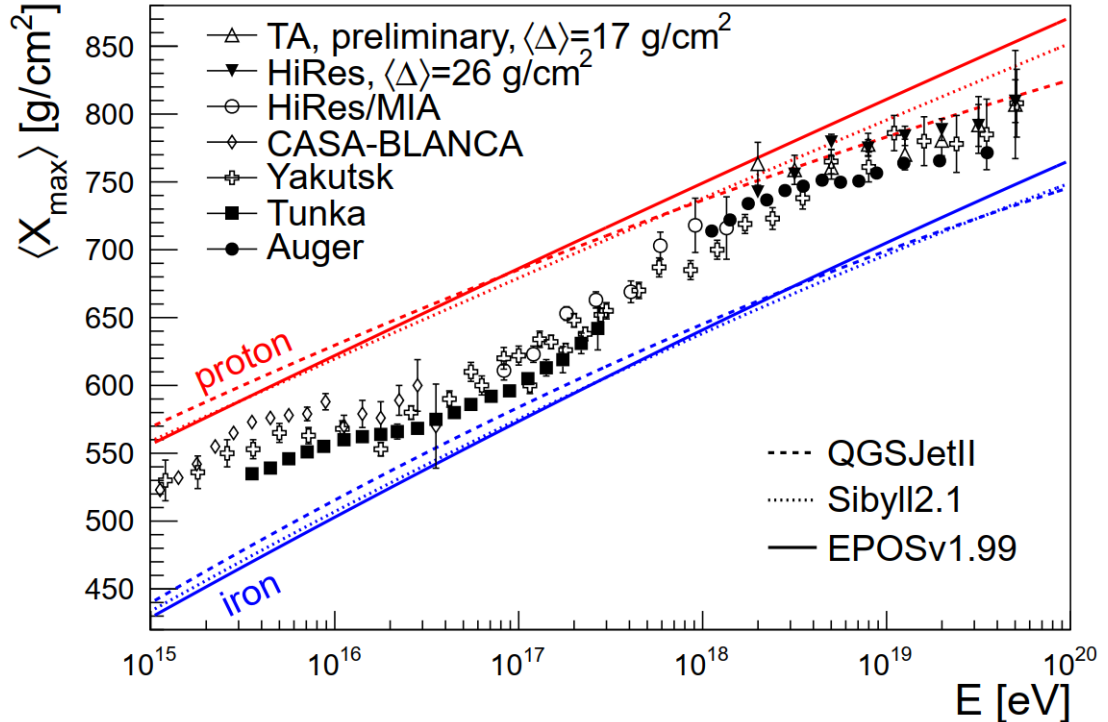


Figure 1.4: Average depth of shower maximum measured as a function of energy by several observatories. The red and blue lines are the predictions extrapolated from lower energy physics [9].

## 1.2 Propagation of proton CR

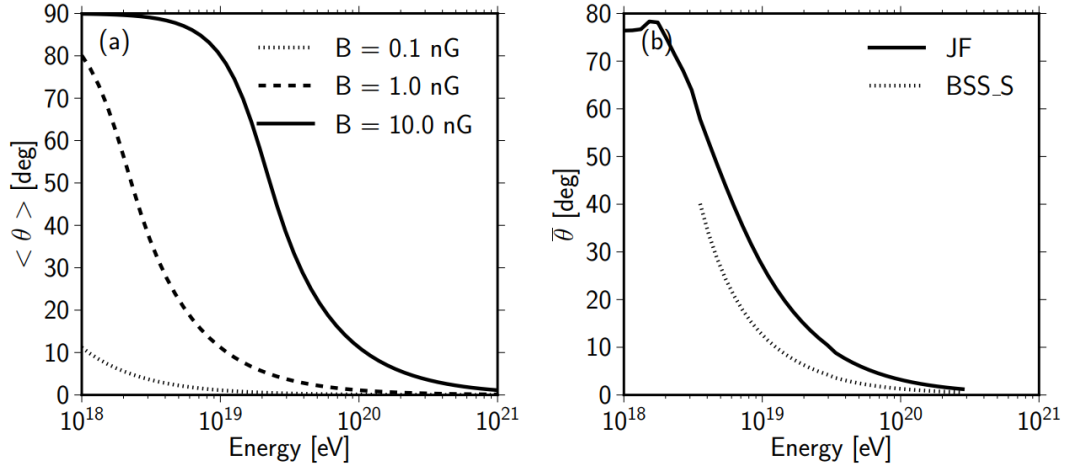
Protons are charged particles and thus are affected by galactic, and extragalactic magnetic fields. Therefore, their trajectories are deflected. Magnitude of the deflection is shown in Fig.1.5. The typical strength of galactic fields is in order of  $\mu\text{G}$ . As for the extragalactic magnetic field, the present upper limit on the strength of the field is  $\leq 0.3$  nG [10]. In both cases in Fig.1.5, it could be seen that the magnitude of deflection is decreasing with increasing proton energy. At proton energy  $10^{19}$  eV, the deflection by the extragalactic magnetic field with  $B = 0.1$  nG is only  $\sim 1^\circ$  (Fig.1.5). Thus, for proton energy above  $10^{19}$  eV effects of the magnetic fields can be neglected and a rectilinear propagation of the proton CR can be assumed.

The only notable effect left during the proton propagation is the energy loss which is provided by two different mechanisms. Firstly, the cosmic expansion of the universe is causing redshift of the particle's energy. The energy losses per time interval caused by the cosmic expansion at present time (redshift  $z = 0$ ) can be calculate as [12]

$$\left( -\frac{1}{E} \frac{dE}{dt} \right)_{ce} = H_0, \quad (1.1)$$

where  $E$  is the proton energy,  $t$  is the time and  $H_0 = 67.8$  km/s/Mpc is the Hubble constant [5].

The second mechanism behind the energy losses are proton collisions with photons from the Cosmic microwave background (CMB). CMB is a relic that



(a) Mean deflection caused by extragalactic magnetic field. (b) Mean deflection caused by galactic magnetic field.

Figure 1.5: Mean deflection of proton cosmic rays as a function of proton energy [11].

comes from early stages of the universe with perfect black body radiation peaked at  $2.75^\circ$  K. There are two types of interactions between proton and CMB photon. Particularly,<sup>2</sup> electron-positron production [13]

$$p + \gamma_{\text{CMB}} \rightarrow p + e^+ + e^-, \quad (1.2)$$

and photomeson production occurring via  $\Delta^+(1232)$  resonance [13]

$$p + \gamma_{\text{CMB}} \rightarrow \Delta^+ \rightarrow p + \pi^0, \quad (1.3)$$

$$p + \gamma_{\text{CMB}} \rightarrow \Delta^+ \rightarrow n + \pi^+, \quad (1.4)$$

with branching ratio 2:1 in favor of  $\pi^0$  production.

The threshold for pair production in the presence of the proton can be simply estimated with the use of four-momenta conservation. After some algebraic simplifications, the proton threshold energy in head on collision is<sup>3</sup>

$$E_{thr} = \frac{m_e(m_p + m_e)}{E_{\text{CMB}}}, \quad (1.5)$$

where  $m_p$  is the proton mass,  $m_e$  is the electron mass and  $E_{\text{CMB}}$  is energy of the CMB photon. For the CMB peak temperature  $T = 2.73^\circ$  K = 0.24 meV this yields threshold  $\sim 2 \times 10^{18}$  eV. Since this reaction can be described by quantum electrodynamics, an exact energy losses can be calculated purely theoretically [14]. General formula that well describes energy losses by pair production was

<sup>2</sup> Legend for the used symbols:  $p$  is proton  $e^-$  is electron,  $e^+$  is positron,  $\Delta^+$  is delta resonance,  $\gamma_{\text{CMB}}$  is the CMB photon,  $\pi^0$  is pion with neutral charge and  $\pi^+$  is pion with positive charge.

<sup>3</sup> The constant  $c$  was set to 1.

worked out by Blumenthal [15]. The resulting formula for the energy losses by pair production at present time (redshift  $z = 0$ ) has the following form [15]

$$\left(-\frac{dE}{dt}\right)_{e^+e^-} = \frac{\alpha r_0^2 (m_e c^2 \omega_0)^2}{\pi^2 \hbar^3 c^3} f(\nu), \quad (1.6)$$

where  $\alpha$  is fine-structure constant,  $r_0$  is the classical electron radius,  $m_e$  is electron mass and  $\omega_0$  is defined as  $\omega_0 = k.T = 2.35 \times 10^{-4}$  eV with  $k$  as the Boltzmann constant and  $T$  as the peak temperature of the CMB. The function  $f(\nu)$  is defined as [15]

$$f(\nu) = \nu^2 \int_2^\infty d\xi \phi(\xi) (e^{\nu\xi} - 1)^{-1}, \quad (1.7)$$

where  $\xi = \epsilon/m_e c^2$  with  $\epsilon$  as the photon energy measured in proton rest frame<sup>4</sup>,  $\nu = m_e c^2 / (2\gamma\omega_0)$  with  $\gamma$  as the Lorentz factor that connects proton rest frame with LAB (laboratory) frame<sup>5</sup>. Parametrization for the function  $\phi(\xi)$  that was used in this thesis can be found in Ref.[16].

The threshold for photomeson production can be estimated by use of the conservation of the four-momenta. This yields for head on collision for the proton threshold energy<sup>6</sup>

$$E_{thr} = \frac{m_\pi(m_\pi + 2m_p)}{4E_{CMB}}, \quad (1.8)$$

where  $m_\pi$  is the mass of the pion and  $m_p$  is the mass of the proton,  $E_{CMB}$  is the energy of CMB photon. By using the peak temperature of CMB photon, one will obtain value for the threshold  $\sim 3.5 \times 10^{19}$  eV.

With the further rise of the photon energy, higher heavier baryon resonance  $\Delta(1620)$  and  $\Delta(1700)$  are created. Going even to higher photon energies, diffractive production of vectormeson  $\rho$  and  $\omega$  starts. At the highest energies, direct multi-pion production takes place.

The formula for energy losses by photomeson production at present time (redshift  $z = 0$ ) is given by [17]

$$\left(-\frac{1}{E} \frac{dE}{dt}\right)_\pi = \frac{\omega_0 c}{2\pi^2 \gamma^2 \hbar^3 c^3} \int_\eta^\infty d\epsilon \epsilon \sigma(\epsilon) K(\epsilon) \ln(1 - e^{-\frac{\epsilon}{2\gamma\omega_0}}), \quad (1.9)$$

where  $\sigma(\epsilon)$  is the cross-section of the proton-photon interaction,  $\gamma$  is the Lorentz factor that connects LAB frame with the proton rest frame,  $\epsilon$  is the energy of the photon in proton rest frame,  $E$  is energy of the proton in the LAB frame,  $\eta$  is the threshold energy for the interaction and  $\omega_0$  is defined same as in Eq.(1.6). The inelasticity  $K$  is defined as a mean fraction of energy lost by a proton in one proton-photon collision in the laboratory system and is given as [17]

$$K = 1 - \frac{\langle E_f \rangle}{E_i}, \quad (1.10)$$

<sup>4</sup> Proton rest frame is frame of reference where proton momentum is null.

<sup>5</sup> LAB frame is frame of reference from where is the proton energy measured.

<sup>6</sup> The constant  $c$  was set to 1.

where  $E_i$  and  $E_f$  is the energy of the incoming and outgoing proton. The calculation for the inelasticity can be found for instance in Ref.[18]

$$K = \frac{1}{2} \left( 1 + \frac{m_\pi^2 - m_p^2}{s} \right), \quad (1.11)$$

where  $s$  is the invariant mass of the interacting particles. Fig.1.6 shows values of inelasticity for proton energy (LAB frame) range  $10^{19.5} - 10^{22}$  eV and photon energy (proton rest frame) range  $0.2 - 4$  GeV. The inelasticity is the same for all proton energies and varies only with photon energies. The inelasticity, for photon energies greater than 4 GeV remains approximately constant.

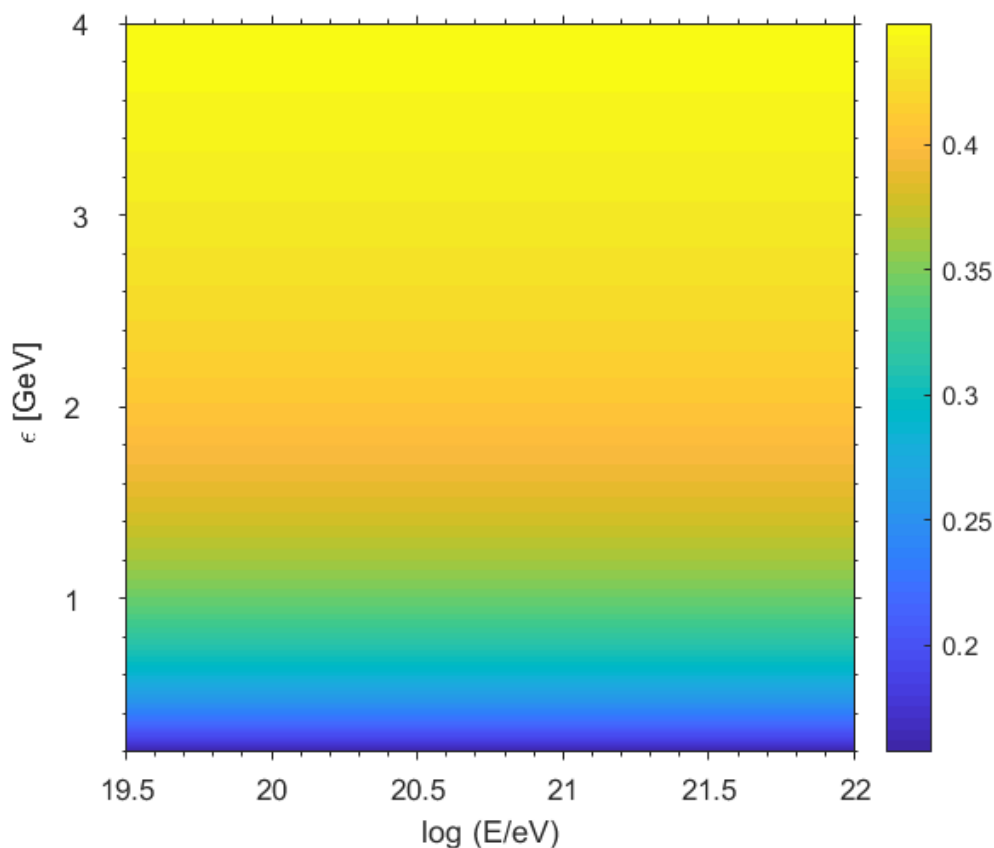


Figure 1.6: Inelasticity (color scale) as a function of proton energy measured in LAB frame (x-axis) and photon energy measured in proton rest frame (y-axis).

In this work, widely accepted parametrization for the proton-photon cross-section made by Rachen [19] is used. In Fig.1.7 this parametrization is compared to the experimental data taken from Ref.[20]. The first peak, the highest one, corresponds to the delta resonance. Using Eq.(1.9), the attenuation length<sup>7</sup> of the proton in the CMB can be calculated as [21]

$$\lambda = c \left( -E^{-1} \frac{dE}{dt} \right)_\pi^{-1}. \quad (1.12)$$

<sup>7</sup> Attenuation length is distance where about 63% of the particles from beam have been stopped.

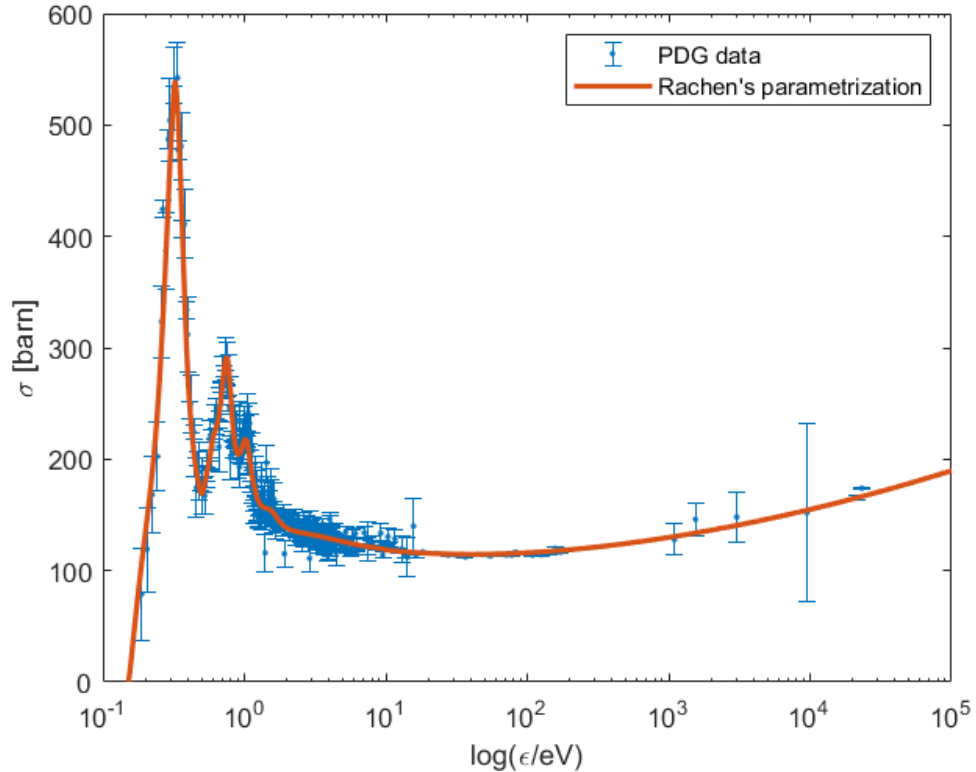


Figure 1.7: Proton-photon cross-section for the photomeson production as a function of the photon's energy in the proton rest frame. Data with errorbars are taken from Ref.[5] and the red line is the parametrization of the proton-photon cross-section from Ref.[14].

The result is shown in Fig.1.8. In this figure is shown that the proton attenuation length at the beginning is exponentially decreasing and from energies about  $10^{20.7}$  eV a constant value of 1 Mpc is established.

The energy losses by cosmic expansion, pair production and photomeson production for energies in the energy range  $10^{17}$  -  $10^{23}$  eV at present time (redshift  $z = 0$ ) were calculated by using Eqs.(1.1), (1.6) and (1.9). These losses are together compared in Fig.1.9.

For proton energies below the threshold for proton-photon interactions, the only mechanism of energy loss is the cosmic expansion. At the energy about  $2 \times 10^{18}$  eV the process of pair production starts and produce losses approximately one half of order of magnitude higher than by those caused by the cosmic expansion. After hitting the threshold for the photomeson production, the energy losses are nearly two orders of magnitude higher than the other ones, i.e. all other effect are therefore negligible.

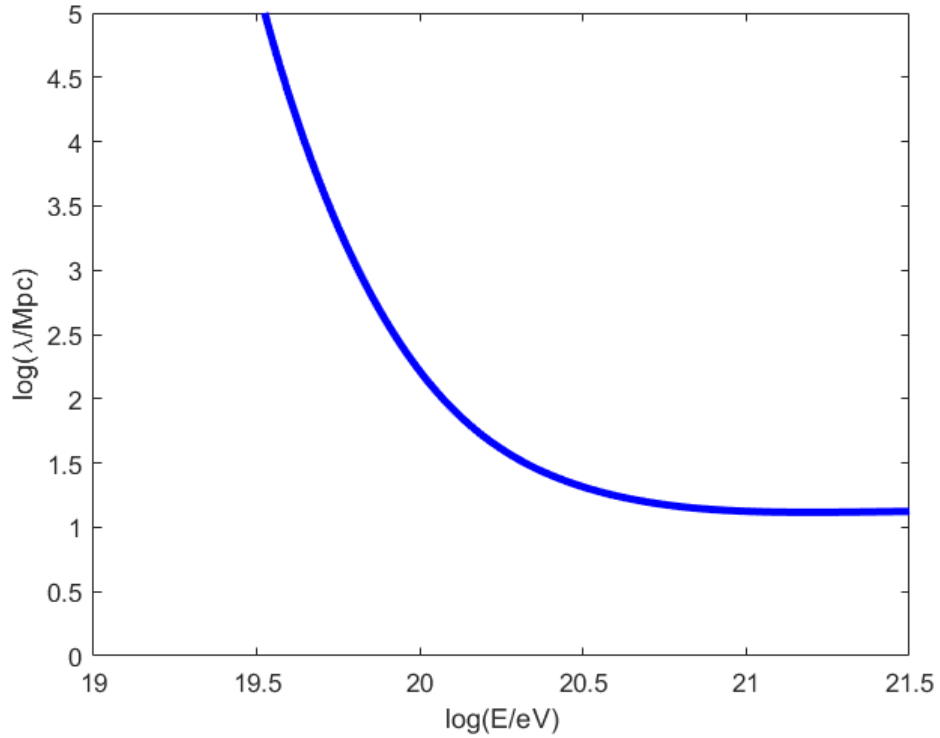


Figure 1.8: Proton attenuation length as a function of proton energy. Calculated using Eq.(1.12).

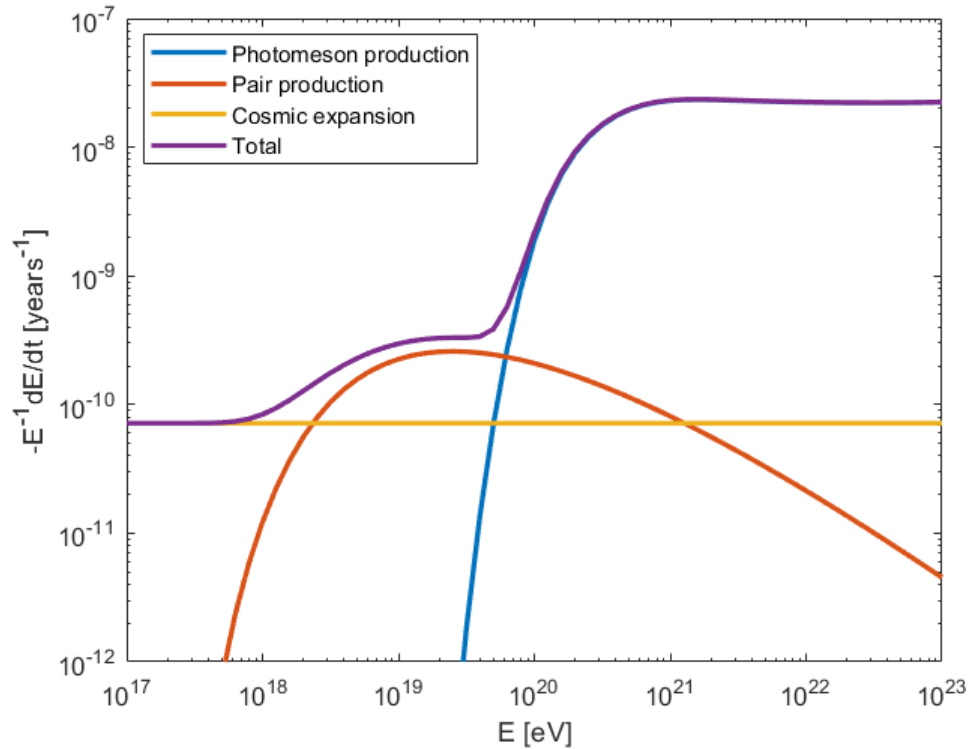


Figure 1.9: Proton energy losses at present time (redshift  $z = 0$ ) as a function of proton energy caused by cosmic expansion (orange), pair production (red), photomeson production (blue) and their sum (violet). Plot was made by calculating Eqs.(1.1), (1.6) and (1.9).

### 1.3 Energy evolution of proton CR

The calculated energy losses shown in Fig.1.9 by Eqs.(1.1), (1.6) and (1.9) are valid for present time, i.e. for zero redshift ( $z = 0$ ). However, the energy losses do change with redshift. The energy losses caused by cosmic expansion at arbitrary redshift are given by [17]

$$\left(-\frac{1}{E} \frac{dE}{dt}(z)\right)_{ce} = H(z), \quad (1.13)$$

where

$$H(z) = H_0 \sqrt{\Omega_r(1+z)^4 + \Omega_m(1+z)^3 + \Omega_K^2 + \Omega_\Lambda}. \quad (1.14)$$

where  $H_0$  is the same as in Eq.(1.1). The  $\Omega_r$  stand for the radiation abundances,  $\Omega_m$  for matter abundances,  $\Omega_\Lambda$  for the vacuum energy and the  $\Omega_K$  stands for the curvature of the universe. The magnitude of the redshift loss depends on the cosmological model of the universe. Currently, the most accepted model of the universe is a flat ( $\Omega_K = 0$ )  $\Lambda$ CDM universe with the following abundances:  $\Omega_r = 0.002$ ,  $\Omega_m = 0.308$  and  $\Omega_\Lambda = 0.692$  [5]. These values are used for all the calculations in this thesis, and since the radiation abundance  $\Omega_r$  is small in comparison to the other abundances, it is neglected.

Because the density of the CMB increase as  $(1+z)^3$  and the energy of photons as  $(1+z)$ , the collisional energy losses (pair production - Eq.(1.6) and photomeson production - Eq.(1.9)) at arbitrary redshift are given by [17]

$$\left(-\frac{1}{E} \frac{dE}{dt}(z)\right)_{e^+e^-, \pi} = (1+z)^3 \left(-\frac{1}{E'} \frac{dE'}{dt}\right)_{e^+e^-, \pi}. \quad (1.15)$$

where  $E' = (1+z)E$  with  $E$  as proton energy measured on Earth. The differential formulas for the energy losses per time interval at arbitrary redshift  $z$  (Eqs.(1.13) and (1.15)) can be rewritten as energy losses per redshift interval with the help of the following relation

$$dt = -\frac{1}{H(z)(1+z)} dz. \quad (1.16)$$

The final form of the equations for energy loss by cosmic expansion, pair production and photomeson production at arbitrary redshift per redshift interval is

$$\left(\frac{dE}{dz}(z)\right)_{ce} = E \frac{1}{(1+z)}, \quad (1.17)$$

$$\left(\frac{dE}{dz}(z)\right)_{e^+e^-} = \frac{1}{H(z)(1+z)} \frac{\alpha r_0^2 (mc^2 \omega_0)^2}{\pi^2 \hbar^3 c^3} f(\nu), \quad (1.18)$$

$$\left(\frac{dE}{dz}(z)\right)_\pi = E \frac{1}{H(z)} \frac{\omega_0 c}{2\pi^2 \gamma^2 \hbar^3 c^3} \int_\eta^\infty d\epsilon \epsilon \sigma(\epsilon) K(\epsilon) \ln(1 - e^{-\frac{\epsilon}{2\gamma\omega_0(1+z)}}). \quad (1.19)$$

The respective variables and constants are explained at Eqs.(1.6), (1.9) and (1.14). The differential equations Eqs.(1.17), (1.18) and (1.19) were numerically solved for the increasing redshift with Runge-Kutta fourth order method for flat  $\Lambda$ CMD universe and also for matter-dominated universe. The result is shown on Fig.1.10. The functions plotted in Fig.1.10 can be interpreted as the proton energy evolu-

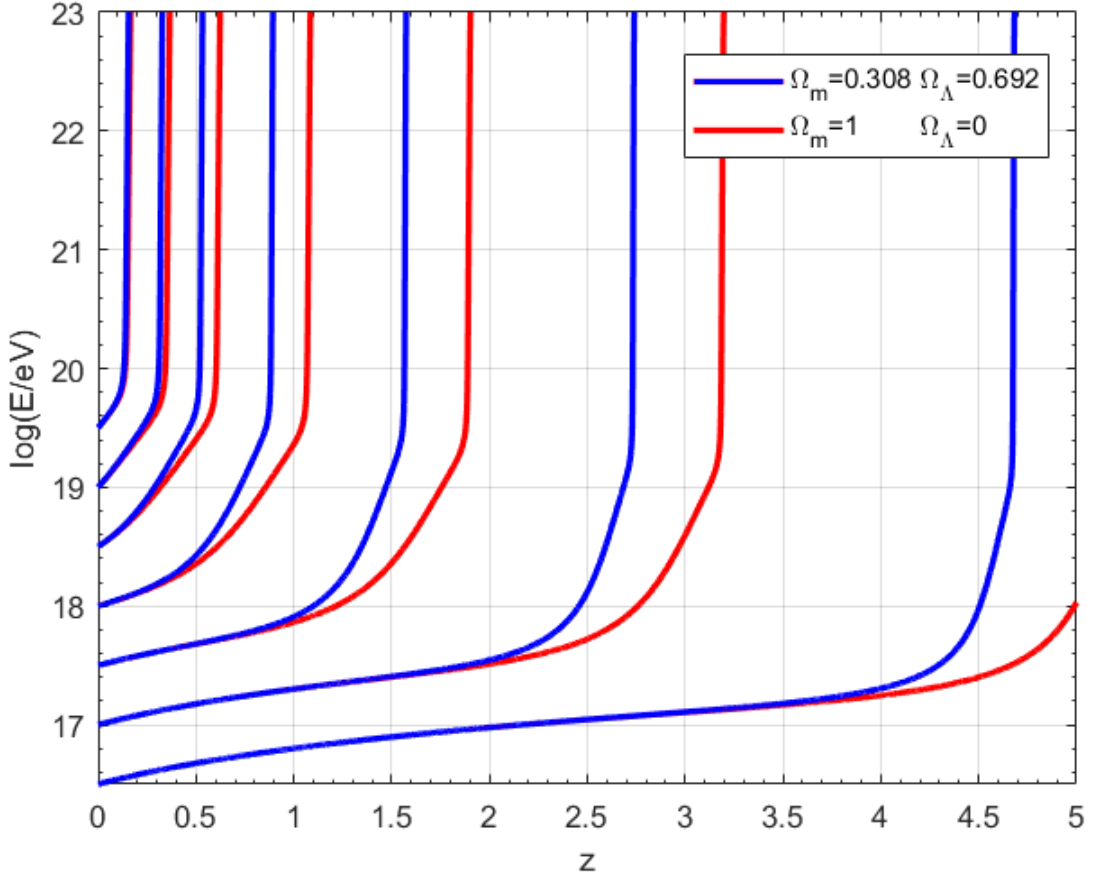


Figure 1.10: Proton's energy evolution as a function of redshift. Blue lines represent  $\Lambda$ CMD universe, red ones are for flat matter dominated universe. Each line connects particle's energy in different redshifts.

tion since they relate the proton energy at redshift  $z = 0$ , i.e., measured at the earth at present time with the energy that particle had before at a redshift  $z$ . The dominant mechanism of the energy loss at particular epoch can be distinguished by looking at the functions plotted in Fig.1.10. The increasing linear part corresponds to losses by cosmic expansion and ends at some  $z_p$  when an exponential part associated with the pair production begin to take place. Moving to higher redshifts, at the second breakpoint ( $z_\pi$ ) a rapid steepening caused by photomeson production occurs. After the epoch  $z_\pi$ , the proton energy rises very quickly so that for significantly higher  $z \gg z_\pi$  the energy of proton would be unphysically

high. This epoch can be therefore considered as the border of the confinement volume transparent to CR protons measured at the earth ( $z = 0$ ) with energy  $E$  [14].

The difference between energy evolution functions for different cosmological models is manifested in higher redshifts, in a region dominated by pair production. It can be clearly seen that exponential part becomes flatter in the matter-dominated universe, shifting the epoch  $z_\pi$  further. For smaller redshifts and the epochs affected by cosmic expansion losses and photomeson production, there is no noticeable change.

Fig.1.11 shows magnified part from Fig.1.10, in order to examine energy evolution of proton with extreme energies. Now, the parts of lines that in Fig.1.10 appeared perpendicular to x-axis (photomeson energy loss region) are sloped. With higher energies the redshift and pair production regions of the curves are gradually disappearing and for energy around  $10^{20.5}$  eV only the photomeson region is visible.

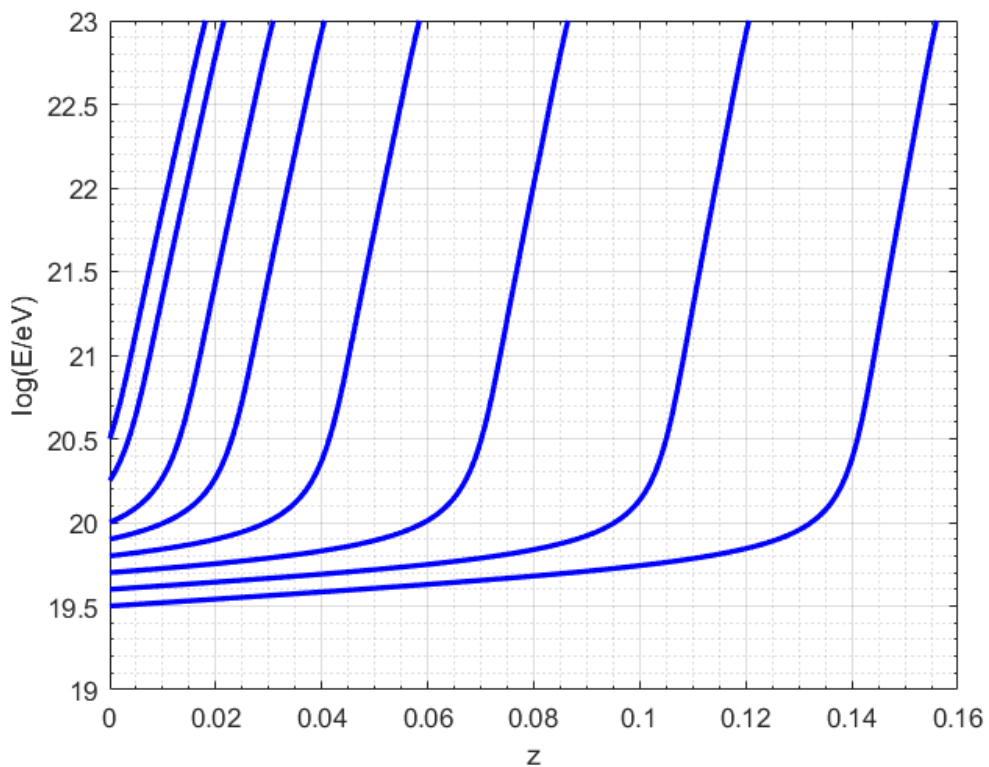


Figure 1.11: Proton energy evolution as a function of redshift. A magnified part from Fig.1.10. Parts of lines that correspond to epoch dominated by photomeson energy losses are sloped with respect to x-axis.

The rapid increase of the proton energy at redshifts  $z \gg z_\pi$  to unphysically high energies (Figs.1.10 and 1.11) can be avoided by setting the maximal acceleration energy at the source ( $E_{max}^{source}$ ). The redshift where the proton reach  $E_{max}^{source}$  can be considered as an effective horizon of transparency, i.e., the hypothetical effective distance of the source. Further, in this thesis, it is shortly referred as Effective horizon.

Hillas [22] suggested the simplest way to estimate the maximal energies at the source. The idea is that the particle which escapes from the source where it

was being accelerated, will be unable to gain more energy. Thus, the maximal attainable energy of the particle depend on the magnetic field and diameter of the source. According to this the maximal energy of the particle, produced at the source can be expressed as [22]

$$E_{max}^{source} = qBR, \quad (1.20)$$

where  $q$  is charge of the particle,  $B$  is the magnetic field at the source, and  $R$  is the diameter of the source. It has to be remembered that this is only rather an approximation. For more precise calculations one might also include radiation losses [23]. Astronomical objects with their respective sizes and magnetic fields are shown in Fig.1.12. The objects below the upper slope cannot accelerate protons to  $10^{21}$  eV. For example, pulsars<sup>8</sup> can theoretically provide the largest acceleration.

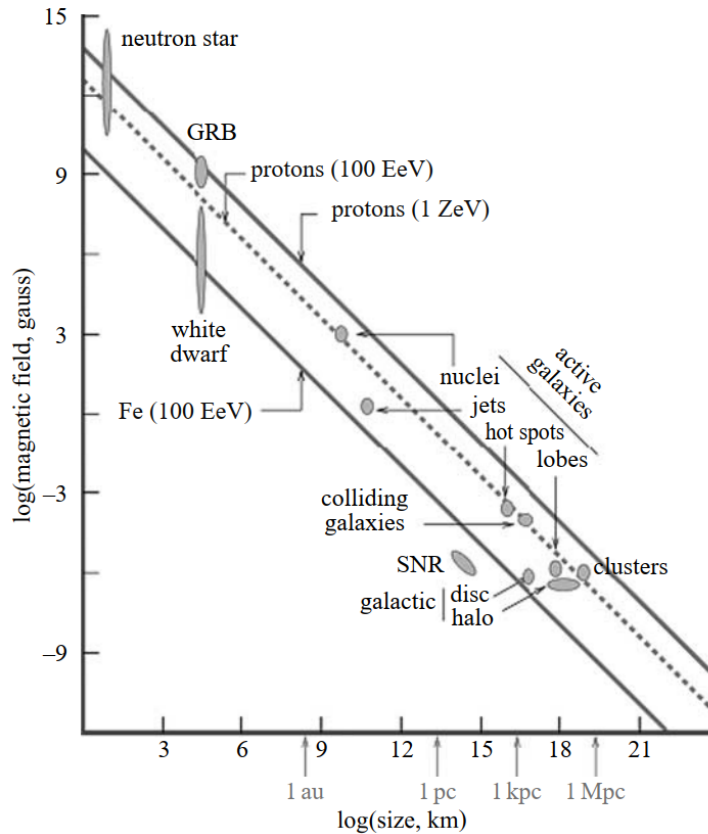


Figure 1.12: Hillas plot [24]. Astronomical objects with their respective size and magnetic field are depicted. The objects below the upper sloped cannot accelerate protons to  $10^{21}$  eV.

By taking values for a typical pulsar, diameter 40 km and magnetic field  $B=10^{16}$  G one gets maximal energy of acceleration  $E_{max}^{source} = 5 \times 10^{23}$  eV. Taking in account the energy losses during the acceleration process we make an estimate of  $E_{max}^{source} = 10^{23}$  eV. However, this scenario should be considered as an extreme case. The usually assumed maximal energy at sources is lower. Therefore, we used maximal energy scenarios from  $E_{max}^{source} = 10^{20.5}$  eV up to  $E_{max}^{source} = 10^{23}$  eV

<sup>8</sup> Pulsars are types of neutron stars.

with step of  $10^{0.05}$  eV to calculate the effective horizon. In Fig.1.13 the effective horizon is shown as a function of the proton's energy measured on Earth for these maximal energy scenarios.

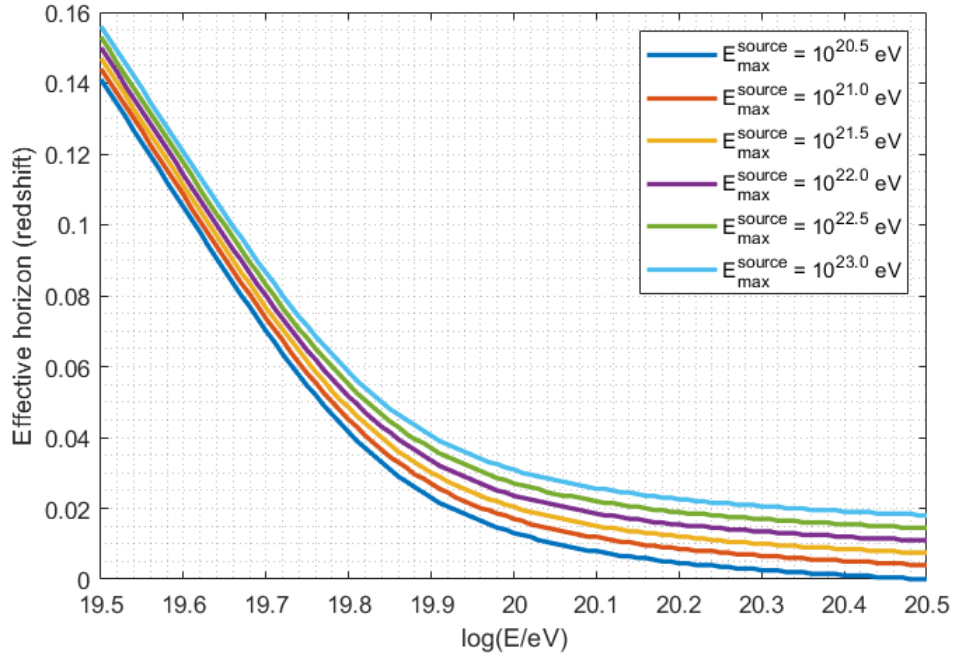


Figure 1.13: Effective horizon (in redshift  $z$ ) as a function of the proton energy measured on Earth. Lines represent different proton maximal energy at source scenario.

At first the horizon is approximately exponentially decreasing. From values about  $10^{20.2}$  eV it remains nearly constant despite a further increase of the proton energy. The precise values of the effective horizon, in units of Mpc, are summarized in Tab.1.1. Below proton energies  $E = 10^{20}$  eV, the horizon for all  $E_{max}^{source}$  scenarios is in the order of hundreds of Mpc. Above proton energies about  $E = 10^{20}$  eV, the horizon is in the order of tens Mpc.

Table 1.1: Effective horizons in Mpc given for various maximal energies at source ( $\log(E_{max}^{source}/\text{eV})$  in columns) and proton energies measured on Earth ( $\log(E_{z=0}/\text{eV})$  in rows).

	<b>20.5</b>	<b>21</b>	<b>21.5</b>	<b>22</b>	<b>22.5</b>	<b>23</b>
<b>19.5</b>	603	615	628	640	652	665
<b>19.6</b>	453	468	478	491	506	518
<b>19.7</b>	305	320	332	347	360	375
<b>19.8</b>	182	197	212	225	240	255
<b>19.9</b>	101	119	132	147	162	178
<b>20.0</b>	57	75	90	103	119	136
<b>20.1</b>	35	53	66	82	97	112
<b>20.2</b>	20	38	53	68	84	99
<b>20.3</b>	11	29	44	60	75	90
<b>20.4</b>	4	22	38	53	68	84
<b>20.5</b>	0	18	33	49	64	79

## 2. Effects of LIV on the propagation of proton CR

Nowadays, Lorentz symmetry is cornerstone of our two best theories for describing the Universe we live in, the General relativity and the Standard model. We also know, that these are not the ultimate theories since they do not provide all answers to unresolved problems. Also, it is believed that these theories are valid only on presently accessible energy scales. They are considered as a low-energy limit of a more fundamental theory at the Planck scale ( $10^{19}$  GeV).

In 1989 Kostelecky [25] had shown the possibility of a spontaneous breakdown of Lorentz symmetry in string theory explored through covariant string field theory. Kostelecky [25] also suggested a potential mechanism for Lorentz breaking that could be generic for other string theories. This triggered the interest of the scientific community in Lorentz violation. Afterwards, the idea of breaking the Lorentz invariance (LI) was investigated in other quantum gravity models, e.g., warped brane worlds [26], and loop quantum gravity [27].

Lorentz violation is also incorporated in many other theories, for instance, emergent gauge bosons [28], varying moduli [29], axion-Wess-Zumino models [30], analogues of emergent gravity in condensed matter [31], ghost condensate [32], space-time varying couplings [33], or varying speed of light cosmologies [34].

The search for a signal of Lorentz violation is highly motivated since it could pave the way to beyond standard model physics.

### 2.1 LIV framework

One of the most commonly used kinematic LIV framework is modified dispersion relation. The following formalism can be found for instance in Ref.[35] and Ref.[36]. The main idea of this framework is the addition of some function  $\Delta(\vec{p})$  to the dispersion law  $E^2 = p^2 + m^2$ , while keeping energy-momentum conservation laws.<sup>1</sup> Thus, the modified form of dispersion relation is [36]

$$E^2 = p^2 + m^2 + \Delta(\vec{p}), \quad (2.1)$$

where  $E$  and  $\vec{p}$  is the energy and momentum of the particle and  $\Delta(\vec{p})$  is a function of momentum containing LIV correction terms. At small energies (and momentum) the standard expression  $E^2 = p^2 + m^2$  has to be recovered. Based on this, the LIV function  $\Delta(\vec{p})$  can be expanded around  $\vec{p} \sim 0$ . This yields [36]

$$\Delta(\vec{p}) = \tilde{\eta}_i^{(1)} p^i + \tilde{\eta}_{ij}^{(2)} p^i p^j + \tilde{\eta}_{ijk}^{(3)} p^i p^j p^k + \tilde{\eta}_{ijkl}^{(4)} p^i p^j p^k p^l + \dots \quad , \quad (2.2)$$

where  $\tilde{\eta}_i, \tilde{\eta}_{ij}, \tilde{\eta}_{ijk}, \dots$  are the LIV correction coefficients, and the terms are summed over all the values of the index (Einstein summation convention). While having a broken rotation Lorentz subgroup, one must always have broken boost subgroup.

<sup>1</sup> The constant  $c$  is set to 1 in all the calculations in this section.

However, this does not apply vice-versa. In LIV frameworks the boost subgroup will be either way broken [36]. Imposing this, "weaker" condition to neglect any violation of rotational symmetry, the expression in Eq.(2.2) simplifies to [36]

$$\Delta(|p|) = \tilde{\eta}^{(1)}|p|^1 + \tilde{\eta}^{(2)}|p|^2 + \tilde{\eta}^{(3)}|p|^3 + \tilde{\eta}^{(4)}|p|^4 + \dots \quad (2.3)$$

Since the LIV is assumed to be relevant around the Planck scales, it is appropriate to have the terms  $\tilde{\eta}^n$  suppressed by the Planck mass ( $M_{Pl} = 2.4 \times 10^{18}$  GeV) to the power  $n$ . This can be done only for terms with  $3 \geq n$  [36]. However from the pattern  $\frac{1}{M_{Pl}^{n-2}}$  one would expect the lower terms  $n=2$  to be unsuppressed and the  $n=1$  term to be even more important [36]. There is some symmetry, or some other mechanism that protects the lower dimension operators from strong LIV or the suppression of the order of suppression by Planck mass is more than  $\frac{1}{M_{Pl}^{n-2}}$  [36]. Such symmetry for instance, can be Supersymmetry [36]. In order to avoid this problem, a mass scale  $\mu$  of the particle with LIV correction can be introduced to the terms, specifically [36]

$$\tilde{\eta}^{(1)} = \eta_1 \frac{\mu^2}{M_{Pl}}, \quad \tilde{\eta}^{(2)} = \eta_2 \frac{\mu}{M_{Pl}}, \quad \tilde{\eta}^{(3)} = \eta_3 \frac{1}{M_{Pl}}, \quad \tilde{\eta}^{(4)} = \eta_4 \frac{1}{M_{Pl}^2}, \dots \quad (2.4)$$

Here, the LIV corrections  $\eta_n$  are now dimensionless. In this thesis mass scale  $\mu = 1$  GeV is used. Thus, the LIV correction term in the expanded form is [36]

$$\Delta(|p|) = \eta_1 \frac{\mu^2}{M_{Pl}}|p| + \eta_2 \frac{\mu}{M_{Pl}}|p|^2 + \eta_3 \frac{1}{M_{Pl}}|p|^3 + \eta_4 \frac{1}{M_{Pl}^2}|p|^4 + \dots \quad (2.5)$$

and the full form of modified dispersion relation is [36]

$$E^2 = m^2 + p^2 + \eta_1 \frac{\mu^2}{M_{Pl}}|p| + \eta_2 \frac{\mu}{M_{Pl}}|p|^2 + \eta_3 \frac{1}{M_{Pl}}|p|^3 + \eta_4 \frac{1}{M_{Pl}^2}|p|^4 + \dots \quad (2.6)$$

For high energy processes such that  $p^2 \gg \Delta(|p|) + m^2$  we can interchange the momentum  $p$  with energy  $E$  in Eq.(2.5) and Eq.(2.6) [17]. Therefore,

$$\Delta(E) = \eta_1 \frac{\mu^2}{M_{Pl}}E + \eta_2 \frac{\mu}{M_{Pl}}E^2 + \eta_3 \frac{1}{M_{Pl}}E^3 + \eta_4 \frac{1}{M_{Pl}^2}E^4 + \dots \quad (2.7)$$

$$E^2 = m^2 + p^2 + \eta_1 \frac{\mu^2}{M_{Pl}}E + \eta_2 \frac{\mu}{M_{Pl}}E^2 + \eta_3 \frac{1}{M_{Pl}}E^3 + \eta_4 \frac{1}{M_{Pl}^2}E^4 + \dots \quad (2.8)$$

It is important to note that, in principle, the LIV terms can be different for individual particles, since there is no argument excluding such behavior.

In case of the composite particles, the LIV terms can be inferred by addition. If  $\mathbb{N}$  particles with momentum  $p$  and mass  $m$  are combined, the total energy, momentum and mass is,  $E_{tot} = \mathbb{N}E$ ,  $p_{tot} = \mathbb{N}p$  and  $m_{tot} = \mathbb{N}m$ . Thus, the dispersion relation is [36]

$$E_{tot}^2 = p_{tot}^2 + m_{tot}^2 + \mathbb{N}^2 \Delta(|p|). \quad (2.9)$$

There are several consequences of the modified dispersion relation. Some interactions that are not kinematically allowed can become possible. For instance,<sup>2</sup> the photon splitting  $\gamma \rightarrow e^+ + e^-$  or pair annihilation  $e^+ + e^- \rightarrow \gamma$  can happen since the LIV terms takes care of the momentum conservation [37]. Moreover, photon annihilation  $\gamma + \gamma \rightarrow e^+ + e^-$  or photon splitting  $\gamma \rightarrow \mathbb{N}\gamma$  can also happen and under assumption of LIV it is possible for neutrinos to oscillate without mass [37]. In the preferred frame each particle can has its maximal velocity [38]. Thus, it is possible for particles to travel faster than photons [38]. When particle exceeds the speed of light, a vacuum Cherenkov effect occur, for instance  $p \rightarrow p + \gamma$ ,  $e^- \rightarrow e^- + \gamma$  or even  $\nu \rightarrow \nu + \gamma$ , since neutrinos still have a charge structure in the standard model [37]. Also, gravitational Cherenkov radiation can occur if matter moves faster than the phase velocity of gravitons in a vacuum [37]. Non-observation of these forbidden effects can be used for constraining LIV terms, what was already done, for instance in Ref.[37].

The mentioned constraints done by forbidden interactions belong to the category of an astrophysical test of LIV [35]. Astrophysics is more suited for directly constraining higher dimension operators as the Lorentz violating effects scale with energy [35]. Other commonly used tests are for instance, Time of flight tests [39], Birefringence test [40] or test by Synchrotron radiation [41].

Terrestrial experiments are, on the other hand, invariably concerned with low energy processes [35]. They are therefore best suited for looking at the lower dimension operators. The principle of these test is that Earth-based laboratories will see slightly different local physics as the planet rotates and revolves. The results of performed experiments from different periods are subsequently compared. Some of the most commonly used terrestrial tests are, for instance, done by using Penning traps [42], Clock comparison experiments [43], Cavity experiments [43], Spin-polarized torsion balances [44], Neutral mesons [45], Doppler shift of lithium [46], Muon experiments [47] and Nuclear Spin Experiments [48].

## 2.2 Modified kinematics

At the beginning, we made an assumption of a pure proton composition for CR spectrum from energy  $10^{19}$  eV. The most relevant physical process for the protons with such extreme energies is the energy loss by photomeson production<sup>3</sup>

$$p + \gamma_{\text{CMB}} \rightarrow \Delta^+ \rightarrow N + \pi, \quad (2.10)$$

governed by Eq.(1.9). The quantity that is changed by LIV in Eq.(1.9) is the inelasticity. The presented way of calculating the LIV modified inelasticity was first derived by Alfaro and Palma [17] and was subsequently used in a number of

<sup>2</sup> Legend for the used symbols:  $e^+$  is positron,  $e^-$  is electron,  $\gamma$  is photon,  $\nu$  is neutrino,  $p$  is proton and  $\mathbb{N}$  is number of particles.

<sup>3</sup> Legend for the used symbols:  $p$  is proton,  $\gamma_{\text{CMB}}$  is the CMB photon,  $\Delta^+$  is delta resonance,  $N$  is nucleon (proton or neutron),  $\beta$  is pion with neutral or positive charge.

other papers, for instance, in Refs.[21, 49]. Here we present a brief derivation of the modified inelasticity.<sup>4</sup> For more details see Ref.[17].

The feature of the Lorentz invariance violation is that it also introduce a preferred system. In the derivation it is assumed that the preferred system denoted by the presence of LIV is the same as CMB comoving reference frame and is used as the laboratory system (LAB) [17].

According to Eq.(2.7) and Eq.(2.8) the dispersion relations for a nucleon  $N$ , pion  $\pi$  and proton  $p$  from Eq.(2.10) can be written as [17]

$$E_N^2 - p_N^2 = \Delta_N(E_N) + m_N^2 = s_N(E_N), \quad (2.11)$$

$$E_\pi^2 - p_\pi^2 = \Delta_\pi(E_\pi) + m_\pi^2 = s_\pi(E_\pi), \quad (2.12)$$

$$E_p^2 - p_p^2 = \Delta_p(E_p) + m_p^2 = s_p(E_p), \quad (2.13)$$

where  $E_N, E_\pi, E_p$  are energies and  $\vec{p}_N, \vec{p}_\pi, \vec{p}_p$  are momenta of nucleon, pion and proton measured in LAB frame and  $m_N, m_\pi$  and  $m_p$  are their respective masses. The  $\Delta_N(E_N), \Delta_\pi(E_\pi)$  and  $\Delta_p(E_p)$  are series of the LIV correction coefficients defined in Eq.(2.7) separately for nucleon, pion and proton. The left sides of Eq.(2.11) and Eq.(2.12) are invariant under the Lorentz transformation. Thus, in reference frame where  $|\vec{p}_N^*| = |\vec{p}_\pi^*|$  we can write [17]

$$(E_N^*)^2 - (p_N^*)^2 = \Delta_N(E_N) + m_N^2, \quad (2.14)$$

$$(E_\pi^*)^2 - (p_\pi^*)^2 = \Delta_\pi(E_\pi) + m_\pi^2, \quad (2.15)$$

where  $E_N^*, E_\pi^*$  are energies and  $\vec{p}_N^*, \vec{p}_\pi^*$  are momenta of the nucleon  $N$  and pion  $\pi$  in reference frame where  $|\vec{p}_N^*| = |\vec{p}_\pi^*|$ . By subtracting Eq.(2.15) from Eq.(2.14) we obtain the following relation [17]

$$(E_N^*)^2 - (E_\pi^*)^2 = s_N(E_N) - s_\pi(E_\pi), \quad (2.16)$$

where we used the notation from Eqs.(2.11) and (2.12). Next we define  $s$  as [17]

$$s = E_{tot}^2 - p_{tot}^2, \quad (2.17)$$

where  $E_{tot}$  is total energy of a system and  $\vec{p}_{tot}$  is total momentum of a system in arbitrary reference frame. For the interacting proton-photon from Eq.(2.10), the  $s$  in frame where proton momentum is null, i.e. where  $E_p' = \sqrt{s_p(E_p)}$  with  $s_p(E_p)$  defined in Eq.(2.13), is given by [17]

$$s = 2\sqrt{s_p(E_p)}\epsilon + s_p(E_p), \quad (2.18)$$

---

<sup>4</sup> The constant  $c$  is set to 1 in all the calculations in this section.

where  $\epsilon$  is the CMB photon energy in the frame where proton momentum is null. On the other hand, in the frame where  $|\vec{p}_N^*| = |\vec{p}_\pi^*|$  the  $s$  is given by [17]

$$s = (E_N^* + E_\pi^*)^2. \quad (2.19)$$

By expressing  $E_\pi^*$  from Eq.(2.16) and substituting it to the Eq.(2.19) we obtain [17]

$$(E_N^*)^2 - (\sqrt{s} - (E_N^*))^2 = s_N(E_N) - s_\pi(E_\pi), \quad (2.20)$$

$$2\sqrt{s}E_N^* = s + s_N(E_N) - s_\pi(E_\pi), \quad (2.21)$$

$$E_N^* = \frac{1}{2\sqrt{s}}(s + s_N(E_N) - s_\pi(E_\pi)). \quad (2.22)$$

Lorentz transformation from one observer to another is not effected by LIV [50]. Thus, the transformation for the nucleon energy from the frame where  $|\vec{p}_N^*| = |\vec{p}_\pi^*|$  to LAB frame is given by [17]

$$E_N = \gamma(E_N^* + \beta |p_N^*| \cos(\theta)). \quad (2.23)$$

By substituting the nucleon momentum expressed from Eq.(2.14) as  $|p_N^*| = \sqrt{E_N^{*2} - s_N(E_N)}$  in Eq.(2.23) and by  $\beta \rightarrow 1$  for extremely high energies, one have [17]

$$E_N = \gamma(E_N^* + \sqrt{(E_N^*)^2 - s_N(E_N)} \cos(\theta)). \quad (2.24)$$

where  $\theta$  is the angle between the proton and photon momenta. The Lorentz factor connecting frame where  $|\vec{p}_N^*| = |\vec{p}_\pi^*|$  with the LAB frame is given by [17]

$$\gamma = \frac{E_p}{\sqrt{s}}, \quad (2.25)$$

where the energy of a photon was neglected since in LAB  $E_p \gg E_{\text{CMB}}$  ( $E_{\text{CMB}}$  is the energy of the CMB photon) and  $s$  is given by Eq.(2.18). By defining inelasticity as  $K_\theta = 1 - E_N/E_p$  we can express nucleon and pion LAB energies as  $E_N = (1 - K_\theta)E_p$  and  $E_\pi = K_\theta E_p$  [17]. Thus, the  $s_N(E_N)$  and  $s_\pi(E_\pi)$  from Eqs.(2.11, 2.12) can be rewritten as a function of inelasticity and the incoming proton energy in LAB frame as follows [17]

$$s_N(E_N) = s_N((1 - K_\theta)E_p), \quad (2.26)$$

$$s_\pi(E_\pi) = s_\pi(K_\theta E_p). \quad (2.27)$$

Thus, all the components necessary to build up an equation where only inelasticity, incoming proton energy measured in LAB frame, photon energy in frame where proton momentum is null and masses for proton, pion and nucleon appears, are ready. Putting expression  $E_N = (1 - K_\theta)E_p$ , the Lorentz factor from

Eq.(2.25) and the expression for  $E_N^*$  from Eq.(2.22) to Eq.(2.24), we finally obtain following transcendental equation for the inelasticity  $K_\theta$  [17]

$$(1 - K_\theta)E_p = \frac{E_p}{\sqrt{s}} \left( \frac{1}{2\sqrt{s}}(s + s_N - s_\pi) + \sqrt{\frac{1}{2\sqrt{s}}(s + s_N - s_\pi) - s_N \cos(\theta)} \right). \quad (2.28)$$

After rearrangement of the terms, canceling out  $E_p$  we get [17]

$$0 = (1 - K_\theta)\sqrt{s} - \left( \frac{1}{2\sqrt{s}}(s + s_N - s_\pi) + \sqrt{\frac{1}{2\sqrt{s}}(s + s_N - s_\pi) - s_N \cos(\theta)} \right). \quad (2.29)$$

In the Appendix B fully expanded form of the this equation can be found (Eq.B.1). To obtain the total inelasticity an average of  $K_\theta$  is made [17]

$$K = \frac{1}{\pi} \int_0^\pi K_\theta d\theta. \quad (2.30)$$

## 2.3 Proton CR propagation modified by LIV

According to Ref.[38] the LIV correction for pion has to be bigger than the proton (or nucleon) correction if one do not want to suppress the photomeson production entirely.<sup>5</sup> Entire suppression of the photomeson production would caused a disappearance of the observed GZK steepening from the CR spectrum. To be still consistent with the fact that the GZK steeping is present in the measured spectra we took  $\Delta_p = 0$  and  $\Delta_N = 0$ . Thus, only LIV pion corrections  $\Delta_\pi$  are investigated. In number of papers, 2<sup>nd</sup> order of pion LIV corrections were already studied, for instance Refs.[21, 49]. Here, we also studied the effect of 3<sup>rd</sup> and 4<sup>th</sup> order corrections. For each examined order, four different values of the LIV coefficient  $\eta_n$  were chosen.

To obtain the modified total inelasticity, a bunch of  $K_\theta s$  in the range  $0 - \pi$  have to be calculated in order that the integral Eq.(2.30) can be numerically computed. To solve the transcendental equation for  $K_\theta$ , we coded a custom solver. Total inelasticity  $K$  was subsequently numerically calculated in energy range  $10^{19.5} - 10^{22}$  eV for protons (in the LAB frame) and in energy range  $0.2 - 4$  GeV for photons (in the proton rest frame<sup>6</sup>). This was done for three different orders of LIV, 2<sup>nd</sup>, 3<sup>rd</sup> and 4<sup>th</sup>. The results are shown in Fig.2.1.

The LIV coefficients are causing a suppression of the inelasticity (compare Fig.(1.6) with Fig.(2.1). The place between the suppressed and unsuppressed inelasticity on Fig.2.1 we are calling “the border”. The magnitude of the  $\eta_n$  gives the position of the border. The bigger, the  $\eta_n$ , the more is the border shifted towards lower proton energies, and earlier is the interaction suppressed (compare panels in arbitrary column in Fig.2.1). Choice of a different LIV order manifests

<sup>5</sup> For more details see Refs.[21, 38, 35].

<sup>6</sup> Proton rest frame - reference frame where proton momentum is null.

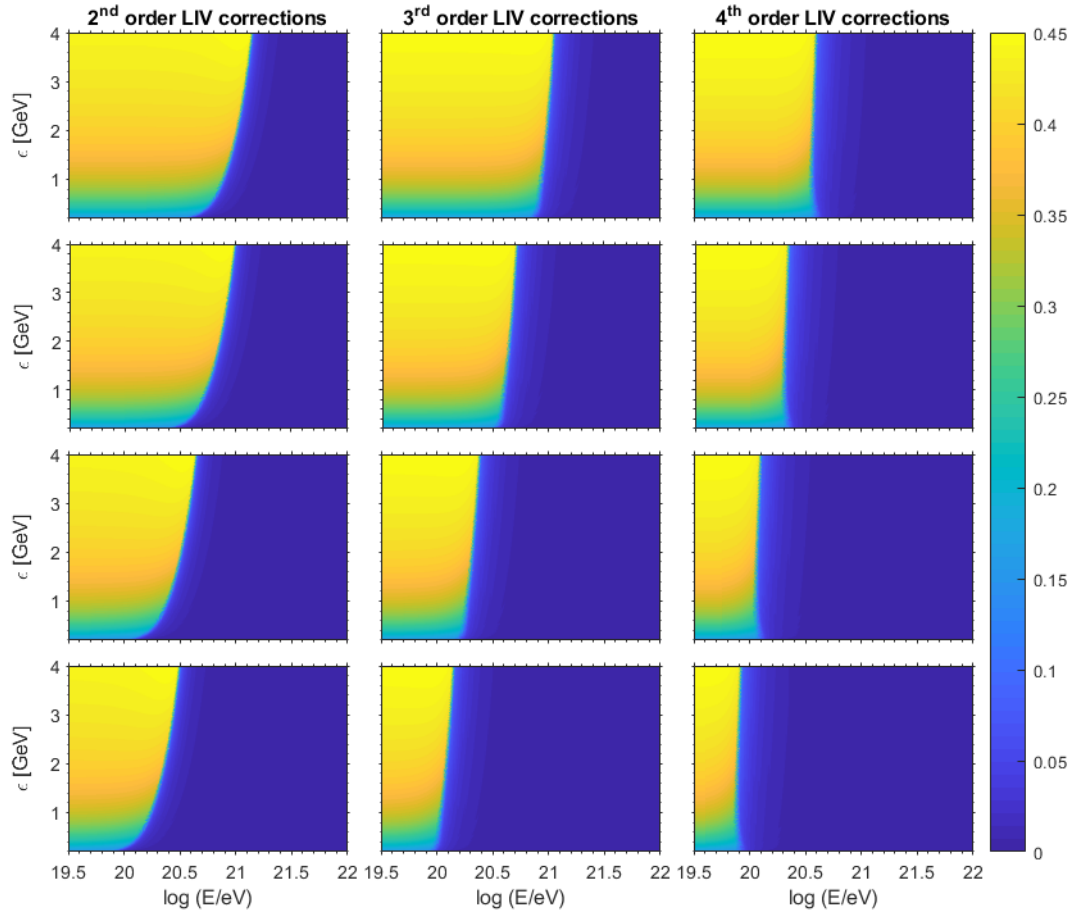


Figure 2.1: Inelasticity (color scale) as a function of proton energy measured in LAB frame (x-axis) and photon energy measured in proton rest frame (y-axis) for various orders and values of  $\eta_i$ . Each column represents a different order of LIV corrections. The used values of  $\eta_2$ , starting from the top plot are:  $5 \times 10^{-5}$ ,  $\times 10^{-4}$ ,  $5 \times 10^{-4}$  and  $\times 10^{-3}$ . For the middle column, the values of  $\eta_3$  are  $5 \times 10^{-14}$ ,  $10^{-14}$ ,  $10^{-15}$ , and  $10^{-16}$ . For the last column, the values of  $\eta_4$  are  $5 \times 10^{-5}$ ,  $10^{-5}$ ,  $10^{-6}$  and  $10^{-7}$ .

in shape of the border. Going to higher orders the shape of the border at small photon energies is starting to curve to opposite side (compare panels in arbitrary row in Fig.2.1).

The modified attenuation lengths were calculated using Eq.(1.12) with the inelasticity modified by LIV coefficients given in caption to Fig.(2.1). The calculated attenuation lengths for  $2^{nd}$  LIV order are shown in Fig.2.2. At first, the behavior of the attenuation lengths is the same as for no-LIV case. After reaching the energies around the border (compare with Fig.2.1), the attenuation lengths start to increase again. As can be seen, the larger the LIV coefficient  $\eta_n$  is, the earlier the recovery starts. Attenuation lengths computed with LIV corrections of  $3^{rd}$  and  $4^{th}$  order can be found in Figs.A.1 and A.2 in Appendix A. Despite the different shape of the borders in Fig.2.1 of different LIV orders, the behavior of attenuation lengths for  $3^{rd}$  and  $4^{th}$  order was very similar as in the case of  $2^{nd}$  order. Slight difference can be observed only at the beginning of the recovery what is a consequence of different shape of the border in lower photon energies observed in Fig.2.1.

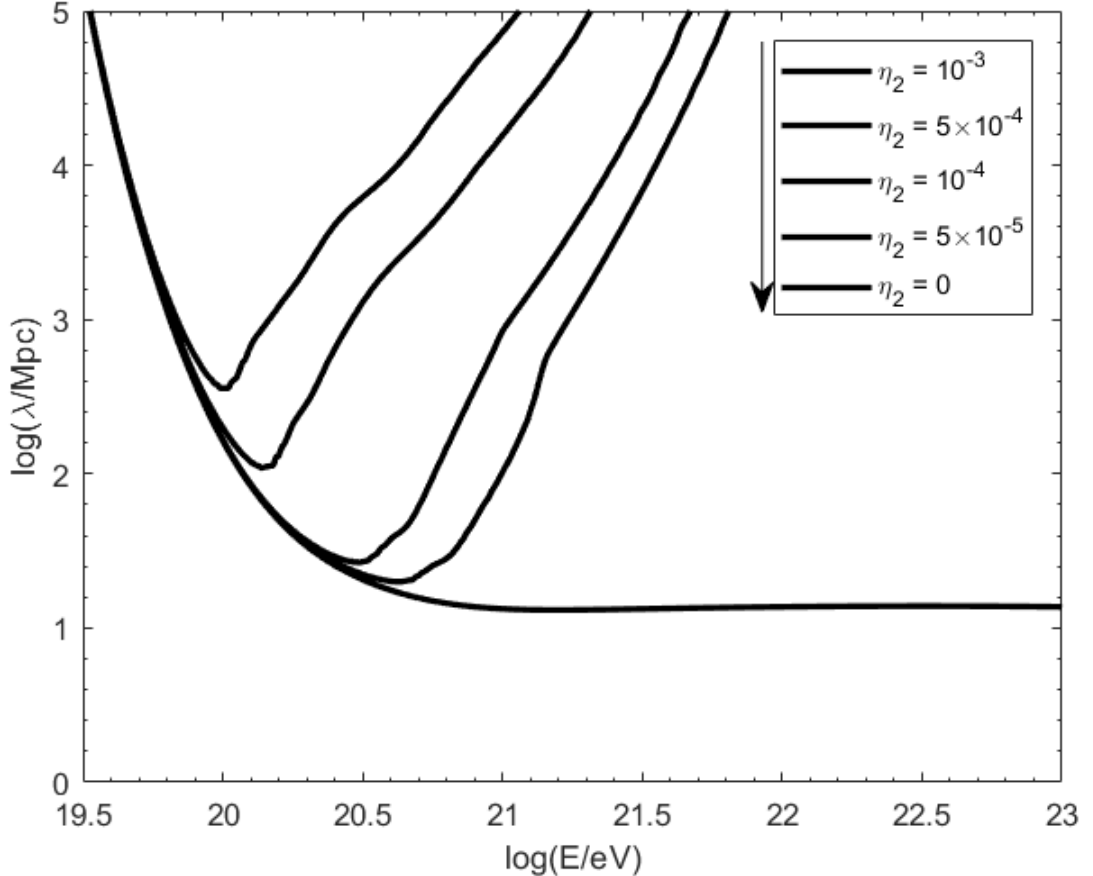


Figure 2.2: Proton attenuation length as a function of proton energy affected by  $2^{nd}$  order LIV coefficients. Values of the LIV coefficients are written in the top right corner.

Modification of the photomeson production also causes different total energy losses. The modified energy losses were calculated using the values of  $\eta_n$  given in caption to Fig.2.1. The results are shown on Fig.2.3. After the suppression of photomeson production the energy losses caused by cosmic expansion start to dominate again. However, if the proton-photon interaction is suppressed very early (large values of  $\eta_n$ ), for a short period the dominant mechanism of energy loss is pair production (panels in third and fourth rows in Fig.2.3).

Finally, the modified proton energy evolutions were computed using Eqs.(1.17), (1.18) and (1.19). In Fig.2.4 the effect of the  $2^{nd}$  order LIV coefficients on the proton energy evolution, for small redshifts, is shown. The LIV bound the photomeson production epoch from the upper side. The sooner is the photomeson production suppressed, the sooner proton stops rapidly losing its energy. This causes large extension of the effective horizon, and therefore proton can come from more distant sources. In the Appendix B, in Fig.B.1 proton energy evolution functions calculated for  $\eta_n$  coefficients given in caption to Fig.2.1 as a function of redshift in range  $z \in <0, 5>$  are summarized.

To determine values of the proton's effective horizon modified by LIV, the same method as in chapter one was used. We computed the proton energy evolutions and redshift where proton reached energy equal to gave us the value of

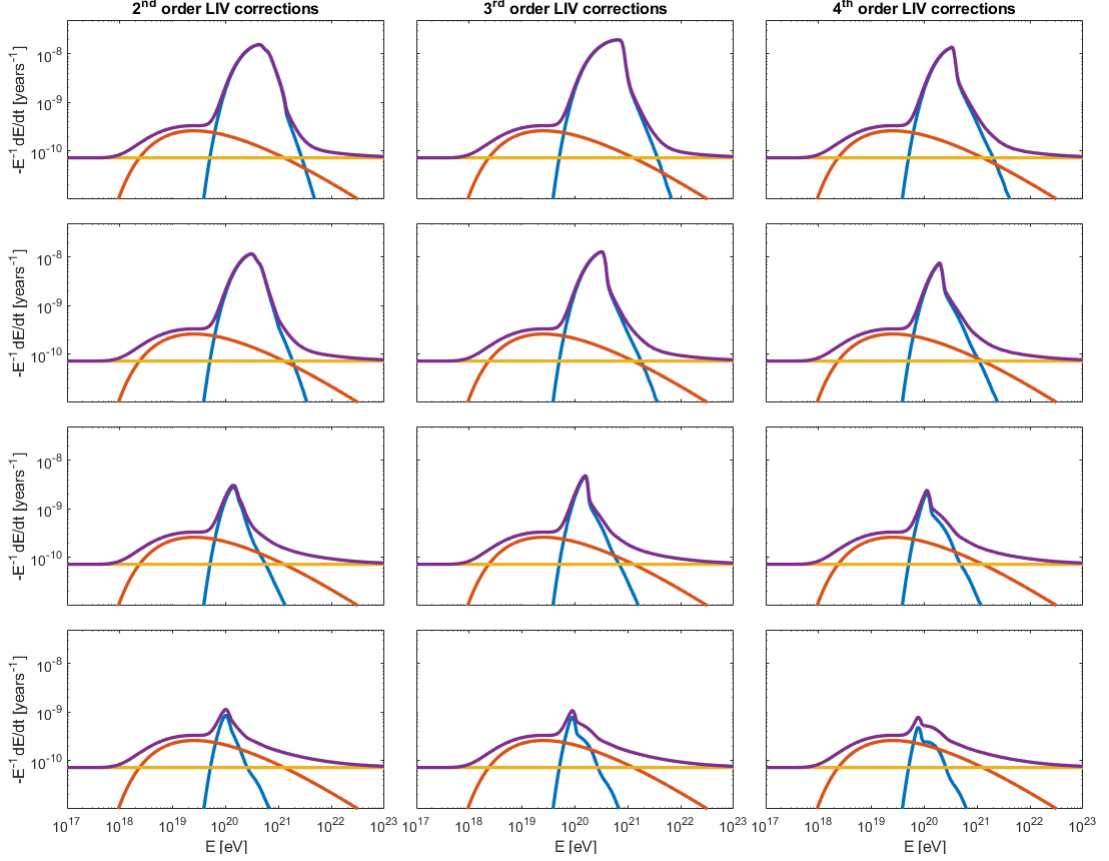


Figure 2.3: Modified proton energy losses as a function of proton energy calculated for the following orders and values of  $\eta_n$ . In the first column, from top to bottom, the values of  $\eta_2$  are:  $5 \times 10^{-5}$ ,  $\times 10^{-4}$ ,  $5 \times 10^{-4}$  and  $\times 10^{-3}$ . In the middle column, the values of  $\eta_3$  are:  $5 \times 10^{-14}$ ,  $10^{-14}$ ,  $10^{-15}$ , and  $10^{-16}$ . In the last column, the values of  $\eta_4$  are:  $5 \times 10^{-5}$ ,  $10^{-5}$ ,  $10^{-6}$  and  $10^{-7}$ . The orange lines represent losses by cosmic expansion, red lines for pair production losses, blue lines indicate photomeson losses and violet lines are the sum of all the mentioned losses. Compare also with Fig.1.9.

the effective horizon  $E_{max}^{source}$ .<sup>7</sup> The effective horizon as a function of 2<sup>nd</sup> order LIV coefficients, for different  $E_{max}^{source}$  scenarios is shown in Fig.2.5. The character of the horizon growth strongly dependent on the chosen  $E_{max}^{source}$  scenario. Generally, with the higher values of  $E_{max}^{source}$ , the horizon increase more rapidly with increasing  $\eta_2$ . For instance, the lowest scenario  $E_{max}^{source} = 10^{20.5}$  eV, the horizon only slightly grow with increasing  $\eta_2$ . The horizon rises only from tens of Mpc to hundreds Mpc in the range  $\eta_2 \in < 0, 10^{-3} >$  for the proton energy  $E \geq 10^{20}$  eV. On the other hand, for scenarios  $E_{max}^{source} \geq 10^{22}$  eV, the horizon immediately jump to thousands of Mpc and further does not significantly grow anymore. For the most extreme calculated scenario  $E_{max}^{source} = 10^{23}$  eV this yields  $\sim 9000$  Mpc what corresponds to a redshift about  $z \approx 20$ , the assumed epoch of the first stars birth. Therefore, this would mean that the most energetic proton observed at Earth could originate even from the first born stars.

The effects of different LIV orders on energy evolution were also investigated. For this, particular values of 2<sup>nd</sup>, 3<sup>rd</sup> and 4<sup>th</sup> were chosen such that the border

<sup>7</sup>  $E_{max}^{source}$  - maximal energy to which the proton can be accelerated at the source.

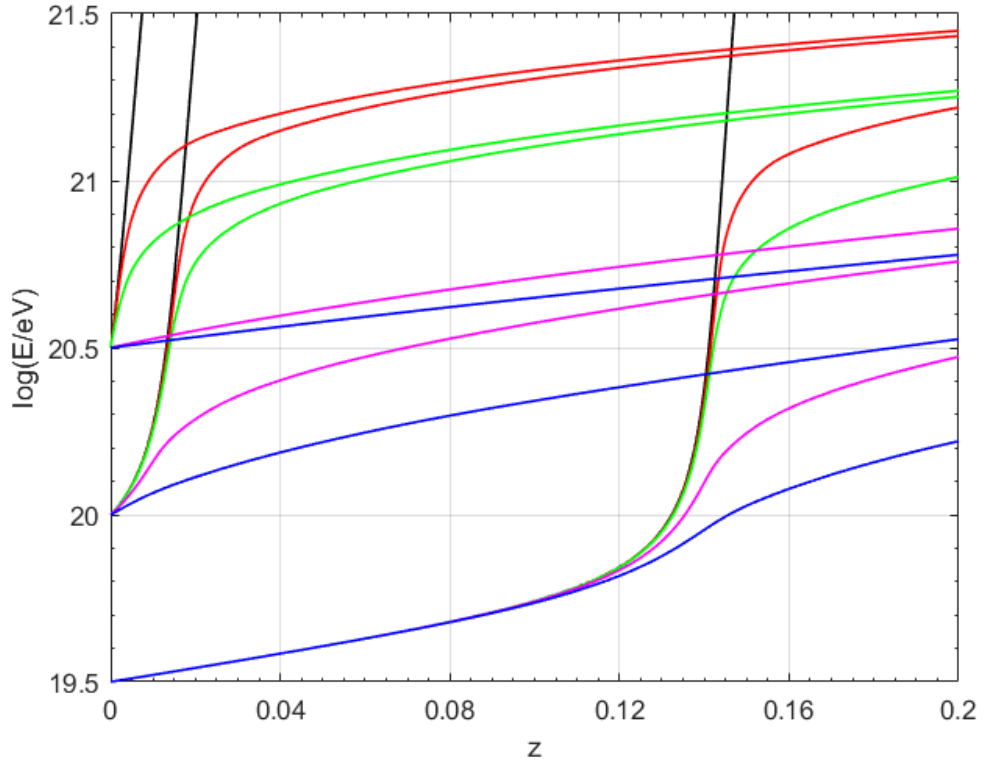


Figure 2.4: Proton energy evolution as a function of redshift. Proton energy evolutions for No-LIV,  $\eta_2 = 5 \times 10^{-5}$ ,  $\eta_2 = 10^{-4}$ ,  $\eta_2 = 5 \times 10^{-4}$  and  $\eta_2 = 10^{-3}$  are shown by black, red, green, magenta and blue lines respectively.

of the suppression in inelasticities was nearly on the same place (top panels in Fig.2.7). Total energy losses for examined cases shown in Fig.2.6 are the same, except for the slightly different decline after the peak. To see if this difference has a significant effect on proton propagation, energy evolution using the same coefficients as in Fig.2.6 were computed. The result is shown in bottom panels in Fig.2.7. The computed curves do not show any observable differences. Also, in Fig.B.1 it can be seen that the only difference between the panels is produced by the epoch when the photomeson production was turned off. To summarize, different orders of LIV corrections manifests in the same way. The only significant change is produced by the different magnitude of the coefficient  $\eta_n$ .

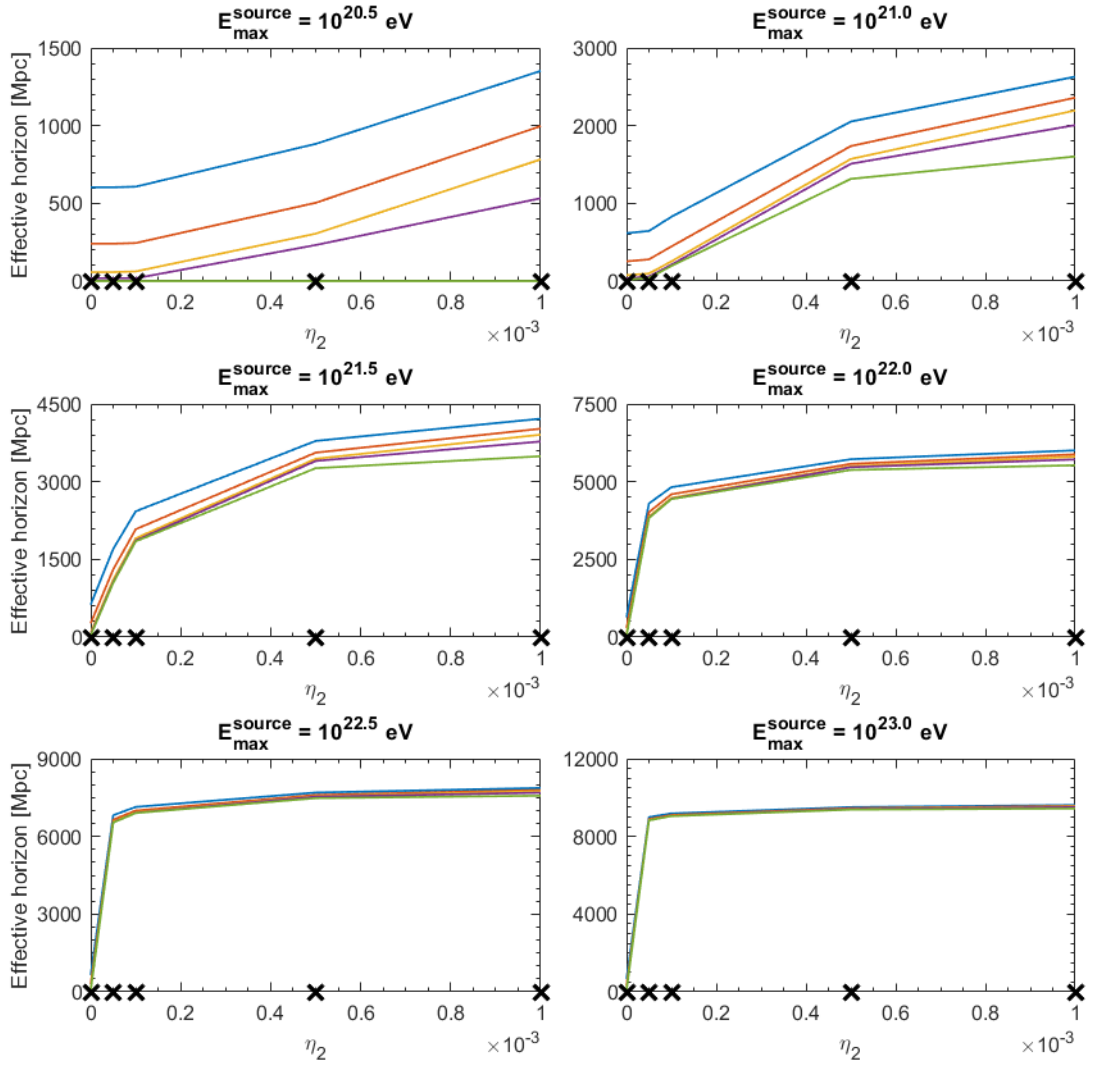


Figure 2.5: Proton's effective horizon as a function of  $2^{nd}$  order LIV coefficients. Cases for protons that were measured on Earth with energies  $10^{19.5}$  eV,  $10^{19.75}$  eV,  $10^{20}$  eV,  $10^{20.25}$  eV and  $10^{20.5}$  eV are depicted by blue, red, yellow, violet and green lines. The black cross marks on x-axis are the examined values of  $\eta_2$ . Panels represents different scenarios of proton maximal energy at sources.

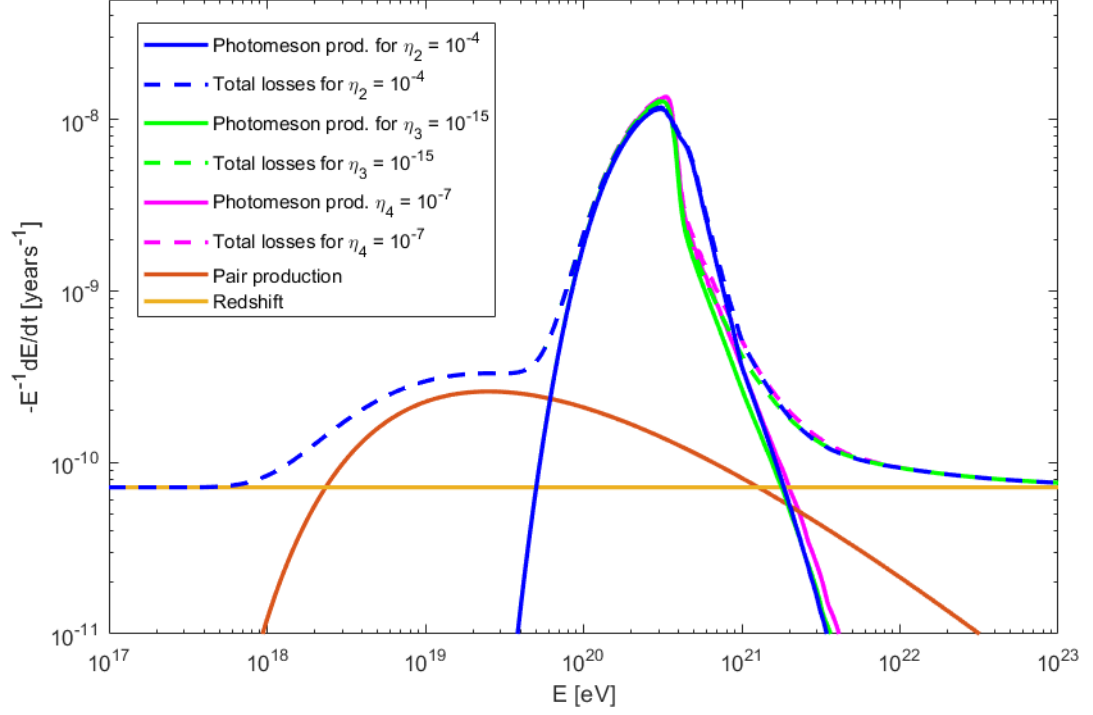


Figure 2.6: Comparison of proton total energy losses as a function of energy for  $\eta_2 = 10^{-4}$ ,  $\eta_3 = 10^{-15}$  and  $\eta_4 = 10^{-7}$ .

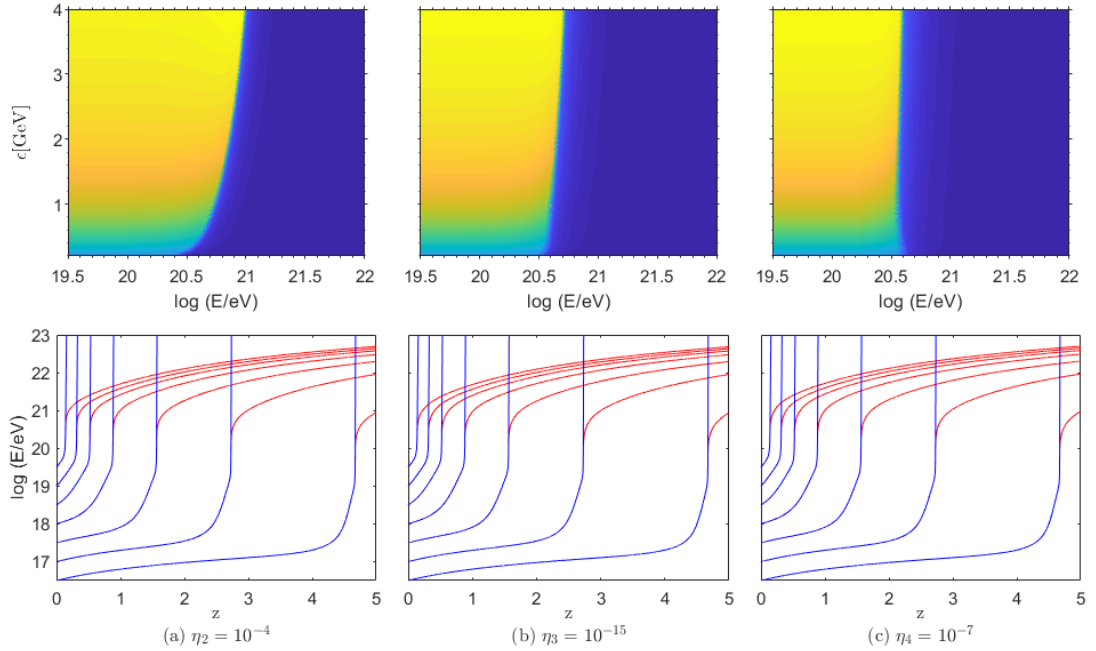


Figure 2.7: Upper panels: inelasticity (color scale) as a function of proton energy measured in LAB frame (x-axis) and photon energy measured in proton rest frame (y-axis) for  $\eta_2 = 10^{-4}$ ,  $\eta_3 = 10^{-15}$  and  $\eta_4 = 10^{-7}$  (from left to right). Bottom panels: proton energy evolution as a function of proton energy in the bottom panels for  $\eta_2 = 10^{-4}$ ,  $\eta_3 = 10^{-15}$  and  $\eta_4 = 10^{-7}$  (from left to right). The resulting curves are of the energy evolution functions are indistinguishable.

# 3. Proton CR spectrum modified by LIV effects

In this chapter, a derivation of the analytical formula for a model of CR spectrum is presented. Moreover, the influence of the model's free parameters spectral index  $\Gamma$ , source evolution term  $\zeta$  and proton maximal energy at sources  $E_{max}^{source}$  on the model of CR spectrum is discussed. Finally, the spectrum affected by LIV is studied. Since currently no astrophysical simulation software dedicated for the study of UHECR propagation contain LIV module, an analytical formalism for proton spectrum derived by Berezhinsky and Grigorieva[1] was used. The formalism has already been used to study LIV effects on proton spectra in several other papers, for instance in Refs.[17, 21].

## 3.1 Analytical calculation of the proton CR spectrum

The derivations of the formula for the diffuse flux starts from the conservation of number of protons within the energy interval  $< E, E + dE >$  which has to be conserved in the comoving volume (the protons can not disappear). We assume roughly straight line propagation from sources to the observer unaffected by magnetic fields. Hence, [51]

$$n_p(E)dE = \int_{t_{min}}^{t_0} dt Q_{gen}(E_g, t)dE_g, \quad (3.1)$$

where  $n_p(E)$  is the density of protons with energy  $E$ ,  $t_0$  is the current age of the universe,  $t_{min}$  is time-age of the universe at emission of the proton,  $E_g$  is the generation energy defined as the energy of a proton generated by the source at time  $t$  and measured with an energy  $E$  on Earth. The  $Q_{gen}$  stands for the generation rate per unit comoving volume, i.e., particles produced by sources at time  $t$  with an initial energy  $E_g$ . Using the time-redshift relation  $|dt/dz| = H^{-1}(z)/(1+z)$  from Eq.1.16, the Eq.3.1 can be rewritten as [51]

$$n_p(E)dE = \int_0^{z_{max}} dz \frac{1}{H(z)(1+z)} Q_{gen}(E_g, z)dE_g. \quad (3.2)$$

Further, the  $Q_{gen}$  can be expressed through volume emissivity  $\mathcal{L}(z)$  of the sources (the energy released per unit redshift and unit of comoving volume), with a conveniently used power-law energy dependence of the form  $E^{-\Gamma}$  where the parameter  $\Gamma$  is the spectral index. Hence, [51]

$$Q(E_g, z) = \mathcal{L}(z)E_g^{-\Gamma}. \quad (3.3)$$

Possible evolution of sources is expressed through relation  $\mathcal{L}(z) = \mathcal{L}(0)(1+z)^\zeta$ ,

where  $\zeta$  is the source evolution term (i.e. parameter for the evolution of the sources). Putting Eq.(3.3) to Eq.(3.2) gives [51]

$$n_p(E)dE = \int_0^{z_{max}} dz \frac{1}{H(z)(1+z)} \mathcal{L}(0)(1+z)^\zeta E_g^{-\Gamma} dE_g. \quad (3.4)$$

After small rearrangements, multiplying the Eq.(3.4) by  $c/4\pi$  and using the expression  $H(z) = H_0\sqrt{\Omega_m(1+z)^3 + \Omega_\Lambda}$ , we obtained the final formula for the spectrum [51]

$$J(E) = \frac{c\mathcal{L}(0)}{4\pi H_0} \int_0^{z_{max}} dz \frac{(1+z)^{\zeta-1}}{\sqrt{\Omega_m(1+z)^3 + \Omega_\Lambda}} E_g^{-\Gamma} \frac{dE_g}{dE}. \quad (3.5)$$

To calculate the spectrum using Eq.(3.5), one has to know the generation energy  $E_g(E, z)$ . The function  $E_g(E, z)$  can be easily obtained from the calculated energy evolution functions discussed in Chapter 1.. In Fig.1.10, the curves are representing the evolution of the proton energy through the redshifts of the proton that was observed on Earth (redshift  $z = 0$ ) with energy  $E$ . By taking values from all the curves at some particular redshift  $z$  and plotting them against their Earth-observed energy (redshift  $z = 0$ ) one obtain function  $E_g(E, z)$  for some particular redshift  $z$ . Example of such computed functions is shown in Fig.3.1. Each curve represents generation energy  $E_g(E, z)$  in the redshift range 0.001 – 0.2 with step of 0.005. For the calculations of the spectrum model, we calculated generation energy functions  $E_g(E, z)$  with redshift step 0.0001.

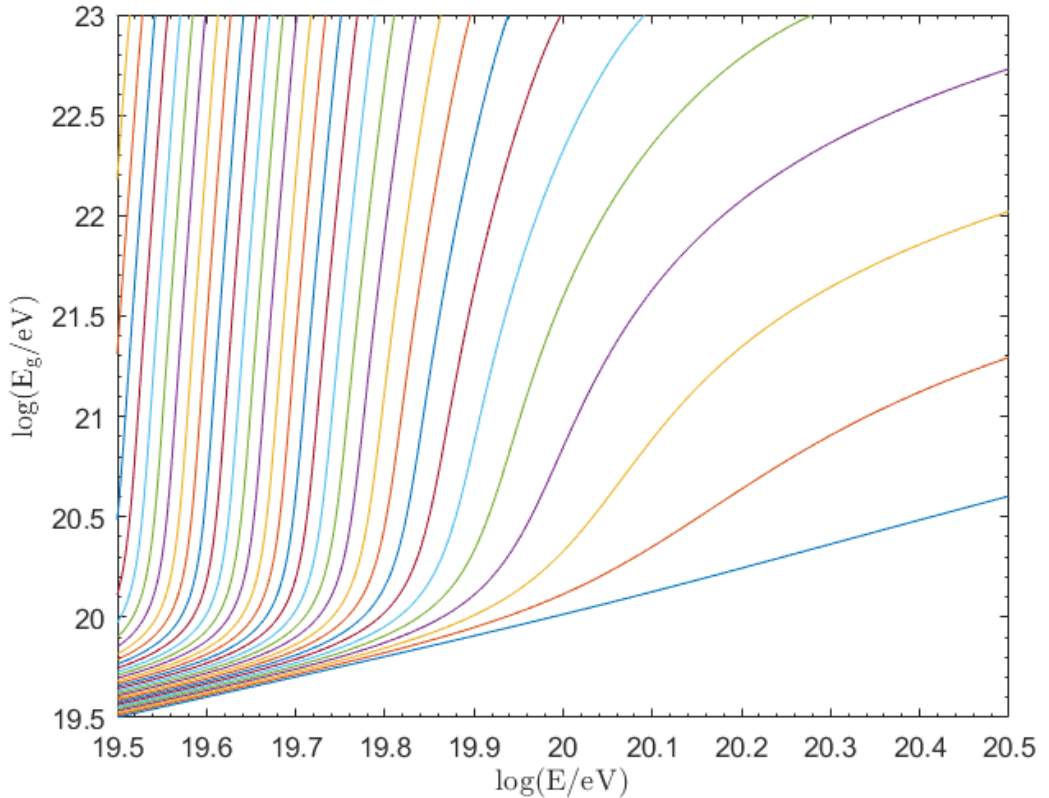


Figure 3.1: Generation energy  $E_g(E, z)$  as a function of proton energy calculated for redshifts  $z$  in range 0.001 – 0.2 with step of 0.005 (from right to left).

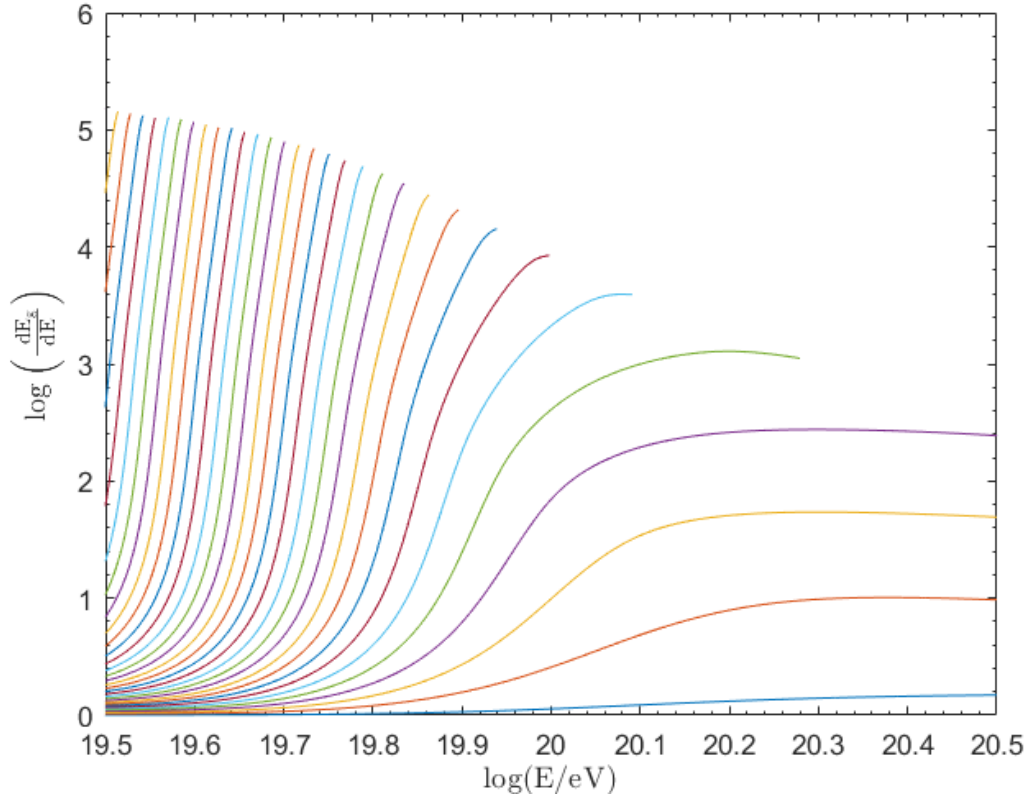


Figure 3.2: The derivative  $dE_g(E, z)/dE$  of the generation energy  $E_g(E, z)$  as a function of proton energy calculated for redshifts  $z$  in range  $0.001 - 0.2$  with step of  $0.005$  (from right to left). The cut-off is caused by the maximal energy at sources  $E_{max}^{source} = 10^{23}$  eV (compare with Fig.3.1).

Next necessary quantity is the derivative  $dE_g(E, z)/dE$  of the generation energy  $E_g(E, z)$  also known as the dilatation of the energy interval. The derivative  $dE_g(E, z)/dE$  can be understood as a connection between energy intervals at epochs of production and observation. According to Berezhinsky [1] the derivative  $dE_g(E, z)/dE$  is calculated by using the following formula

$$\frac{dE_g(E, z)}{dE} = (1 + z) \exp \left( \frac{1}{H_0} \int_0^z dz' (1 + z')^{1/2} \left( \frac{db_0(E')}{dE'} \right)_{E'=(1+z')E_g(z')} \right). \quad (3.6)$$

Where  $b_0$  represents the energy losses of the proton at  $z = 0$ . The detailed calculation of the derivative  $db_0(E)/dE$  can be found in Ref.[51]. To avoid the tremendous numerical integrations we worked out an alternative approach from which we were able to obtain the same models of spectra as in Refs.[12, 17, 51].

Since we already numerically calculated  $E_g(E, z)$  as function of  $E$  (for different  $z$ ), we interpolated the curves with cubic spline and subsequently derivated the splined function with respect to  $E(z = 0)$ . The results are shown in Fig.3.2 for the same redshifts as in Fig.3.1.

The final step in the spectrum calculation is the numerical integration of Eq.(3.5) from 0 up to some  $z_{max}$  from where sources are not relevant anymore for the phenomena since they lie beyond the horizon. The  $z_{max}$ , therefore, vary with proton's observed energy on Earth.

The formula for the spectrum given by Eq.(3.5) contains several free parameters, the emissivity of the sources  $\mathcal{L}_0$ , the source evolution term  $\zeta$  and the spectral index  $\Gamma$ . However, implicitly the formula for the spectrum also depends on the maximal proton energy at sources  $E_{max}^{source}$ . In the calculations we allowed energy rescaling  $\pm 15\%$ . Since the emissivity  $\mathcal{L}_0$  acts only as the normalization constant shifting the spectrum up or down, its influence on the spectrum is not investigated further. The influence of the three free parameters  $\Gamma$ ,  $\zeta$  and  $E_{max}^{source}$  on the shape of the CR spectrum model is shown in Figs.3.3, 3.4 and 3.5. In each of these figures we vary only one parameter while the others remained the same. The data with error bars represent the combined spectrum measured by Pierre Auger Observatory [52]. The cross marks with arrows represent the upper limits on the CR flux derived using the Surface Detector of the Pierre Auger Observatory [52].

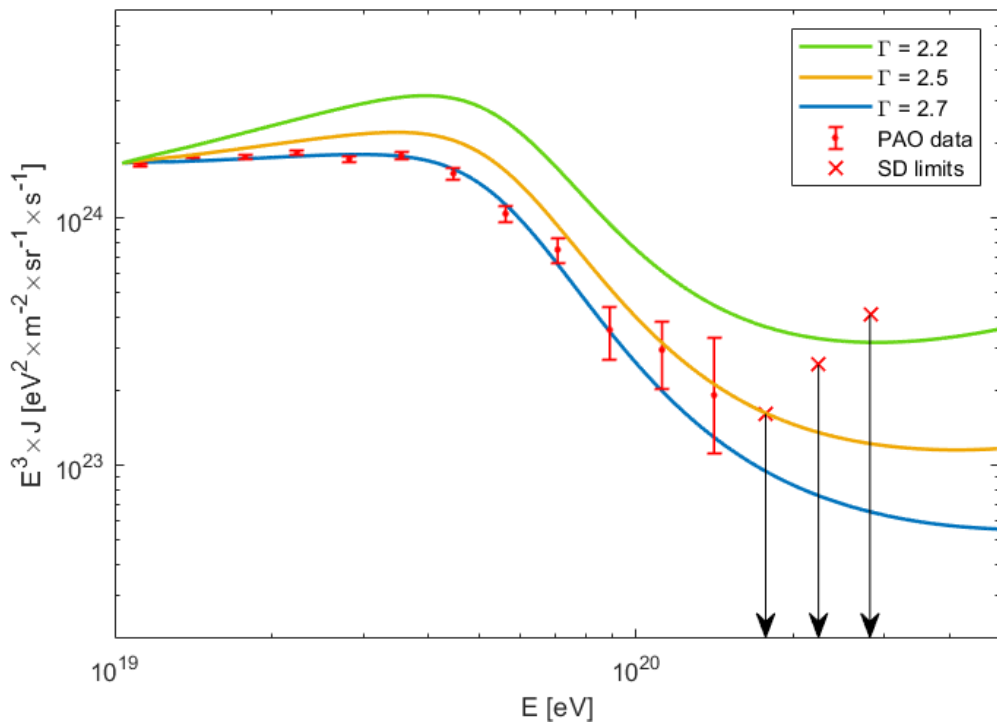


Figure 3.3: Models of proton CR spectra multiplied by  $E^3$  for different values of spectral index  $\Gamma$ , with fixed source evolution term  $\zeta = 6$  and fixed proton maximal energy at sources  $E_{max}^{source} = 10^{22.5}$  eV. The data with error bars represent the combined spectrum measured by Pierre Auger Observatory [52]. The cross marks with arrows represents the upper limits on the CR flux derived using the Surface Detector of the Pierre Auger Observatory [52].

The spectrum is very sensitive to a change of the spectral index  $\Gamma$ . Change of its value changes the slope of the spectrum, see Fig.3.3. The larger the spectral index  $\Gamma$ , the steeper, the slope is. The influence of the source evolution parameter  $\zeta$  is weak, its increase from 0 to 6 produces only a slight change at the end of the spectrum. The parameter  $E_{max}^{source}$  is responsible for the beginning of the suppression. With growing  $E_{max}^{source}$  the suppression is shifted to higher energies. In Fig.3.5 difference between curves with  $E_{max}^{source} = 10^{21.5}$  eV and  $E_{max}^{source} = 10^{22.5}$  eV is almost unnoticeable since the x-axis ends at energy  $5 \times 10^{20.5}$  eV. The difference is expected to be seen at higher energy.

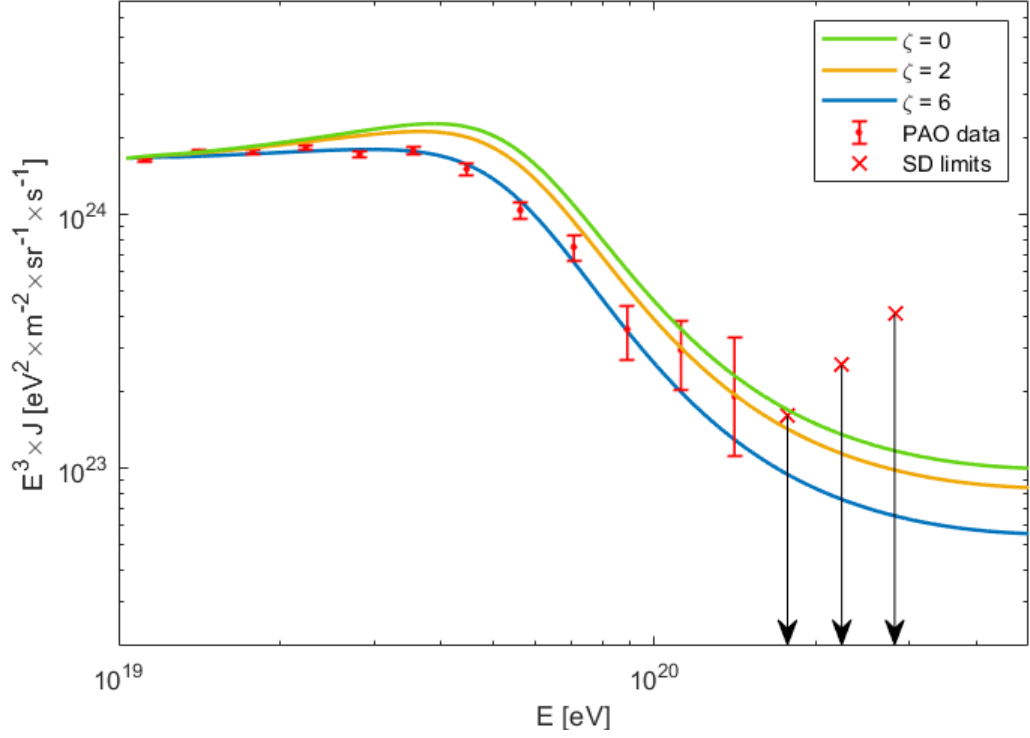


Figure 3.4: Models of proton CR spectra multiplied by  $E^3$  for different values of the source evolution term  $\zeta$ , with fixed spectral index  $\Gamma = 2.7$  and fixed proton maximal energy at sources  $E_{max}^{source} = 10^{22.5}$  eV. For more details see caption to Fig.3.3.

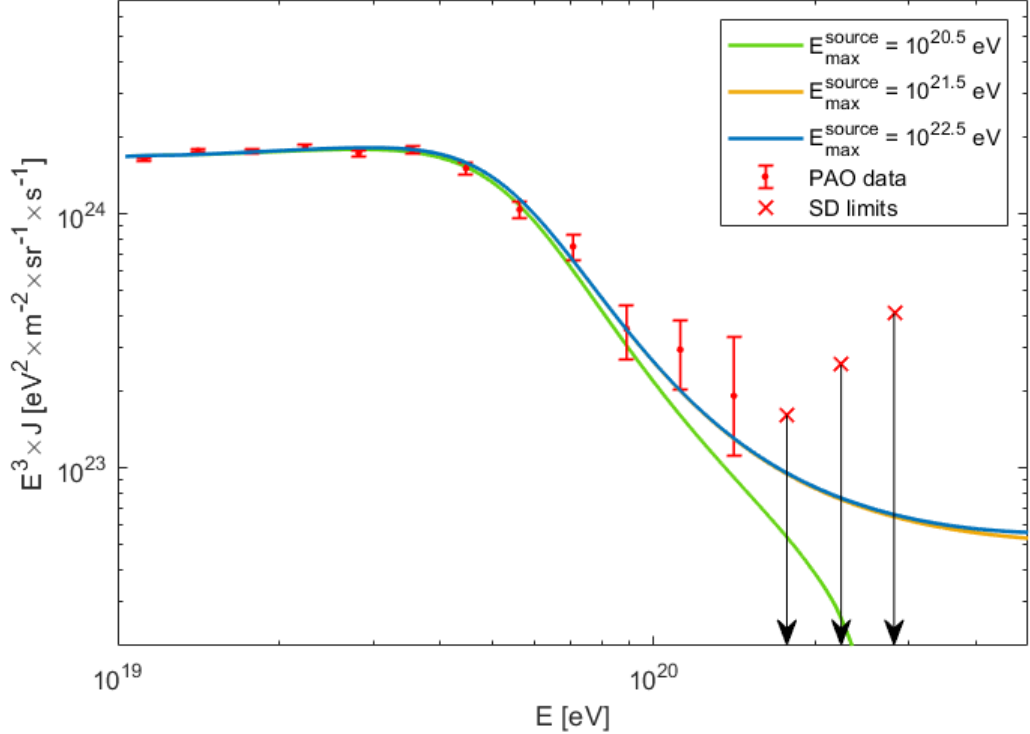


Figure 3.5: Models of proton CR spectra multiplied by  $E^3$  for different values of proton maximal energy at sources  $E_{max}^{source}$ , with fixed spectral index  $\Gamma = 2.7$  and fixed source evolution term  $\zeta = 6$ . For more details see caption to Fig.3.3.

## 3.2 Proton CR spectra modified by LIV

The presented analytical formalism was used to study the LIV effects on the proton spectrum. The investigated corrections were of the 2<sup>nd</sup> order with the following values  $\eta_2 = 10^{-3}, 5 \times 10^{-4}, 10^{-4}$  and  $5 \times 10^{-5}$ . The model spectra modified by LIV coefficients  $\eta_2$ , for two different sets of fixed parameters  $\Gamma$ ,  $\zeta$  and  $E_{max}^{source}$ , are shown in Figs.3.6 and 3.7. Immediately, it is evident that the LIV causes a recovery of the end of the spectral curves. In Fig.3.6 is shown that with the increasing value of  $\eta_2$  the recovery starts at lower energies. However, the character of the recovery can differ under the different combination of the remaining free parameters. In contrast to Fig.3.6 in Fig.3.7 is shown that the spectra with no LIV,  $\eta_2 = 5 \times 10^{-5}$  and  $\eta_2 = 10^{-4}$  are indistinguishable. The recovery of the spectra for  $\eta_2 = 10^{-3}$  and  $\eta_2 = 5 \times 10^{-4}$  in Fig.3.7 is suppressed. On the other hand, in Fig.3.6 spectra for these LIV coefficients are rapidly rising. Thus, the character of the LIV effect on the spectra also depends on the choice of the remaining free parameters.

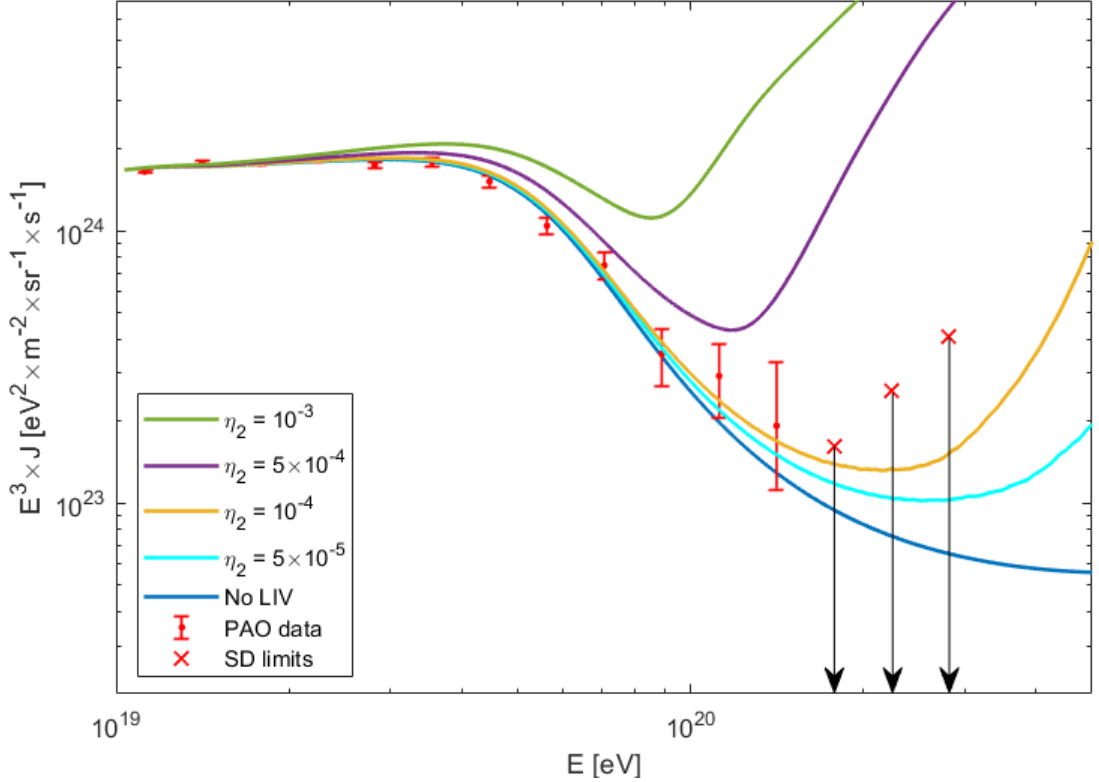


Figure 3.6: Models of CR spectra multiplied by  $E^3$  with spectral index  $\Gamma = 2.7$ , source evolution term  $\zeta = 6$  and proton maximal energy at source  $E_{max}^{source} = 10^{22.5}$  eV affected by LIV coefficients in legend. For more details see caption to Fig.3.3.

In order to investigate the compatibility of spectra modified by LIV with measured data of combined spectra from Pierre Auger Observatory (PAO) [52] and Telescop Array (TA) [53], we used statistics  $\chi_{red}^2$  defined as

$$\chi_{red}^2 = \sum_i \left( \frac{y_i^{data} - y_i^{model}}{\sigma_i^{data}} \right)^2 / \nu, \quad (3.7)$$

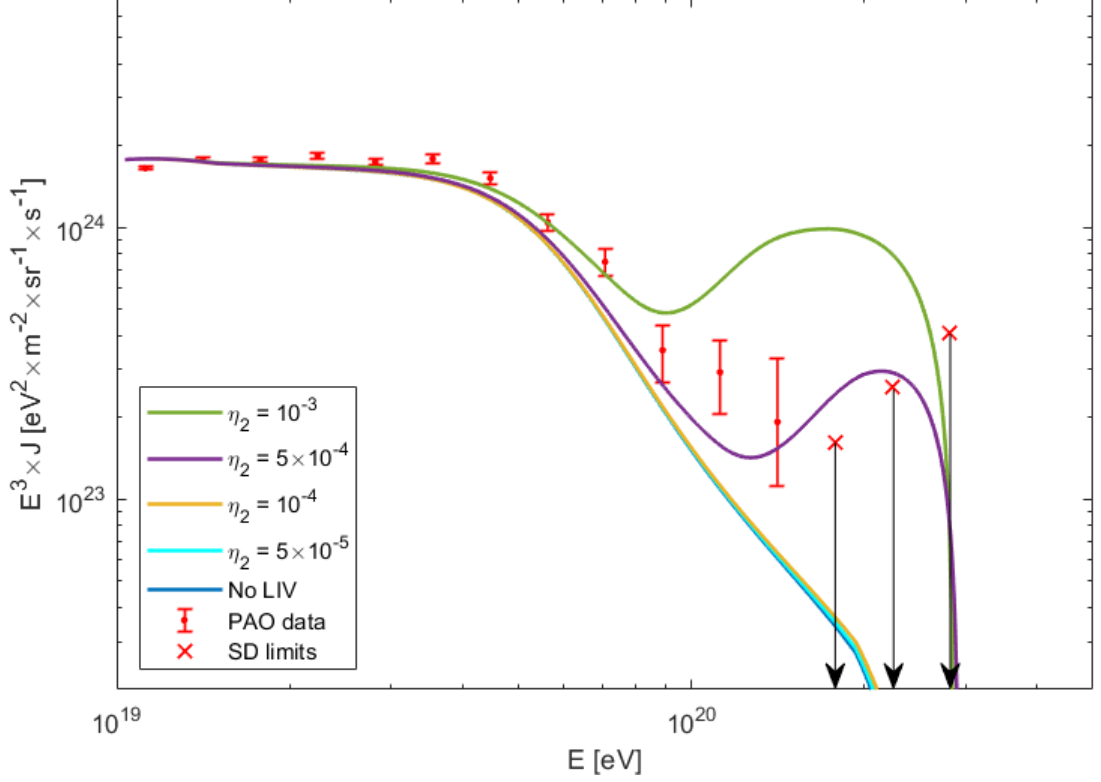


Figure 3.7: Models of CR spectra multiplied by  $E^3$  with spectral index  $\Gamma = 2.9$ , source evolution term  $\zeta = 6$  and proton maximal energy at source  $E_{max}^{source} = 10^{20.5}$  eV affected by LIV coefficients in legend. For more details see caption to Fig.3.3.

where  $\nu = N - n$  stands for the degrees of freedom, where  $N$  is the number of data points and  $n$  is number of fitted parameters.

The analytical models of the CR spectrum were calculated for combination of the following free parameters:  $0 \leq \zeta \leq 6$  with step of 0.5 (its effect is not strong),  $2.2 \leq \Gamma \leq 3$  with step of 0.1 and  $10^{20.5}$  eV  $\leq E_{max}^{source} \leq 10^{23}$  eV with step of  $10^{0.5}$  eV for the following values of  $\eta_2 = 0, 10^{-3}, 5 \times 10^{-4}, 10^{-4}$  and  $5 \times 10^{-5}$ .<sup>1</sup>

The resulting  $\chi_{red}^2$  values for the data measured by PAO and TA, for all the combinations of the chosen free parameters and LIV coefficients are given in Appendix C in form of three-dimensional surface plots (Figs.C.1, C.2, C.3, C.4, C.5 for data measured by PAO [52] and Figs.C.6, C.7, C.8, C.9, C.10 for data measured by TA [53]). Square root of the  $\chi_{red}^2$  was used in these figures to highlight the characteristics. Models that yields the best  $\chi_{red}^2$  for each of the LIV coefficients are depicted in Fig.3.8 for data measured by PAO [52] and in Fig.3.9 for data measured by TA [53]. The values of their respective free parameters are summarized in Tab.3.1.

<sup>1</sup> Case  $\eta_2 = 0$  correspond to No-LIV scenario.

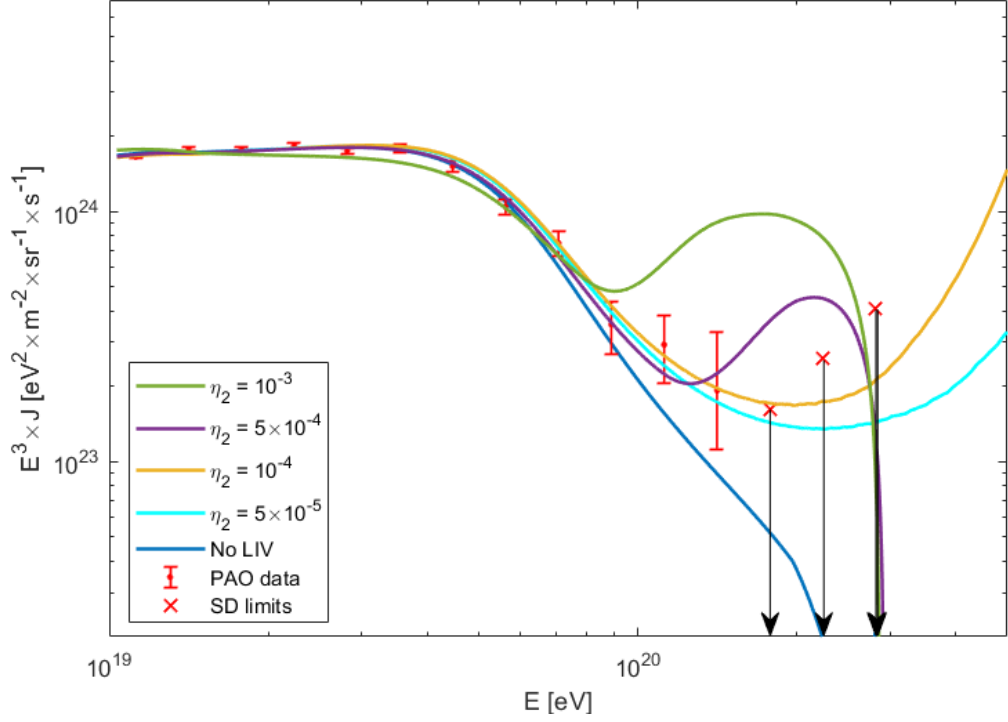


Figure 3.8: Models of CR spectra multiplied by  $E^3$  that had best values of  $\chi_{red}^2$  using data measured by PAO [52] for no-LIV and LIV scenarios. For more details see caption to Fig.3.3.

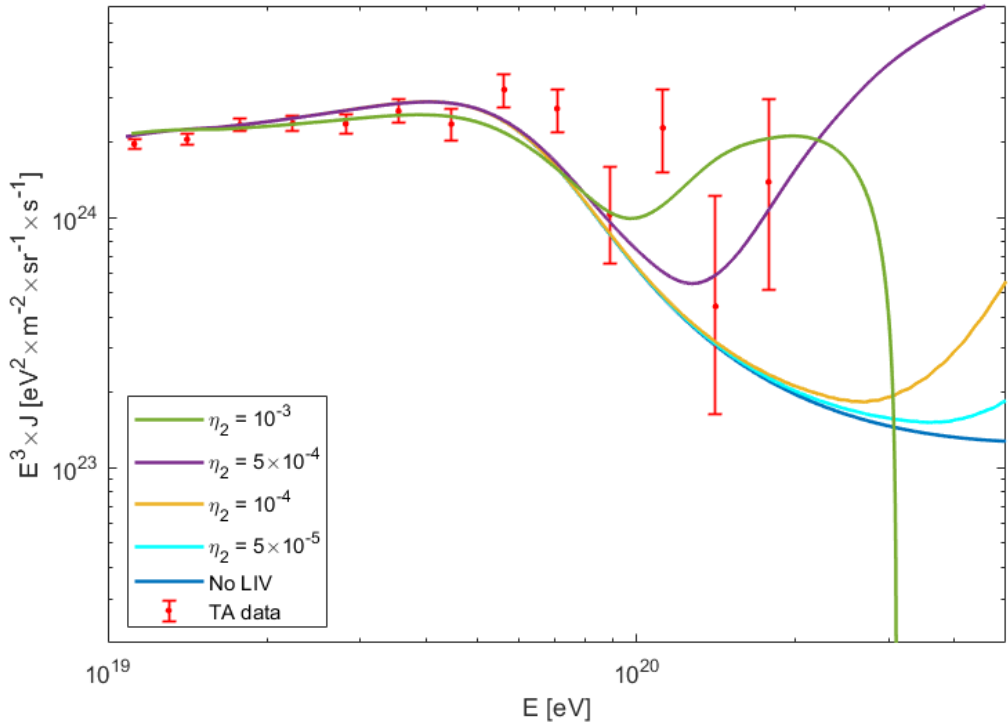


Figure 3.9: Models of CR spectra multiplied by  $E^3$  that had best values of  $\chi_{red}^2$  using data measured by TA [53] for no-LIV and LIV scenarios. The values of the respective free parameters  $\Gamma$ ,  $\zeta$  and  $E_{max}^{source}$  are given in Tab.3.1. The data with error bars represent the combined spectrum measured by TA [53].

Table 3.1: Values of the free parameters of the models of CR spectrum that yielded best compatibilities with measured data for no-LIV and LIV scenarios. The respective spectra are given in Fig.3.8 and Fig.3.9.

	PAO				TA			
	$\chi_{red}^2$	$\Gamma$	$\zeta$	$E_{max}^{source}$	$\chi_{red}^2$	$\Gamma$	$\zeta$	$E_{max}^{source}$
no LIV	3.2	2.7	6	20.5	1.78	2.7	0	23.0
$\eta_2 = 5 \times 10^{-5}$	3.15	2.7	6	23.0	1.68	2.7	0	23.0
$\eta_2 = 10^{-4}$	3.10	2.7	6	23.0	1.68	2.7	0	23.0
$\eta_2 = 5 \times 10^{-4}$	2.89	2.7	6	20.5	1.61	2.7	0	23.0
$\eta_2 = 10^{-3}$	16.95	2.9	6	20.5	2.83	2.8	0	20.5

To see how the best value of  $\chi_{red}^2$  changes with the increasing values of LIV coefficients, we plotted the best values of  $\sqrt{\chi_{red}^2}$  as a function of the LIV coefficients, separately for data measured by PAO [52] and TA [53] Fig.3.10. The root square of the best values of  $\chi_{red}^2$  was used to highlight the trends.

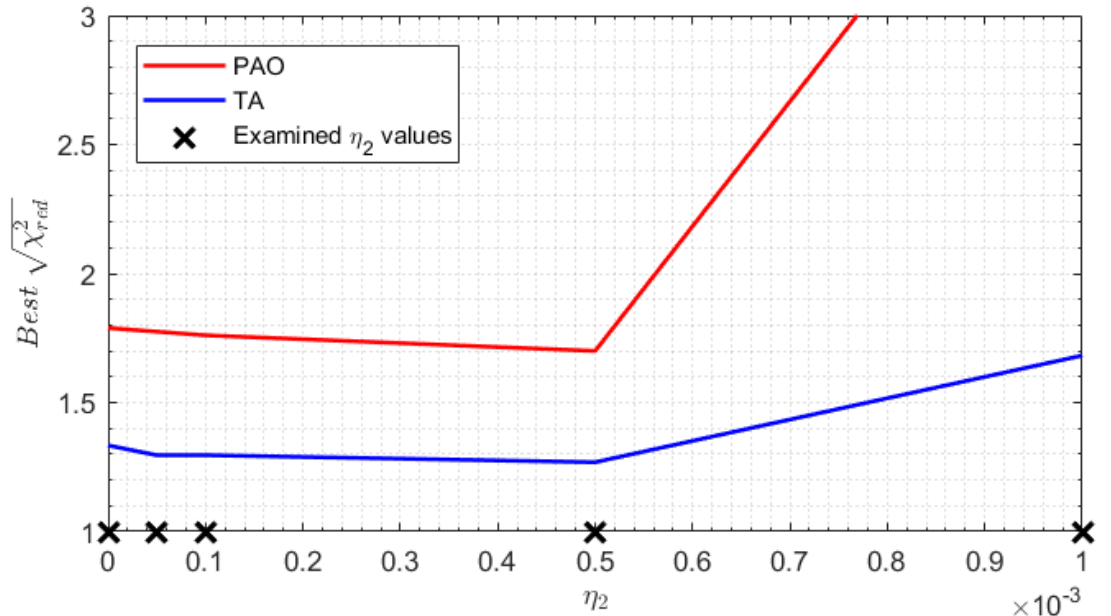


Figure 3.10: The best values of  $\sqrt{\chi_{red}^2}$  as a function of  $\eta_2$  coefficients. Red line represents the best values of  $\eta_2$  when using PAO data [52]. Blue line is for data of TA [53]. The black cross marks on x-axis are the examined values of  $\eta_2$ .

The behavior of the best  $\sqrt{\chi_{red}^2}$  was similar in both examined data sets (PAO and TA). The increase of the  $\eta_2$  slightly improve the best values of  $\chi_{red}^2$ . The trend goes up to  $\eta_2 = 5 \times 10^{-4}$  where the best value of  $\chi_{red}^2$  reaches its minimum. However, for  $\eta_2 = 10^{-3}$  the best value of  $\chi_{red}^2$  yields very high values, especially in the PAO case. Since the models of spectra are still compatible with  $\eta_2 = 5 \times 10^{-4}$  and incompatible with  $\eta_2 = 10^{-3}$  we estimate that the upper bound on the pion LIV coefficient is not less than  $5 \times 10^{-4}$  but not exceed  $10^{-3}$ , i.e.  $\eta_2^{up} \in (5 \times 10^{-4}, 10^{-3})$ .

Finally, we investigated the relation between the LIV coefficients and the free parameters  $\Gamma$ ,  $\zeta$ ,  $E_{max}^{source}$  of the model of CR spectrum. Number of occurrences

of models that yielded values of  $\chi_{red}^2 \leq 4.64$  for data measured by PAO [52] and  $\chi_{red}^2 \leq 4.27$  for TA [53] is given as a function of  $\Gamma$ ,  $\zeta$  in Fig.3.11 and Fig.3.12.<sup>2</sup> Plot for  $\eta_2 = 10^{-3}$  is not shown since the value of  $\chi_{red}^2$  in all the models was larger than the accepted value.

The Fig.3.11 for PAO case and Fig.3.12 for TA case show similar behavior. In each panel in Figs.3.11 and 3.12 the accepted solutions have the same values of spectral index  $\Gamma$  and source evolution term  $\zeta$ . Only the number of these solutions varies with  $\eta_2$ . For the coefficient  $\eta_2 = 5 \times 10^{-4}$  where the minimum of the best value of  $\chi_{red}^2$  is reached, they decrease remarkably. This indicates that parameter  $E_{max}^{source}$  is restricted. Thus, the LIV coefficients and  $E_{max}^{source}$  parameters are sensitive to each other.

The most accepted solutions in Figs.3.11 and 3.12 for spectral index  $\Gamma$  are found in the range 2.7 – 2.8 for data measured by PAO [52] and in the range 2.5 – 2.8 for TA [53] respectively. However, the best values of  $\chi_{red}^2$  is at  $\Gamma = 2.7$  for both cases. Regarding the source evolution term  $\zeta$ , the data from PAO [52] are more compatible with stronger evolution of the sources, and the best  $\chi_{red}^2$  is obtained for the highest allowed value  $\zeta = 6$ . On the other hand, data from TA [53] yields the best values for scenario without evolution ( $\zeta = 0$ ) although Fig.3.12 indicates acceptance of the higher values of  $\zeta$ .

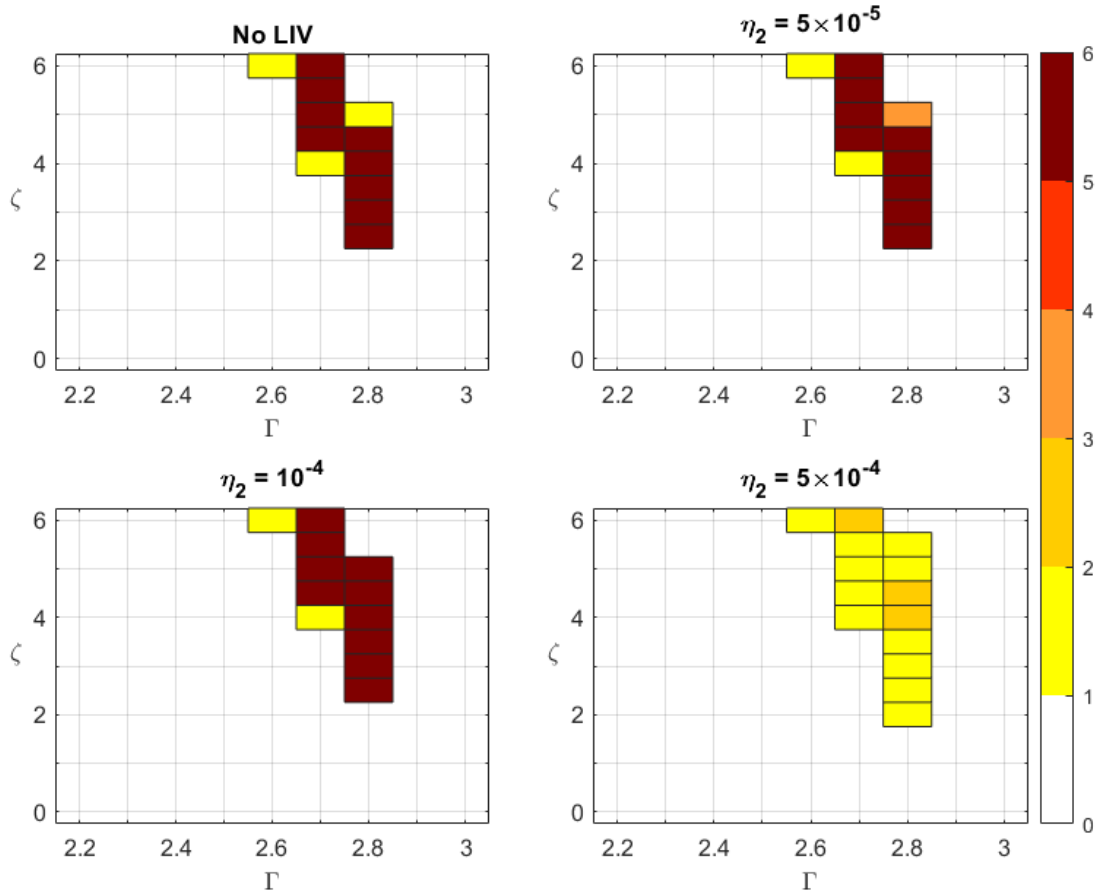


Figure 3.11: Number of solution with  $\chi_{red}^2 \leq 4.64$ , obtained using data from PAO [52] (color scale) as a function of spectral index  $\Gamma$  (x-axis) and source evolution term  $\zeta$  (y-axis).

<sup>2</sup> The chosen values of  $\chi_{red}^2$  correspond to p-value = 0.0001.

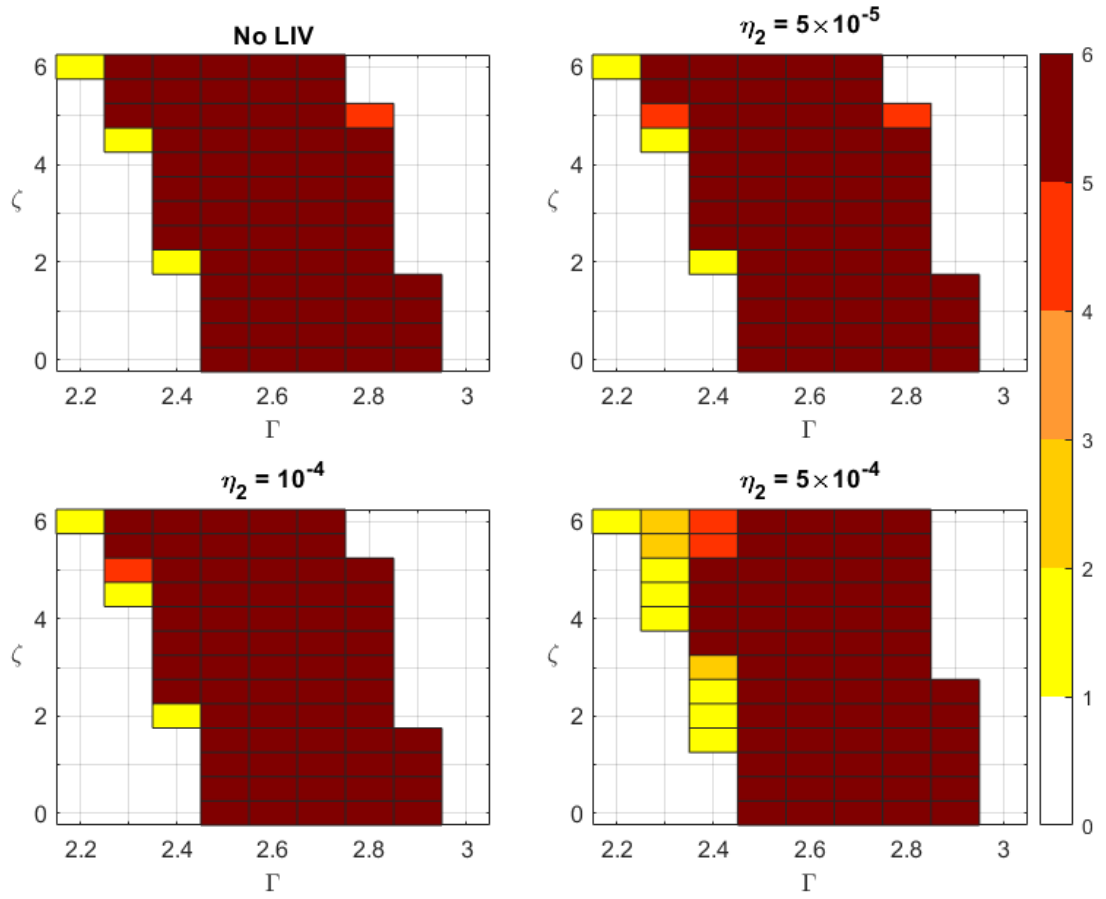


Figure 3.12: Number of solution with  $\chi_{red}^2 \leq 4.27$ , using data from TA [53] (color scale) as a function of spectral index  $\Gamma$  (x-axis) and source evolution term  $\zeta$  (y-axis).

# Conclusion

In this thesis, we dealt with the violation of Lorentz invariance and its effects on proton cosmic ray propagation. The effects of the violation of Lorentz invariance in  $2^{nd}$  on inelasticity and proton attenuation lengths were investigated some time ago in Ref.[21]. We calculated total energy losses for protons propagating through space and interacting with the cosmic microwave background. We intentionally affect their propagation by violating Lorentz invariance in the  $2^{nd}$ ,  $3^{rd}$  and  $4^{th}$  order. It was found that there is a slight difference in total energy losses when assuming different orders of the violation. However, this difference was not significant enough to affect the proton propagation. Based on this we concluded that violation of Lorentz invariance in  $3^{rd}$  and  $4^{th}$  order affect the shape of the Cosmic ray spectrum in the same manner as coefficients of  $2^{nd}$  order.

The effects of Lorentz invariance violation on Cosmic ray spectrum have been studied in Refs.[17, 21]. We took also into account a possible mutual influence between the free parameters of the spectrum model and coefficients describing Lorentz invariance violation. We learned that cosmic ray spectra are suitable to constraint the violation of Lorentz invariance. In the  $2^{nd}$  order of Lorentz invariance we estimated that the upper bound on pion Lorentz violating coefficient lies in the interval  $5 \times 10^{-4} - 10^{-3}$ . Moreover, we found that there is a considerable correlation between the parameters for maximal proton energy at source and coefficients that describe the violation of Lorentz invariance. Using different conditions, we also estimated effective horizons for cosmic protons affected by Lorentz invariance violation. Technically, as a side outcome, we worked out a different way of the analytical calculations of the proton spectra by using a derivation of spline functions.

Our future research will aim to examine the effects of Lorentz invariance violation on the Cosmic ray spectrum composed from nuclei.

# Bibliography

- [1] V.S. Berezhinskii and S.I. Grigor'eva. A bump in the ultra-high energy cosmic ray spectrum. *Astron. Astrophys.*, 199:1–12, 1988.
- [2] R.A. Mewaldt. Galactic cosmic ray composition and energy spectra. *Advances in Space Research*, 14(10):737–747, 1994.
- [3] J. R. Hörandel. Cosmic-ray composition and its relation to shock acceleration by supernova remnants. *Advances in Space Research*, 41:442–463, 2008.
- [4] A. R. Bell. Cosmic ray acceleration. *Astroparticle Physics*, 43:56–70, 2013.
- [5] M. Tanabashi et al. Review of particle physics. *Phys. Rev. D*, 98:030001, 2018. DOI:10.1103/PhysRevD.98.030001.
- [6] T. Abu-Zayyad et al. The knee and the second knee of the cosmic-ray energy spectrum. arXiv:1803.07052 [astro-ph.HE], 2018.
- [7] G. Cocconi. Intergalactic space and cosmic rays. *Nuovo Cimento*, 6(3):1433–1442, 1956.
- [8] A. M. Taylor. Cosmic rays beyond the knees. *Nature*, 531:43–44, 2016.
- [9] K. Kampert and M. Unger. Astroparticle Physics Measurements of the cosmic ray composition with air shower experiments. *Astroparticle Physics*, 35(10):660–678, 2012.
- [10] L. M. Widrow. Origin of galactic and extragalactic magnetic fields. *Rev. Mod. Phys.*, 74:775–823, 2002. DOI: 10.1103/RevModPhys.74.775.
- [11] H.P. Bretz et al. PARSEC: A parametrized simulation engine for ultra-high energy cosmic ray protons. *Astroparticle Physics*, 54:110 – 117, 2014.
- [12] V. Berezhinsky, A. Z. Gazizov, and S. I. Grigorieva. Ultrahigh-energy cosmic rays from extragalactic astrophysical sources: Energy losses and spectra. In *27th International Cosmic Ray Conference (ICRC 2001) Hamburg, Germany*, 2001. arXiv:hep-ph/0107306.
- [13] A. De Angelis and M.J.M. Pimenta. *Introduction to Particle and Astroparticle Physics*. First Edition. Springer, Milano, 2006.
- [14] J. P. Rachen and P. L. Biermann. Extragalactic ultrahigh-energy cosmic rays. 1. Contribution from hot spots in FR-II radio galaxies. *Astron. Astrophys.*, 272:161–175, 1993. arXiv:astro-ph/9301010v2.
- [15] G. R. Blumenthal. Energy Loss of High-Energy Cosmic Rays in Pair-Producing Collisions with Ambient Photons. *Phys. Rev. D*, 1:1596–1602, 1970. DOI:10.1103/PhysRevD.1.1596.
- [16] M. J. Chodorowski, A. A. Zdziarski, and M. Sikora. Reaction rate and energy-loss rate for photopair production by relativistic nuclei. *Astrophysical Journal*, 400:181–185, 1992. DOI:10.1086/171984.

- [17] J. Alfaro and G. Palma. Loop quantum gravity and ultrahigh energy cosmic rays. *Phys. Rev. D*, 67:083003, 2003. DOI:10.1103/PhysRevD.67.083003.
- [18] F.W. Stecker. Effect of photomeson production by the universal radiation field on high-energy cosmic rays. *Physical Review Letters*, 21:1016–1018, 1968.
- [19] J.P. Rachen. *Interaction Processes and Statistical Properties of the Propagation of Cosmic Rays in Photon Backgrounds*. University of Bonn, 1996.
- [20] M. Tanabashi et al. Review of particle physics. *Phys. Rev. D*, 98:030001, 2018. DOI:10.1103/PhysRevD.98.030001.
- [21] S.T. Scully and F.W. Stecker. Lorentz invariance violation and the observed spectrum of ultrahigh energy cosmic rays. *Astroparticle Physics*, 31:220–225, 2009. DOI:10.1016/j.astropartphys.2009.01.002.
- [22] A.M. Hillas. The origin of ultra-high-energy cosmic rays. *Ann. Rev. Astron. Astrophys.*, 22:425–444, 1984.
- [23] K.P. Ptitsyna and S.V. Troitsky. Physical conditions in potential accelerators of ultra-high-energy cosmic rays: updated hillas plot and radiation-loss constraints. *Physics-Uspekhi*, 53(7):691, 2010.
- [24] F. Frascetti. On the acceleration of ultra-high-energy cosmic rays. *Philosophical Transactions of the Royal Society A: Mathematical, Physical and Engineering Sciences*, 366(1884):4417–4428, 2008.
- [25] V. A. Kostelecký and S. Samuel. Spontaneous breaking of Lorentz symmetry in string theory. *Physical Review D.*, 39:683–685, 1989. DOI:10.1103/physrevd.39.68.
- [26] C.P. Burgess et al. Loop-generated bounds on changes to the graviton dispersion relation. *J. High Energy Phys.*, 3:043, 2002. DOI:10.1088/1126-6708/2002/03/043.
- [27] R. Gambini and J. Pullin. Nonstandard optics from quantum space-time. *Phys. Rev. D*, 59:124021, 1999. DOI:10.1103/PhysRevD.59.124021.
- [28] J. Bjorken. Emergent gauge bosons. In *Proceedings to the workshops: What comes beyond the standard model*, 2001. arXiv:hep-th/0111196 [hep-th].
- [29] T. Damour and A.M. Polyakov. The string dilation and a least coupling principle. *Nuclear Physics B*, 423(2):532–558, 1994. DOI:10.1016/0550-3213(94)90143-0.
- [30] A. A. Andrianov, R. Soldati, and L. Sorbo. Dynamical Lorentz symmetry breaking from a  $(3 + 1)$ -dimensional axion-Wess-Zumino model. *Phys. Rev. D*, 59, 1998. DOI:10.1103/PhysRevD.59.025002.
- [31] C. Barceló, S. Liberati, and M. Visser. Analogue Gravity. *Living Reviews in Relativity*, 8(1):12, 2005. DOI:10.12942/lrr-2005-12.

- [32] N. Arkani-Hamed, H. Cheng, M.A. Luty, and S. Mukohyama. Ghost condensation and a consistent infrared modification of gravity. *Journal of High Energy Physics*, 2004(05):074, 2004.
- [33] V. A. Kostelecký, R. Lehnert, and M. J. Perry. Spacetime-varying couplings and Lorentz violation. *Phys. Rev. D*, 68:123511, 2003. DOI:10.1103/PhysRevD.68.123511.
- [34] J. Magueijo. New varying speed of light theories. *Reports on Progress in Physics*, 66(11):2025, 2003.
- [35] D. Mattingly. Modern Tests of Lorentz Invariance. *Living Reviews in Relativity*, 8:5, 2005. DOI:10.12942/lrr-2005-5.
- [36] T. Jacobson, S. Liberati, and D. Mattingly. Lorentz violation at high energy: Concepts, phenomena, and astrophysical constraints. *Annals of Physics*, 321(1):150–196, 2006. DOI:10.1016/j.aop.2005.06.004.
- [37] T. Jacobson, S. Liberati, and D. Mattingly. Threshold effects and Planck scale Lorentz violation: Combined constraints from high energy astrophysics. *Phys. Rev. D*, 67:124011, 2003. DOI:10.1103/PhysRevD.67.124011.
- [38] Sidney Coleman and Sheldon L. Glashow. High-energy tests of Lorentz invariance. *Phys. Rev. D*, 59:116008, 1999.
- [39] J. Wei et al. Constraining Anisotropic Lorentz Violation via the Spectral-lag Transition of GRB 160625B. *The Astrophysical Journal*, 842(2):115, 2017. DOI:10.3847/1538-4357/aa7630.
- [40] S. Lijing and M. Bo-Qiang. Lorentz-violation-induced vacuum birefringence and its astrophysical consequences. *Phys. Rev. D*, 83:127702, 2011.
- [41] B. Altschul. Lorentz violation and synchrotron radiation. *Phys. Rev. D*, 72:085003, 2005.
- [42] Robert Bluhm, V. Alan Kostelecký, and Neil Russell. CPT and lorentz tests in penning traps. *Phys. Rev. D*, 57:3932–3943, 1998.
- [43] V. Alan Kostelecký and Arnaldo J. Vargas. Lorentz and *cpt* tests with clock-comparison experiments. *Phys. Rev. D*, 98:036003, 2018.
- [44] B.R. Heckel et al. Torsion Balance Test of Spin Coupled Forces. In *Quantum Gravity, Generalized Theory of Gravitation, and Superstring Theory-Based Unification*, pages 153–160, 2002. DOI:10.1007/0-306-47104-3-14.
- [45] V. Alan Kostelecký. CPT, T, and Lorentz violation in neutral-meson oscillations. *Phys. Rev. D*, 64:076001, 2001.
- [46] B. Botermann et al. Test of Time Dilation Using Stored  $\text{Li}^+$  Ions as Clocks at Relativistic Speed. *Phys. Rev. Lett.*, 113:120405, 2014.
- [47] André H. Gomes, V. Alan Kostelecký, and Arnaldo J. Vargas. Laboratory tests of Lorentz and *CPT* symmetry with muons. *Phys. Rev. D*, 90:076009, 2014.

- [48] K. K. Vos, H. W. Wilschut, and R. G. E. Timmermans. Concurrent tests of lorentz invariance in  $\beta$ -decay experiments. *Phys. Rev. C*, 92:052501, 2015.
- [49] Torri, M.D.C. and Bertini, S. and Giammarchi, M. and Miramont, L. . Lorentz invariance violation and the observed spectrum of ultrahigh energy cosmic rays. *Journal of High Energy Astrophysics*, 18:5–14, 2018. DOI:10.1016/j.jheap.2018.01.001.
- [50] T. H. Bertschinger, N.A. Flowers, and J. D. Tasson. Observer and Particle Transformations and Newton’s Laws. In *Proceedings, 6th Meeting on CPT and Lorentz Symmetry (CPT 13): Bloomington, Indiana, USA*, 2014. DOI:10.1142/9789814566438-0072.
- [51] V. Berezhinsky, A. Gazizov, and S. Grigorieva. On astrophysical solution to ultrahigh energy cosmic rays. *Phys. Rev. D*, 74:043005, 2006. DOI:10.1103/PhysRevD.74.043005.
- [52] Pierre Auger Collaboration. The Pierre Auger Observatory: Contributions to the 35th International Cosmic Ray Conference (ICRC 2017). In *35th International Cosmic Ray Conference, Bexco, Busan, Korea.*, volume ICRC 2017, 2017. arXiv:1708.06592[astro-ph.HE].
- [53] I. Dmitri. TA Spectrum Summary. In *Proceedings, 34th International Cosmic Ray Conference (ICRC 2015): The Hague, The Netherlands*, volume ICRC 2015, page 349, 2016. DOI:10.22323/1.236.0349.

# List of Abbreviations

CMB	Cosmic microwave background
CR	Cosmic rays
GZK	Greizen-Zatsepin-Kuzmin
LI	Lorenz invariance
LIV	Lorenz invariance violation
PAO	Pierre Auger Observatory
TA	Telescop Array
UHECR	Ultra-high energy cosmic rays

# A. Appendix

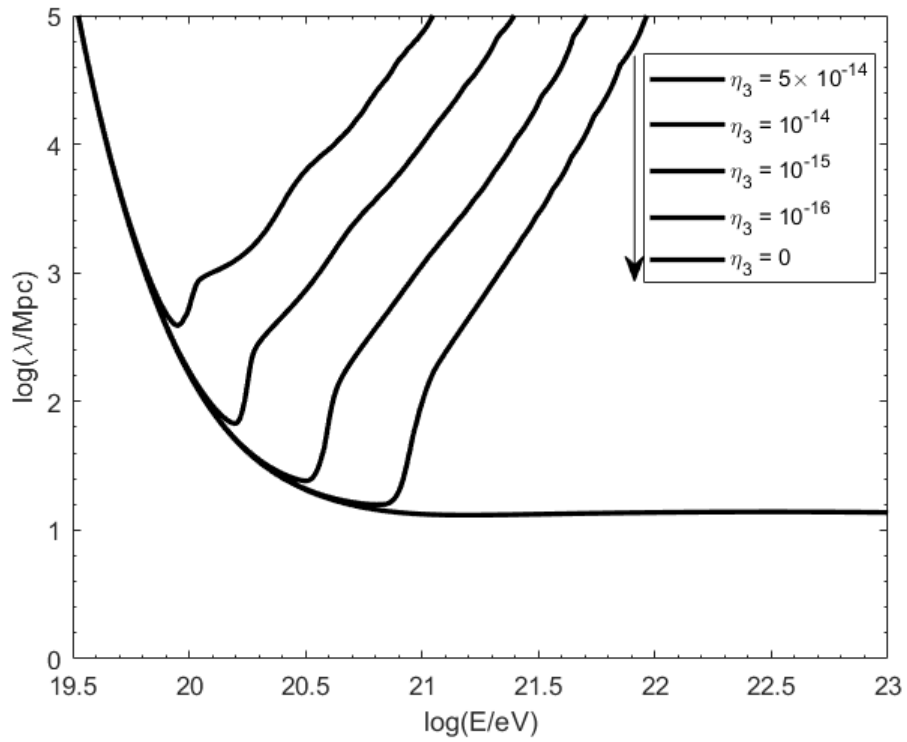


Figure A.1: Proton attenuation length as a function of proton energy affected by 3<sup>rd</sup> order LIV coefficients.

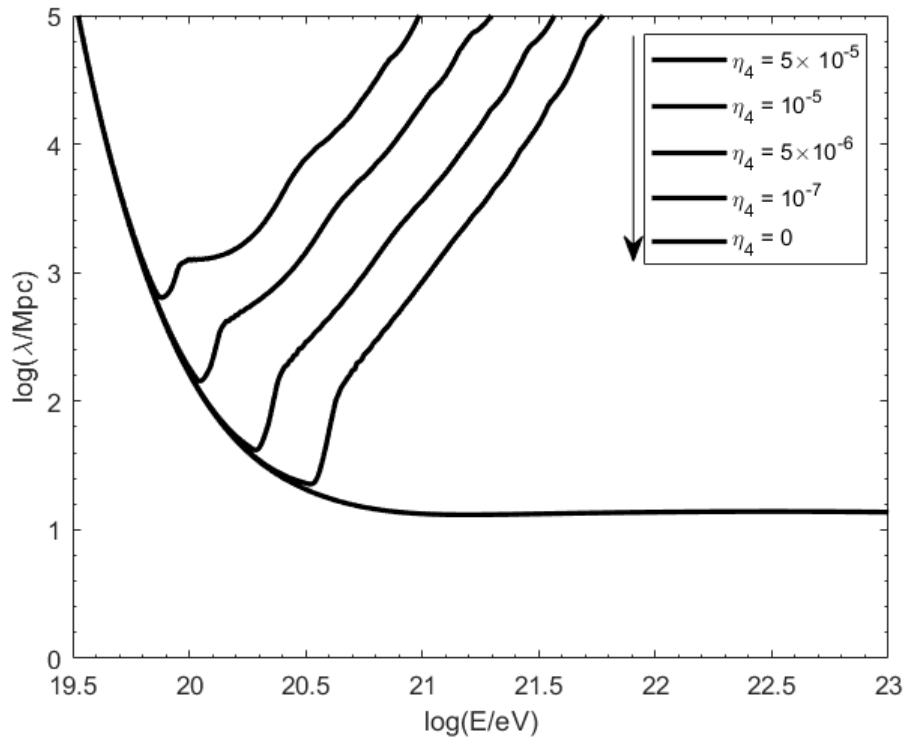


Figure A.2: Proton attenuation length as a function of proton energy affected by 4<sup>th</sup> order LIV coefficients.

## B. Appendix

Fully expanded form of the transcendental equation for inelasticity modified by LIV. The variables and constants are explained in Chapter 2.

$$\begin{aligned}
0 = & (1 - K_\theta) \sqrt{(2\sqrt{\Delta_p(E_p) + m_p^2} \epsilon + \Delta_p(E_p) + m_p^2)} \\
& - \left( \frac{1}{2\sqrt{(2\sqrt{\Delta_p(E_p) + m_p^2} \epsilon + \Delta_p(E_p) + m_p^2)}} \right. \\
& \times \left[ (2\sqrt{\Delta_p(E_p) + m_p^2} \epsilon + \Delta_p(E_p) + m_p^2) \right. \\
& \left. + (\Delta_N((1 - K_\theta)E_p) + m_N^2) - (\Delta_\pi(K_\theta E_p) + m_\pi^2) \right] \\
& + \left( \frac{1}{2\sqrt{(2\sqrt{\Delta_p(E_p) + m_p^2} \epsilon + \Delta_p(E_p) + m_p^2)}} \right. \\
& \times \left[ (2\sqrt{\Delta_p(E_p) + m_p^2} \epsilon + \Delta_p(E_p) + m_p^2) + (\Delta_N((1 - K_\theta)E_p) + m_N^2) \right. \\
& \left. \left. - (\Delta_\pi(K_\theta E_p) + m_\pi^2) \right] - (\Delta_N((1 - K_\theta)E_p) + m_N^2) \right)^{1/2} \cos(\theta)
\end{aligned} \tag{B.1}$$

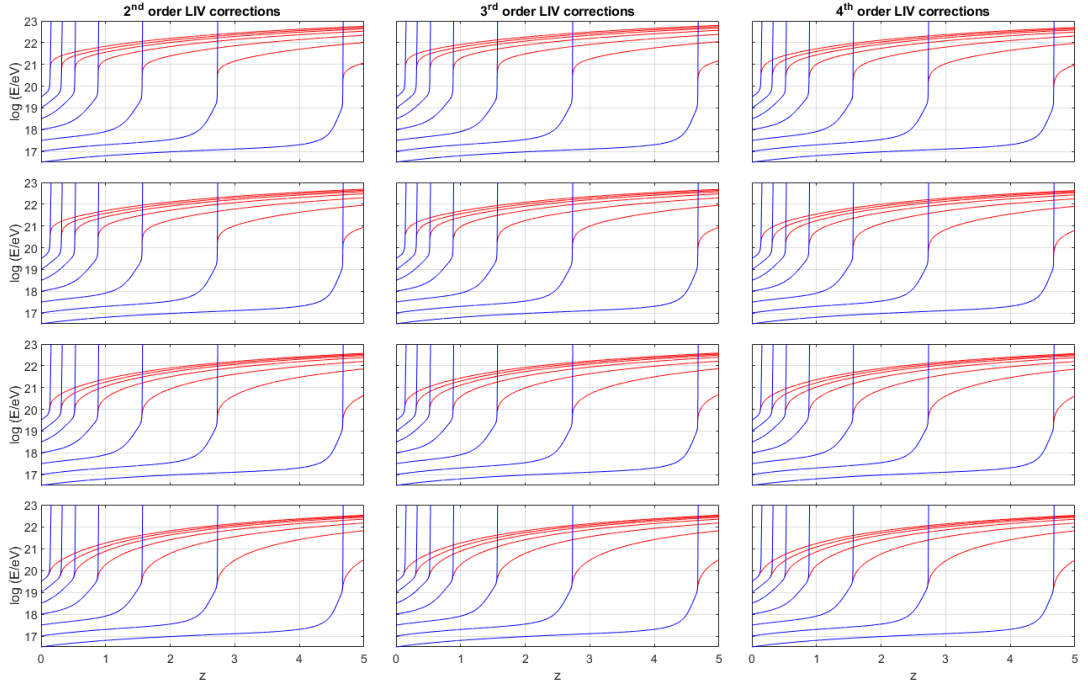


Figure B.1: Proton energy evolution as a function of redshift affected by different values of  $\eta_n$ . The values of  $\eta_2$ , starting from the top plot are:  $5 \times 10^{-5}$ ,  $\times 10^{-4}$ ,  $5 \times 10^{-4}$  and  $\times 10^{-3}$ . For the middle column, the values of  $\eta_3$  are  $5 \times 10^{-14}$ ,  $10^{-14}$ ,  $10^{-15}$ , and  $10^{-16}$ . For the last column, the values of  $\eta_4$  are  $5 \times 10^{-5}$ ,  $10^{-5}$ ,  $10^{-6}$  and  $10^{-7}$ .

## C. Appendix

Surface plots of  $\sqrt{\chi_{red}^2}$  as a function of  $\Gamma, \zeta$  and  $E_{max}$  for data measured by PAO

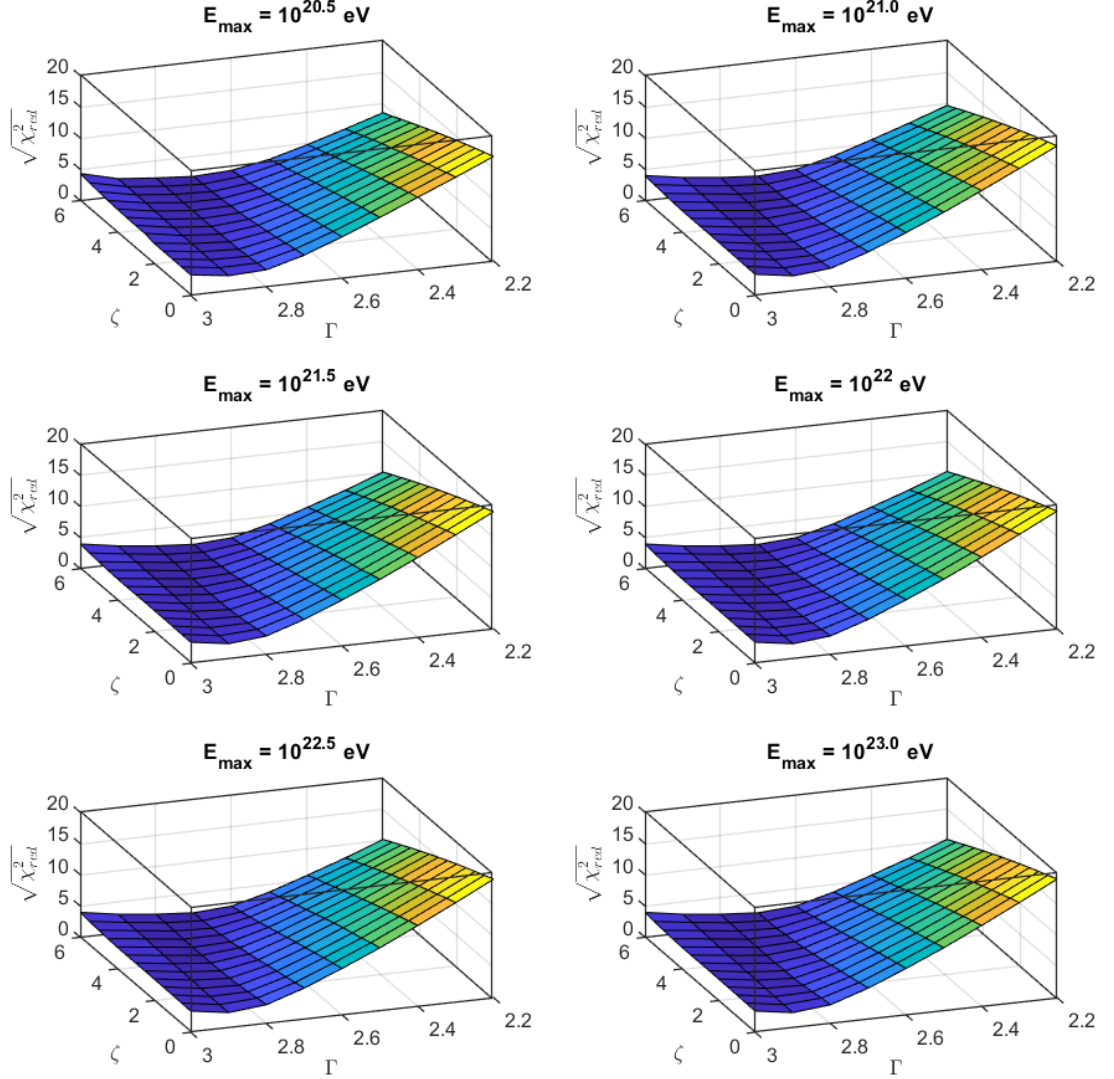


Figure C.1: Values of  $\sqrt{\chi_{red}^2}$  as a function of spectral index  $\Gamma$  and source evolution term  $\zeta$  for six different proton maximal energies at source  $E_{max}^{source}$ . Solutions without LIV for data measured by PAO [52].

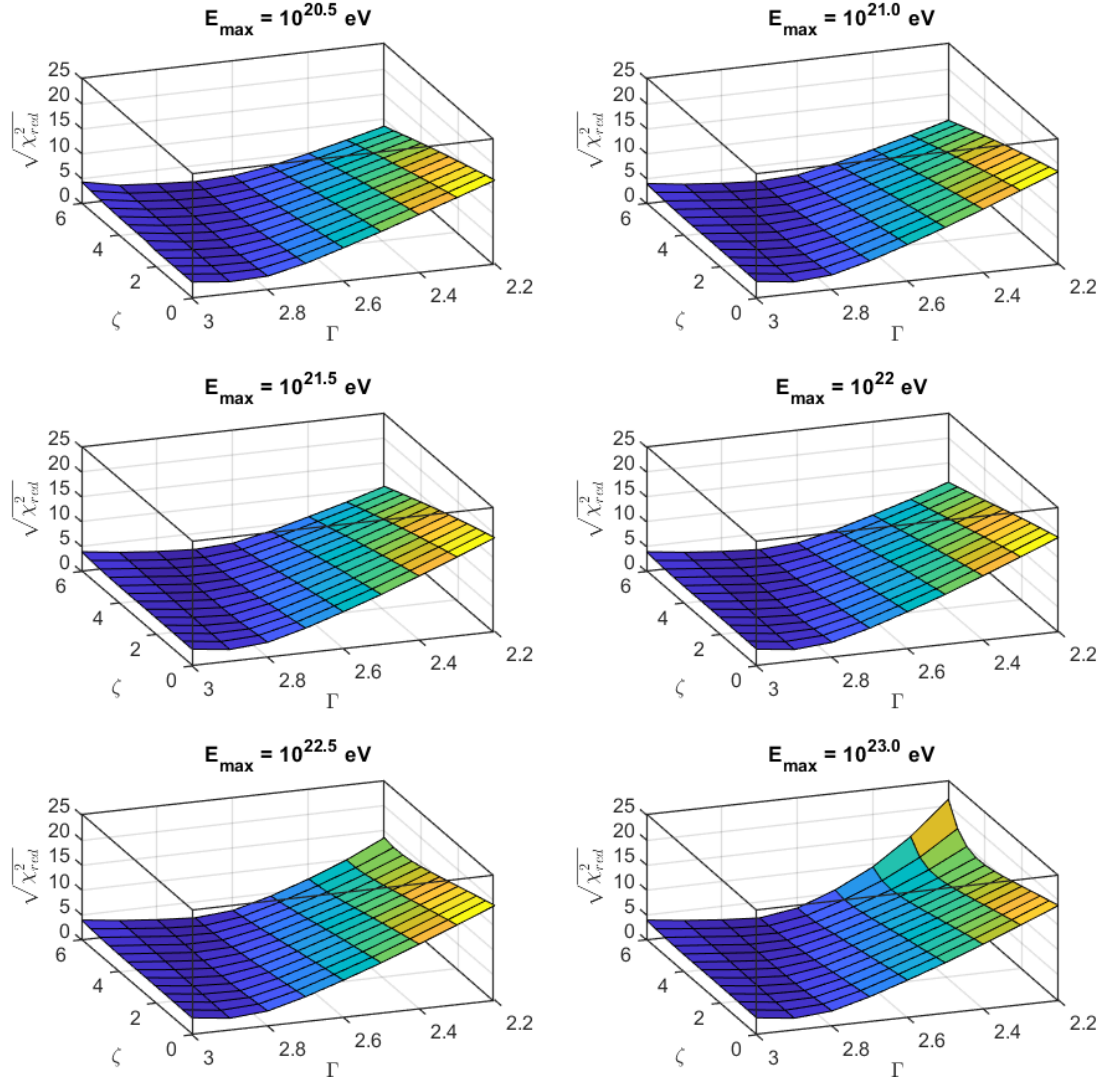


Figure C.2: Values of  $\sqrt{\chi_{red}^2}$  as a function of spectral index  $\Gamma$  and source evolution term  $\zeta$  for six different proton maximal energies at source  $E_{max}^{source}$ . Solutions with LIV correction  $\eta_2 = 5 \times 10^{-5}$  for data measured by PAO [52].

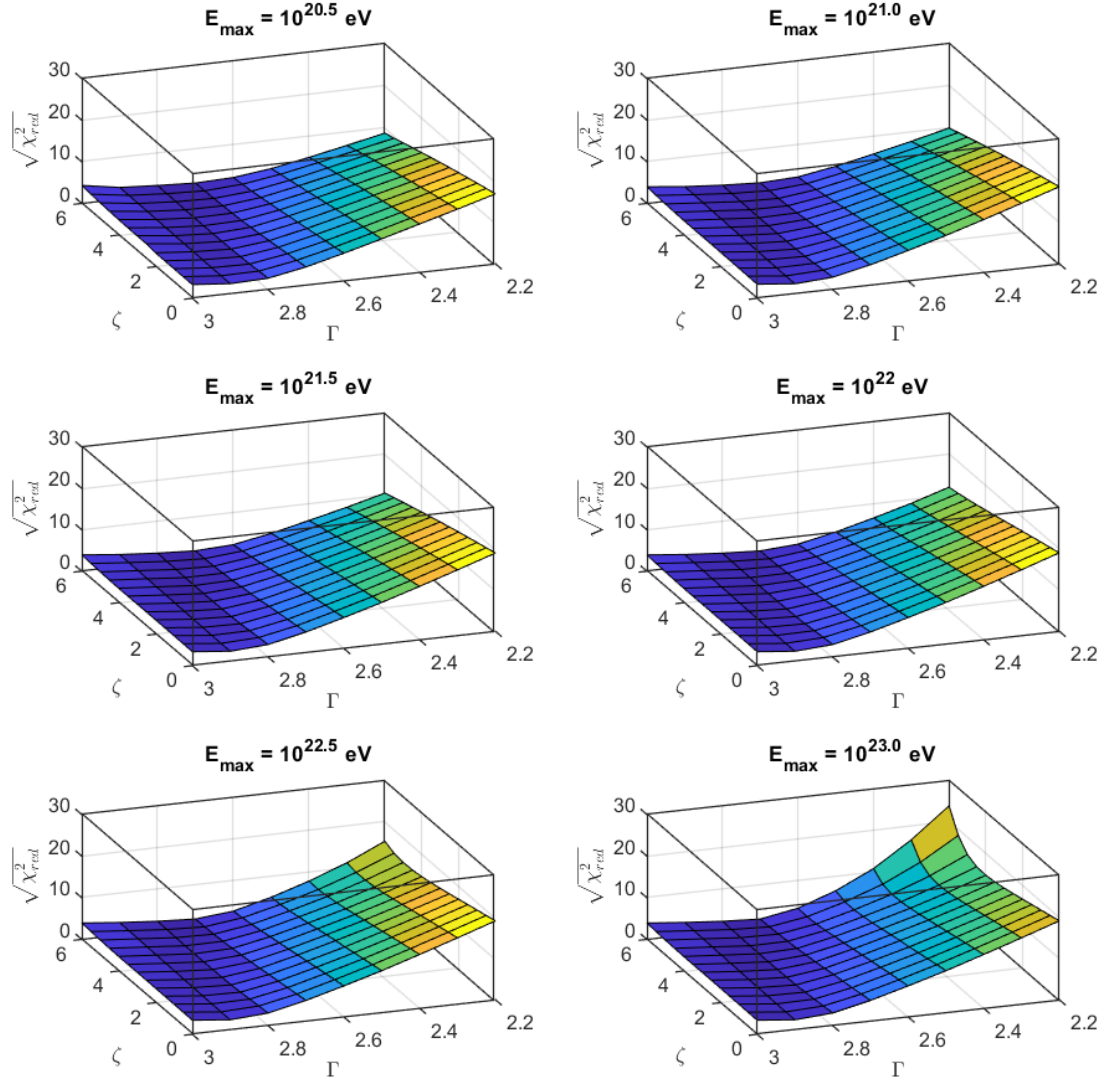


Figure C.3: Values of  $\sqrt{\chi_{red}^2}$  as a function of spectral index  $\Gamma$  and source evolution term  $\zeta$  for six different proton maximal energies at source  $E_{max}^{source}$ . Solutions with LIV correction  $\eta_2 = 10^{-4}$  for data measured by PAO [52].

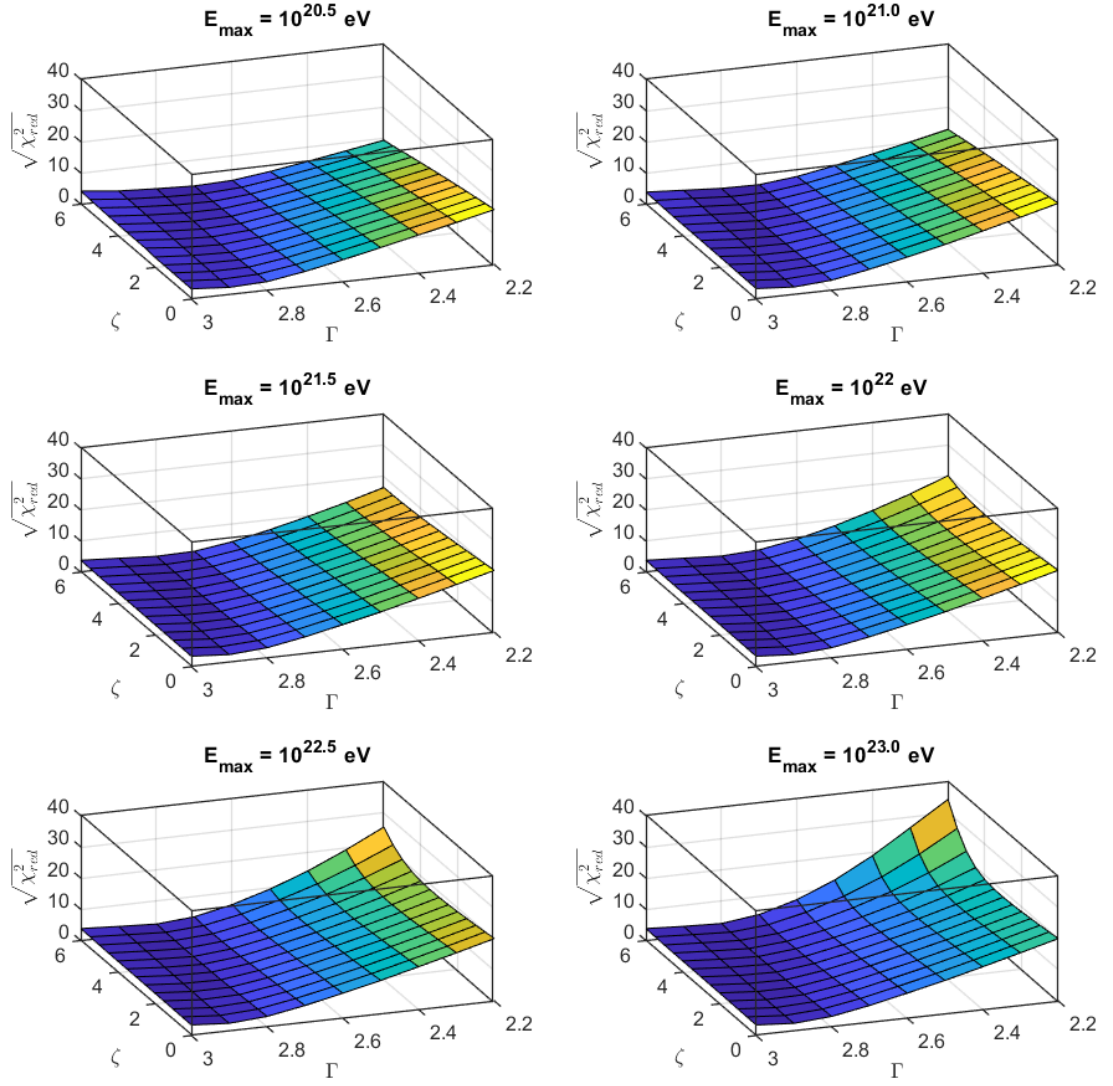


Figure C.4: Values of  $\sqrt{\chi_{red}^2}$  as a function of spectral index  $\Gamma$  and source evolution term  $\zeta$  for six different proton maximal energies at source  $E_{max}^{source}$ . Solutions with LIV correction  $\eta_2 = 5 \times 10^{-4}$  for data measured by PAO [52].

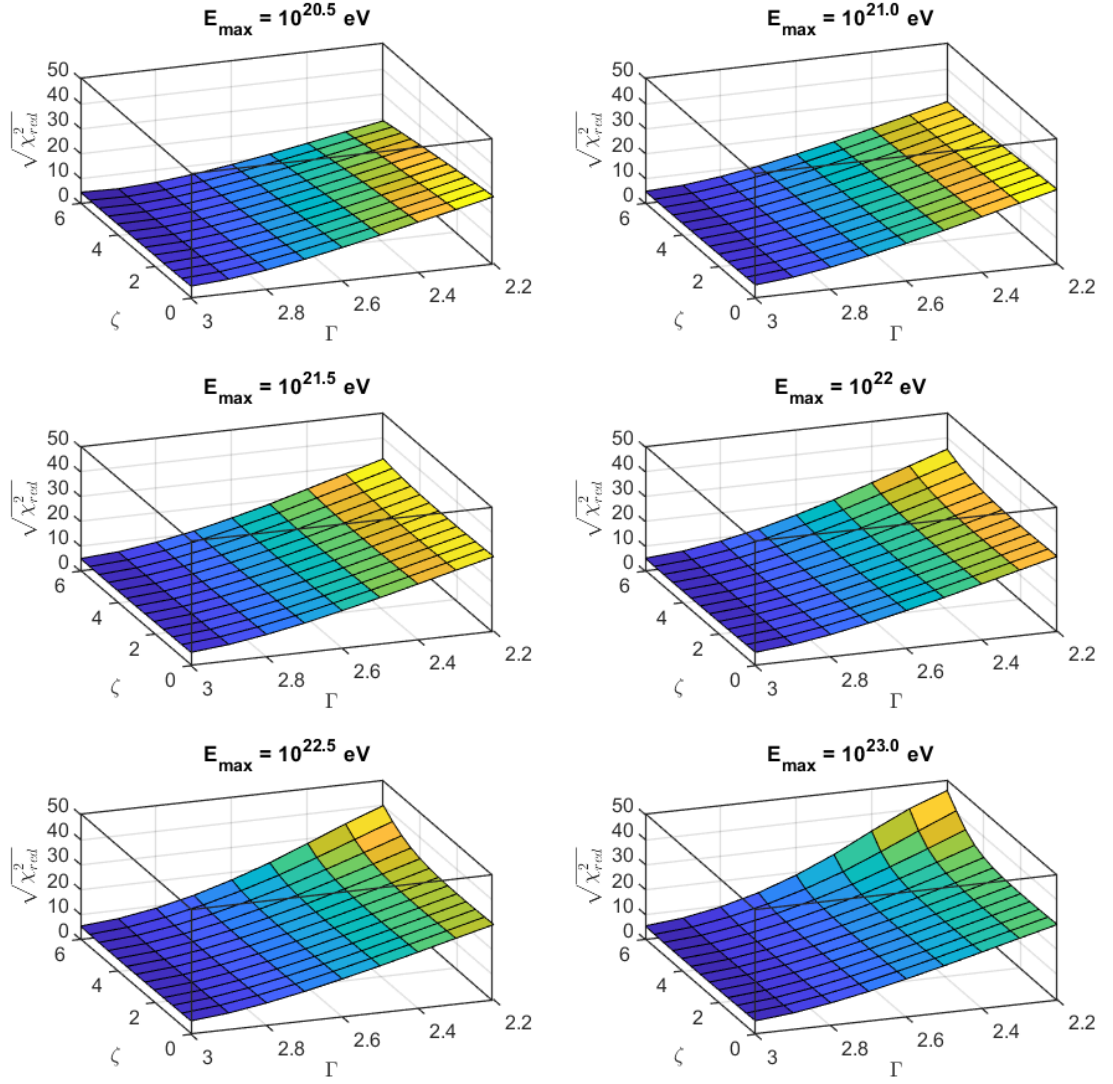


Figure C.5: Values of  $\sqrt{\chi_{red}^2}$  as a function of spectral index  $\Gamma$  and source evolution term  $\zeta$  for six different proton maximal energies at source  $E_{max}^{source}$ . Solutions with LIV correction  $\eta_2 = 10^{-3}$  for data measured by PAO [52].

## Surface plots of $\sqrt{\chi_{red}^2}$ as a function of $\Gamma, \zeta$ and $E_{max}$ for data measured by TA

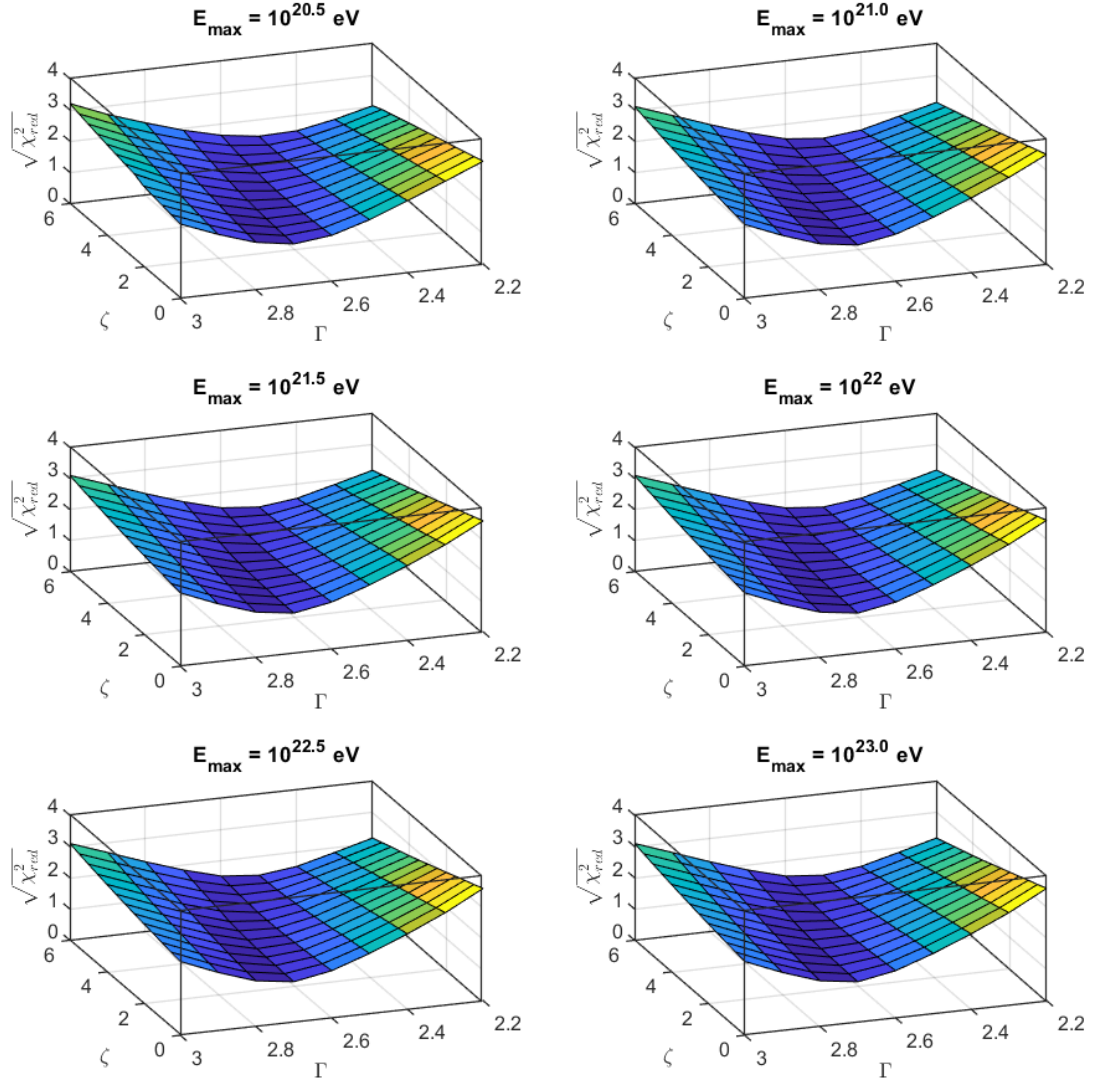


Figure C.6: Values of  $\sqrt{\chi_{red}^2}$  as a function of spectral index  $\Gamma$  and source evolution term  $\zeta$  for six different proton maximal energies at source  $E_{max}^{source}$ . Solutions without LIV for data measured by TA [53].

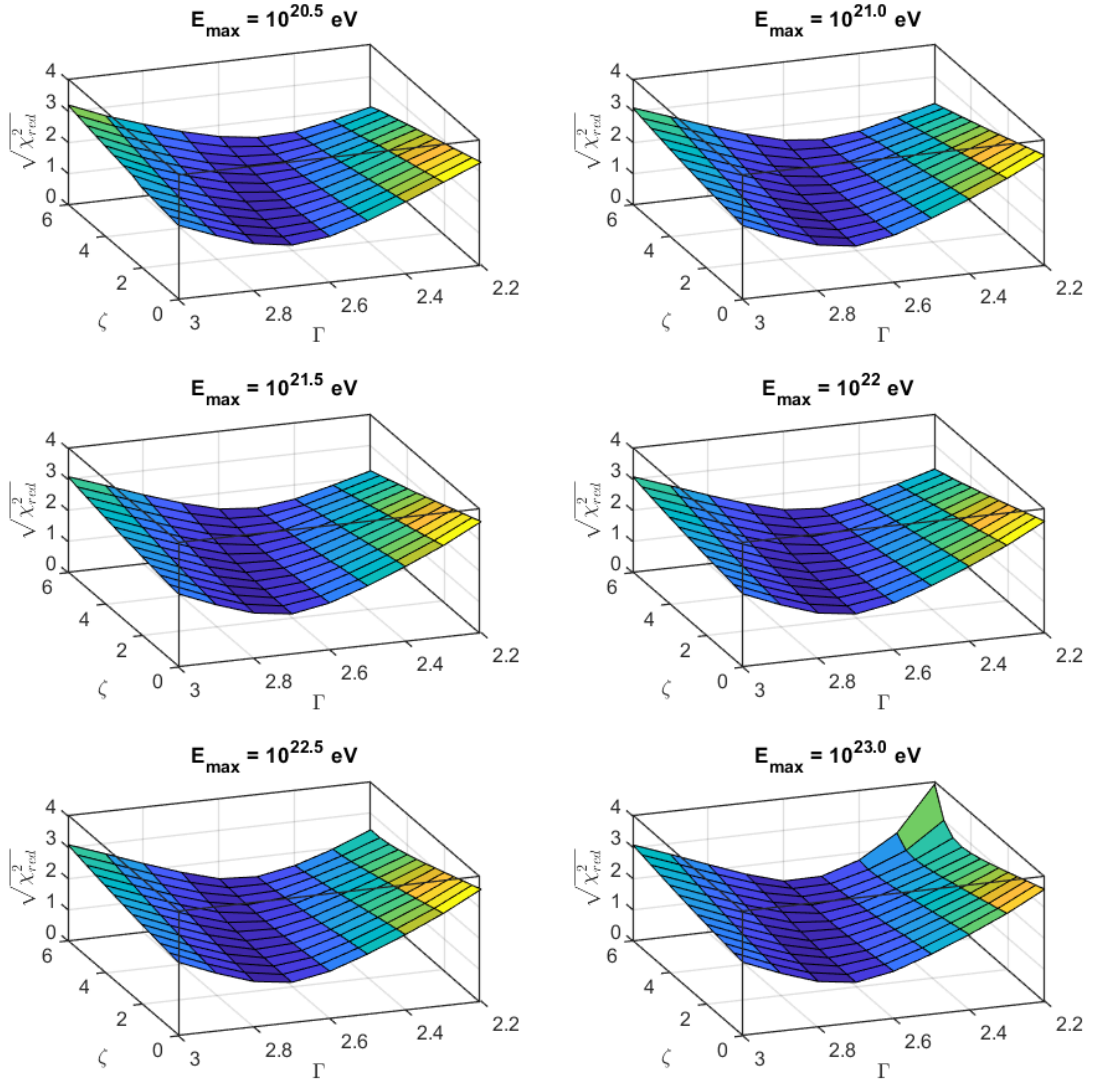


Figure C.7: Values of  $\sqrt{\chi_{red}^2}$  as a function of spectral index  $\Gamma$  and source evolution term  $\zeta$  for six different proton maximal energies at source  $E_{max}^{source}$ . Solutions with LIV correction  $\eta_2 = 5 \times 10^{-5}$  for data measured by TA [53].

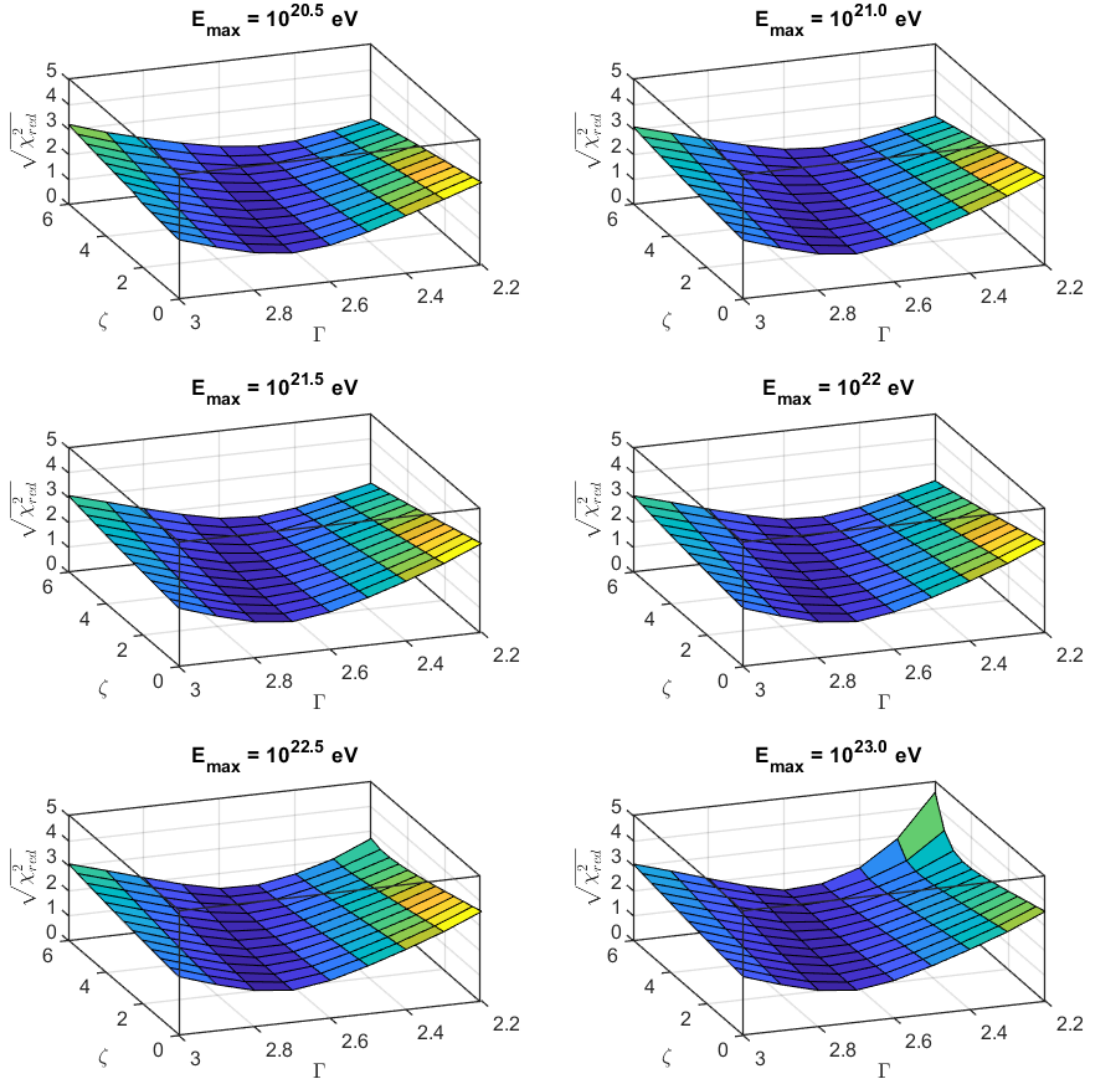


Figure C.8: Values of  $\sqrt{\chi_{red}^2}$  as a function of spectral index  $\Gamma$  and source evolution term  $\zeta$  for six different proton maximal energies at source  $E_{max}^{source}$ . Solutions with LIV correction  $\eta_2 = 10^{-4}$  for data measured by TA [53].

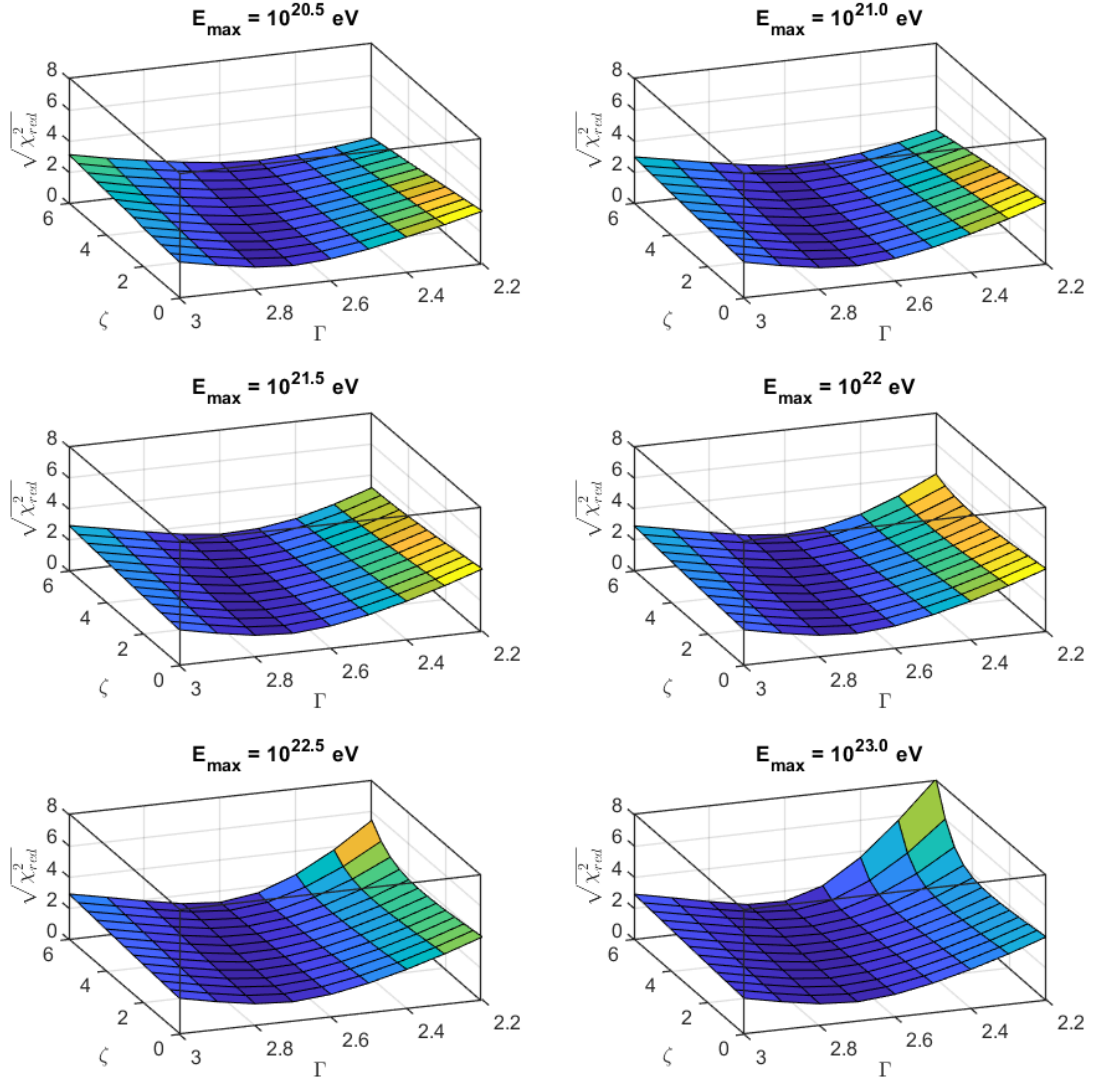


Figure C.9: Values of  $\sqrt{\chi_{red}^2}$  as a function of spectral index  $\Gamma$  and source evolution term  $\zeta$  for six different proton maximal energies at source  $E_{max}^{source}$ . Solutions with LIV correction  $\eta_2 = 5 \times 10^{-4}$  for data measured by TA [53].

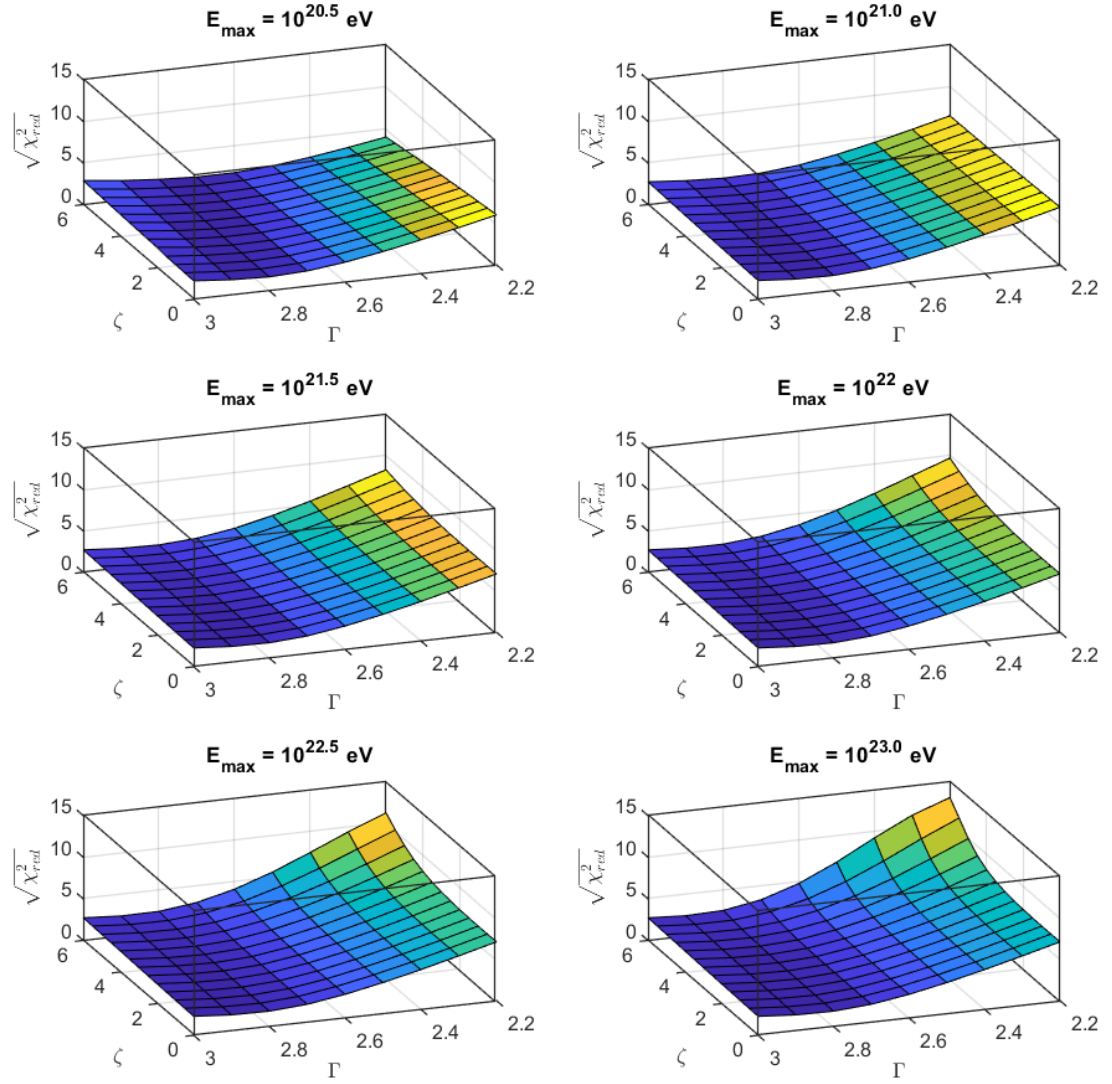


Figure C.10: Values of  $\sqrt{\chi_{red}^2}$  as a function of spectral index  $\Gamma$  and source evolution term  $\zeta$  for six different proton maximal energies at source  $E_{max}^{source}$ . Solutions with LIV correction  $\eta_2 = 10^{-3}$  for data measured by TA [53].